A Microfluidic Platform for the Efficient Determination of Liquid-Liquid Equilibria Using Raman Microspectroscopy

Eine mikrofluidische Plattform für die effiziente Bestimmung von Flüssig-flüssig-Gleichgewichten mittels Raman-Mikrospektroskopie

Von der Fakultät für Maschinenwesen der
Rheinisch-Westfälischen Technischen Hochschule Aachen
zur Erlangung des akademischen Grades einer Doktorin
der Ingenieurwissenschaften genehmigte Dissertation

vorgelegt von

Julia Jutta Thien

Berichter: Univ.-Prof. Dr.-Ing. André Bardow
apl. Prof. Dr.-Ing. Hans-Jürgen Koß
Univ.-Prof. Dr.-Ing. Andreas Jupke

Tag der mündlichen Prüfung: 18. April 2024

Aachener Beiträge zur Technischen Thermodynamik Band 54

Julia Jutta Thien
A Microfluidic Platform for the Efficient Determination of Liquid-Liquid Equilibria Using Raman Microspectroscopy

Eine mikrofluidische Plattform für die effiziente Bestimmung von Flüssig-flüssig-Gleichgewichten mittels Raman-Mikrospektroskopie

ISBN: 978-3-95886-542-6

Bibliografische Information der Deutschen Bibliothek
Die Deutsche Bibliothek verzeichnet diese Publikation in der Deutschen Nationalbibliografie; detaillierte bibliografische Daten sind im Internet über http://dnb.ddb.de abrufbar.

Herstellung & Vertrieb:

1. Auflage 2025
© Wissenschaftsverlag Mainz GmbH - Aachen
Süsterfeldstr. 83, 52072 Aachen
Tel. 0241 / 87 34 34 00
www.Verlag-Mainz.de

ISSN: 2198-4832

Satz: nach Druckvorlage des Autors
Umschlaggestaltung: Druckerei Mainz

printed in Germany
D82 (Diss. RWTH Aachen University, 2024)

Vorwort

Die vorliegende Arbeit entstand während meiner Zeit als wissenschaftliche Mitarbeiterin am Lehrstuhl für Technische Thermodynamik der RWTH Aachen.

Ein ganz besonderer Dank gilt meinem Doktorvater Prof. André Bardow, der mich schon als Patenprofessor im Studium begleitet und mir anschließend das Vertrauen entgegengebracht hat, an seinem Lehrstuhl zu promovieren. Ihm und meinem Gruppenleiter und zweiten Prüfer Prof. Hans-Jürgen Koß danke ich außerdem dafür, dass sie mir durch ihre Unterstützung sehr geholfen haben, mich fachlich und persönlich zu entwickeln. Mein herzlicher Dank gilt auch Prof. Andreas Jupke für die Übernahme des Korreferats und Prof. Dieter Moormann für die Übernahme des Prüfungsvorsitzes und die angenehme Art, die Prüfung zu leiten.

Auch bei allen Kollegen am LTT möchte ich mich für die tolle Zeit und die großartigen Erfahrungen bedanken. Ganz besonders möchte ich dabei Dominique danken, die mich fachlich sehr viel gelehrt hat und gleichzeitig eine gute Freundin wurde. Ebenso danke ich allen Mitgliedern der OMT für die tollen fachlichen und persönlichen Gespräche und Freizeitaktivitäten und möchte dabei ganz besonders Christine, Ludger, Carsten und Marvin, die das Büro mit mir geteilt und den Spirit des Mädchenzimmers aufrechterhalten haben, und Thorsten, der mir immer mit einem guten Rat zur Seite stand, hervorheben.

Ein großer Dank gilt auch allen TaMis für die tolle Unterstützung und die netten Gespräche und allen Studierenden, die mich begleitet und unterstützt haben. Ganz besonders möchte ich mich dabei bei Marvin bedanken, der mich viele Jahre als Student begleitet und insbesondere während meiner Elternzeit sehr unterstützt hat und anschließend ein super Kollege und Freund wurde.

Nicht zuletzt danke ich meiner Familie, insbesondere meinen Eltern, meiner Schwester Annika, Dominik und meinen Kindern, dafür, dass sie mich stets unterstützen, mein Leben bereichern und mich glücklich machen!

Julia

Contents

List of Figures

List of Tables

Notation

Abbreviations

C	Continuous
Ca	Capillary Number
CCD	Charge-Coupled Device
D	Dispersed
DDU	Droplet Detection Unit
GC	Gas Chromatography
H	Height
IHM	Indirect Hard Modeling
KH	Kelvin-Helmholtz
L	Length
LLE	Liquid-Liquid Equilibrium
LPME	Liquid Phase Microextraction
M	Mixture
Nd:YAG	Neodymium-Doped Yttrium Aluminum Garnet
o	observation point
PEEK	Polyether Ether Ketone
PTFE	Polytetrafluoroethylene
Re	Reynolds Number
ROI	Region of Interest
tot	total
W	Width

Symbols

A_i	Area of component i	
d	characteristic length scale	m
G	Gibbs free energy	J
K_i	distribution coefficient of component i	
n_i	amount of substance of component i	mole
p	pressure	bar
t	time	s
T	temperature	K
u	flow velocity	m/s
$u(i)$	absolute uncertainty of component i	
$u_r(i)$	relative uncertainty of component i	
v	molar volume	m^3/mole
$\dot{V}$	volume flow rate	μL/min
w_i	IHM model weight of component i	
x	mole fraction	

Greek symbols

η	dynamic viscosity	Pas
μ_i	chemical potential of component i	J/mole
ρ	Density	kg/m^3
σ_i	surface or interfacial tension	N/m^2

Kurzfassung

Experimentelle Daten zu Flüssig-flüssig-Gleichgewichten sind wichtig für viele Anwendungen von der Auslegung von Extraktionsanlagen bis hin zu Umweltaspekten wie die Löslichkeit von organischen Substanzen in Wasser. Dennoch benötigen konventionelle Messmethoden sehr viel Zeit und Probenmengen.

Daher wird im ersten Teil dieser Arbeit ein Messaufbau für die zeit- und materialeffiziente Vermessung von Flüssig-Flüssig-Gleichgewichten in parallelen mikrofluidischen Strömungen vorgestellt. Der Messaufbau verknüpft die Vorteile von Mikrofluidik und Raman-Spektroskopie. Die kleinen Dimensionen des Mikrokanals führen zu einer schnelle Gleichgewichtseinstellung bei gleichzeitig niedrigem Probenverbrauch, wobei die Raman Spektroskopie eine schnelle in-situ Quantifizierung aller Komponenten ermöglicht. Der Messaufbau wurde erfolgreich validiert durch die Vermessung des Flüssig-flüssig-Gleichgewichts des ternären Systems Cyclohexan - Methanol - Toluol.

Um die höchste Effizienz und Nutzerunabhängigkeit zu erreichen, wurde der Messaufbau im zweiten Teil dieser Arbeit so angepasst, dass ein automatisierter Arbeitsablauf von Kalibration bis zur Datenanalyse möglich ist. Dafür werden Reinstoffe in einem Mikromischer vorgemischt, um innerhalb eines Experimentes mehrere Datenpunkte für die Kalibration oder das Flüssig-flüssig-Gleichgewicht zu generieren. Mit Hinblick auf die Validierung sowohl der integrierten Kalibration als auch der Gleichgewichtsmessung, wurden die beiden ternären Systeme Cyclohexan - Toluol - Methanol und *n*-Heptan - Acetonitril - Ethanol vermessen.

Eine stabile parallele Strömung kann allerdings für viele industriell relevante wässrig-organische Systeme nicht eingestellt werden, da diese zu einer Propfenströmung tendieren. Propfenströmungen haben den Vorteil, dass innere Zirkulationen in den Propfen den Massentransport erhöhen, was eine schnellere Gleichgewichtseinstellung bewirkt. Daher wird im dritten Teil dieser Arbeit ein Messaufbau für die Bestimmung von Flüssig-flüssig-Gleichgewichten in mikrofluidischen Propfenströmungen vorgestellt. In dem Messaufbau wird eine Kapillare gegen die Strömungsrichtung bewegt. Dabei wird je ein Propfen von entweder wässriger oder organischer Phase während der Aufnahme der Ramanspektren im Laserfokus gehalten. Das Vormischen der Komponenten, die Berechnung der Längen und Geschwindigkeiten der Propfen und die Raman-Messungen finden in beiden Phasen voll automatisiert statt. Der Messaufbau und die Versuchsdurchführung wurden erfolgreich am ternären System Aceton - Toluol - Wasser validiert. Mit beiden vorgestellten Aufbauten ist es nun möglich, die Flüssig-flüssig-Gleichgewichte vieler verschiedener Systeme höchst effizient zu vermessen.

Abstract

Experimental liquid-liquid equilibrium (LLE) data are of major importance for many applications ranging from extraction column design to water partitioning of organics in the environment. However, conventional LLE experiments are time consuming and need large sample volumes.

Therefore, in the first part of this work, a measurement setup is presented for the time- and material-efficient determination of LLE data. The measurement setup combines the advantages of microfluidics and Raman microspectroscopy. The small dimensions of the used H-cell microchannel lead to rapid equilibration and small sample consumption while Raman microspectroscopy allows for rapid in-situ quantification of all components. The measurement setup has successfully been validated by measuring the LLE of the ternary system cyclohexane – methanol – toluene.

Since highest efficiency and user independence can be reached by automation, the setup has been adapted in the second part of the manuscript to allow for an automated workflow from calibration to data analysis. Pure components are premixed online using a micromixer resulting in a closed system with the additional advantage of avoiding potential losses of volatile components. In the automated setup, one experiment generates several data points for calibration and LLE data measurements. The automated setup and workflow are successfully validated with respect to both the integrated calibration and the LLE measurements. For this purpose, the two ternary systems cyclohexane – toluene – methanol and *n*-heptane – acetonitrile – ethanol were studied.

However, a stable parallel microfluidic flow regime cannot be established for numerous industrially relevant aqueous-organic LLE systems since they tend to form plug flows. These plug flows have the advantage that inner circulations in the plugs enhance the mass transfer, leading to a much faster equilibration. Therefore, a measurement setup is presented for LLE in microfluidic plug flows in the third part of this thesis. In the setup, a capillary is moved against the flow direction. Thereby, one plug of either aqueous or organic phase is hold in the laser focus during the Raman measurement. Full automation is established for the premixing of the components, the calculation of the plug lengths and speeds and the Raman measurements of both phases. The setup and automated measurement procedure are successfully validated for the LLE of the ternary system acetone – toluene – water.

Using both presented setups, it is now possible to measure the liquid-liquid equilibria of many different systems in a highly efficient manner.

Chapter 1

Introduction

Experimental liquid-liquid equilibrium (LLE) data is needed in many areas, e.g., for extraction column design in the chemical industry (Kontogeorgis et al., 2021), sample extraction in analytical chemistry (Tang et al., 2016) or for environmental assessments of novel biofuels with respect to their partitioning behavior with water and the resulting impact of aqueous toxicity (Anastas and Zimmerman, 2016; Dechambre et al., 2017; Heger et al., 2018).

The assessment of the mutual partitioning of new biofuels or biofuel blends with water motivated this work which was funded by the Cluster of Excellence 'Tailor-Made Fuels from Biomass'. The research of this Cluster of Excellence refers to second-generation biofuels derived from lignocellulosic biomass, which have no competition with food production. While searching for the optimal biofuel candidate or blend the focus is set in equal measures on the production chains, the combustion characteristics and environmental aspects. Since many biofuel candidates and blends were considered, also many possible liquid-liquid systems have attracted interest, both in terms of sample extraction during production or processing and regarding environmental aspects such as the mutual solubilities of new biofuels or biofuel blends and water.

In the chemical industry, liquid-liquid extraction is an important separation when distillation cannot be applied or only with an excessive energy consumption, e.g. due to an azeotrope. Liquid-liquid extraction allows to separate large quantities of liquids at low cost and with relatively simple equipment and is therefore also used to enrich a component in a phase with a lower volume. A subsequent distillation step can thus be much more efficient and cost-effective.

The prediction of LLE data remains a great challenge today, because LLE occur

due to complex molecular interactions in liquid mixtures (Case et al., 2011). Thus, experimental LLE data is of major importance. Despite this importance, LLE data is scarce, in particular for multicomponent systems: LLE data is available for 8193 ternary, 1277 quaternary and only 131 quinary systems from Dortmund Data Bank (DDBST GmbH, 2023). Considering that 8193 ternary systems could be formed with only 38 unique substances and thousands of new substances are added to CAS REGISTRY (2023) daily, it is evident that needed LLE data is mostly unavailable. Consequently, experiments are unavoidable.

Conventional LLE experiments are time consuming and need large sample volumes of up to tens of milliliters (Weir and de Loos, 2005). The need for larger samples is particularly an issue in the screening of new systems, where components are often of limited availability. Thus, two improvements are desirable for LLE experiments: firstly, smaller sample sizes; and secondly, fast and reliable data collection.

1.1 Structure of this Thesis

In this work, a new measurement principle is presented which combines microfluidics and Raman microspectroscopy for highly efficient LLE measurements.

Chapter 2 presents the current state of the art for the fundamentals and measurements of liquid-liquid equilibria. First, some fundamental rules for the appearance and application of liquid-liquid equilibria are presented. Then, the current measurement methods, from conventional experiments for fully LLE measurements to microfluidic approaches for the determination of distribution coefficients are presented. Finally, further insight is given in liquid-liquid microfluidic flows and the in-situ concentration measurement using Raman spectroscopy.

In Chapter 3, the proof of concept to efficiently determine liquid-liquid equilibria in parallel microfluidic flows using Raman microspectroscopy is presented. Due to the small dimensions of the used microchannel, the equilibration is rapid and the sample consumption is minimized. Raman microspectroscopy allows for in-situ quantification of all components with high spatial resolution. These features allow the determination of full ternary liquid-liquid equilibria in microfluidic flows, going beyond the measurement of partition coefficients for the first time.

In Chapter 4, the previously shown setup is automated. An automated workflow

and setup are presented which include online premixing of components to calibrate and measure LLE data with high efficiency and user independence. Several data points for both calibration and LLE data measurements can now be generated automatically in one experiment.

Since especially the industrially relevant aqueous-organic systems tend to form plug flows rather than parallel flows, Chapter 5 presents an alternative measurement setup for the determination of LLE in microfluidic plug flows. To hold one plug in the laser focus during the Raman measurement, a capillary is moved against the flow direction. Full automation is established for premixing of the components, calculation of the droplet lengths and speeds and the Raman measurements of both phases.

The work is summarized in Chapter 6. Finally, perspectives for future work are given.

Chapter 2

State of the Art

In this chapter, the theoretical background of liquid-liquid equilibria and the state of the art of LLE measurements are presented. In Section 2.1, a short introduction is given to the fundamentals of LLE appearance and the application of LLE for industrial separation processes. Section 2.2 gives an overview of different experiments for the determination of LLE data, starting with conventional batch experiments with large sample volumes over newer automated approaches which still use standard analytics to new microfluidic approaches for the determination of distribution coefficients. In Section 2.3, more detailed insight is given on the different liquid-liquid microfluidic flow regimes. Since Raman spectroscopy is very suitable for use in microfluidics, the fundamentals and applications of this measurement technique are presented in Section

2.4. Finally, the idea of an efficient measurement principle which combines microfluidics and Raman spectroscopy for highly efficient LLE experiments is presented in Section 2.5 which underlines the significance of this work.

2.1 Fundamentals and Application of Liquid-Liquid Equilibria

Two liquid phases are in thermodynamic equilibrium when temperature T , pressure p and the chemical potentials μ of all components in both phases are equal where the chemical potential of a component i is the partial molar Gibbs free energy of this component:

$$\mu_i = \left(\frac{\partial G}{\partial n_i}\right)_{T,p,n_{j\neq i}} . \tag{2.1}$$

In thermodynamic phase equilibrium, the total Gibbs free energy of the system is at a minimum (Frank et al., 2008). Liquid-liquid equilibria can occur when mixtures show strongly non-ideal mixing behavior mostly due to the different polarities of the various components of the mixture. When the excess Gibbs energy of the mixture, which describes the deviation of the mixture behavior from the ideal mixture behavior, would become to large in the theoretical consideration of a single-phase mixture, the system splits into two phases to minimize the overall total Gibbs free energy. The compositions and phase properties of the two separated phases can differ to a large extent, especially for systems where two components are nearly immiscible.

Liquid-liquid equilibria form the basis of liquid-liquid extraction processes which use the differing solubility of one solute in two immiscible liquid phases for separation by enrichment of this solvent in one of the phases. The ratio of the volumes of these two phase can thereby be influenced by a clever choice of the total composition over both phases. The distribution coefficient

$$K_i = \frac{x_i'}{x_i''} \tag{2.2}$$

quantifies the ratio of the mole fractions of a component i between the two phases $'$ and $''$. This mole fraction ratio depends on the global concentration but is constant

along a tie line for constant temperature and pressure conditions (see Figure 2.1).

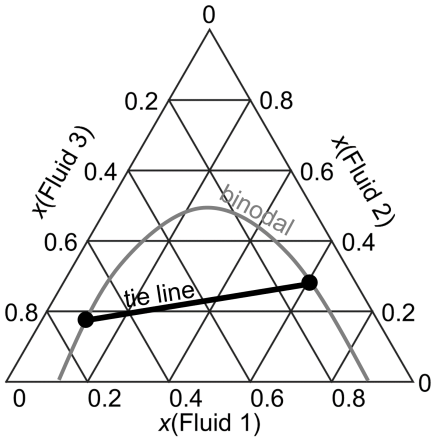

Figure 2.1: Representation of a ternary liquid-liquid equilibrium in a triangular phase diagram.

For the optimal design and operation of liquid-liquid extraction columns, not only distribution coefficients are relevant but also the concentration-dependent mutual solubility between the feed and solvent phase and thus the full LLE data, i.e. the concentrations of all components in both phases.

Liquid-liquid equilibria can be strongly temperature-dependent but are only hardly influenced by pressure (Raal and Mühlbauer, 1997). A change of the temperature can therefore change the position of the binodal and thus the equilibrium distribution to improve the extraction efficiency.

In the last years, research in the field of liquid-liquid extraction is moving more and more in the direction of microfluidics. The short diffusion distances and large surface-to-volume ratios of microfluidic setups are especially beneficial for liquid-liquid extraction, which efficiency relies on effective liquid-liquid contacting (Assmann et al., 2013).

For the design and optimization of conventional or microfluidic liquid-liquid extraction processes, accurate and reliable LLE data is needed. Possible measurement methods are therefore presented in the following section.

2.2 Determination of Liquid-Liquid Equilibria

Generally, three types of experimental methods are used for the determination of liquid-liquid equilibrium data (Frank et al., 2008):

- optical turbidity measurements as function of concentration (by titration),
- optical turbidity measurements as function of temperature
- and direct analysis of the equilibrated phases.

Turbidity measurements, also known as cloud point measurements, make use of the fact that a starting clear single-phase mixture becomes cloudy once a second liquid phase is formed in the moment when the (temperature-dependent) miscibility gap of a system is reached. To conduct a turbidity experiment, a single-phase mixture of known composition is placed in a tempered equilibrium cell. Then, either a pure component or mixture with varying composition is titrated or the temperature is varied until the mixture becomes cloudy. By varying the temperature, the upper and lower critical solution temperatures of a mixture at given composition can be determined. Using titration, the position of the binodale curve can be determined. For systems with three or more components, the turbidity measurements only give information about the binodale curve and cannot detect the positions of the tie lines.

In the direct analysis method, a mixture with a global concentration in the miscibility gap is prepared and tempered at a desired temperature. When the liquid-liquid equilibrium is reached and the phases are separated, samples are drawn from the two co-existing phases and the compositions of both phases are analyzed (Frank et al., 2008). This method has the greatest experimental effort but is quantitative and gives additional information about the tie lines of the systems to provide full LLE data sets. Therefore, the focus in the following subchapters is on analytical methods based on the concentration determination of the equilibrated phases.

2.2.1 Methods Using Standard Analytics

In conventional LLE experiments, an equilibrium cell with a typical volume of some centiliters is used. This equilibrium cell is placed in an oven or water bath for accurate temperature control. Typically, the components are introduced, thoroughly stirred for some hours until the liquid-liquid equilibrium state is reached and then

the phases are allowed to separate. Afterwards, samples are withdrawn from the two phases which are commonly analyzed via standard analytical methods like gas or liquid chromatography.

This conventional procedure has to be repeated for each individual tie line. Therefore, the conventional approach is very elaborate and time-consuming and needs large sample volumes (Weir and de Loos, 2005).

To improve the speed and reliability of the analytical approach, automation has been shown to be effective in various applications (Prabhu and Urban, 2017). For LLE measurements, the efficiency improvement by using automation has been demonstrated combining an autosampler with standard analytical methods like gas or high-performance liquid chromatography (Dechambre et al., 2014a; Kuzmanović et al., 2003). However, the employed standard analytical methods take long analysis time for each sample and are therefore often the bottleneck in these new automated approaches. Additionally, an internal standard is needed in many cases, which increases the overall consumption of chemicals (Grob and Barry, 2004).

Thus, more time- and material-efficient measurement techniques are desirable to determine LLE data, especially when screenings of new systems have to be conducted where many experiments are needed and some compounds are only available in very small amounts.

2.2.2 Microfluidic Approaches

In the last years, the field of microfluidics has received more and more attention for various applications in chemical industry, biotechnology and medicine (Whitesides, 2006; Zhao and Middelberg, 2011). The small dimensions of the microfluidic setups result in small sample volumes, rapid equilibration and good control of fluid flows (Whitesides, 2006).

When two partially miscible or immiscible fluids are brought into contact in a microfluidic device, a liquid-liquid microfluidic flow is established. Compared to standard liquid-liquid extraction applications, the interfacial area and thus the surface-to-volume ratio is increased enhancing mass transfer. The high potential of microfluidics for liquid-liquid extraction processes has been repeatedly shown as thoroughly reviewed by Assmann et al. (2013), Ciceri et al. (2014), Wang and Luo (2017) and Xu and Xie (2017). Using microfluidics, mass transfer rates can be increased by up to

three orders of magnitude in comparison to conventional extraction processes (Wellsandt et al., 2015). Hence, these microfluidic approaches have the potential to replace conventional established macroscopic methods in the long term despite the fact that till now, there is no breakthrough in the implementation for industrially relevant separations (Wellsandt et al., 2015). According to Wellsandt et al. (2015), the main reasons for the still missing breakthrough are that the phase separation is difficult, the throughput is low and that the scalability is limited.

These restrictions do not matter when regarding the measurement of phase equilibrium data. Here, the small throughput and the fast equilibration are strongly beneficial in order to increase the efficiency of LLE measurements regarding time and material consumption. That microfluidics can be used for the efficient determination of partition coefficients has repeatedly been shown, with the first approaches based on ex-situ standard analytical methods like high performance liquid chromatography (Alimuddin et al., 2008; Kralj et al., 2007), gas chromatography (Jovanovic et al., 2011) or (spectro-)photometric methods (Poulsen et al., 2015; Susanti et al., 2016). Standard analytical methods require phase separation at the end of the microchannel. Additionally, especially the chromatographic methods require laborious preparation of the samples and long analysis times. Consequently, the advantage of the fast equilibration times is lost compared to the long and laborious analysis.

The good optical accessibility of microfluidic systems allows in-situ concentration measurements in both liquid phases. As a consequence, the phase separation at the end of the microchannel can be avoided. The feasibility of in-situ measurements of partition coefficients has been shown for parallel laminar flows (Kim et al., 2000; Stephan et al., 2014), plug flows (Luther et al., 2014; Marine et al., 2009; Mary et al., 2008) and other micro-volume extraction systems (Abolhasani et al., 2015; Kitt and Harris, 2015; Carlsson and Karlberg, 2000). In microfluidics, concentrations are mostly determined in-situ by thermal-lens microscopy or fluorescence microscopy (Assmann et al., 2013). These measurement techniques do not allow for complete LLE measurements in ternary mixtures, because they only quantify one component in both phases and therefore measure only the partition coefficient of that component. The cross-solubility of both solvents and thus the full LLE data cannot be determined. This gap can be filled by the match of microfluidics with Raman spectroscopy which will be explained in detail in Section 2.4. Luther et al. (2014) use Raman spectroscopy for phase-specific measurements in segmented flows up to fast kHz-rates. To overcome

the weak Raman signal of one plug passing the laser focus, they use a photo-electric guard to identify the phase boundaries which triggers the photo-electric gate that ensures that only the laser light from one phase is analyzed (Luther et al., 2014).

Hübner and Minceva (2022) recently presented a microfluidic setup for the determination of LLE without any composition determination by an analytical device. In their setup, the LLE concentrations were calculated under knowledge of the position of the binodal curve from the measured densities of both saturated phases and the position of the phase boundary. The approach of Hübner and Minceva (2022) uses the assumption that the two liquid phases flow side by side at the same velocity, which is only valid if the ratios of the viscosities and densities are close to one . Furthermore, especially for the screening of new systems, the position of the binodal curve is often not known.

Microfluidics and Automation

To gain the highest efficiency for the LLE measurement, automation is unavoidable. Although much progress has been made in establishing microfluidics in a wide variety of research areas, most systems using microfluidic devices still require trained operators and tedious sample preparation procedures (Battat et al., 2022). The integration of external equipment and the automation of microfluidic devices and operations will advance the use of microfluidic approaches as an alternative to conventional methods (Battat et al., 2022).

Automation has already been successfully integrated using programmable syringe pumps in microfluidic approaches for chemical synthesis enabling smart platforms in which the products are synthesized and the yields are optimized without human intervention (Fabry et al., 2016; Houben and Lapkin, 2015; Liu and Jiang, 2017). In the automated microsystems, accurate program control is essential ensuring that all modules, including the injection systems and the real-time analytics which enable the closed-loop optimization, work well together (Liu and Jiang, 2017). In their review, Houben and Lapkin (2015) highlight the above highlighted Raman spectroscopy as potential sensor for a closed-loop optimization of non-fluorescent systems.

In a review on the automation of liquid phase microextraction (LPME) for sample pretreatment and analyte preconcentration in analytical laboratories, Alexovič et al. (2016) highlight the advantages of automated approaches which are easy-to-operate,

highly reproducible and can be conducted with high throughput and reduced sample consumption. The automation of LPME methods can be done through the use of autosamplers or programmable syringe pumps which enable reproducible propulsion, mixing and transport of fluids (Alexovič et al., 2016). According to Alexovič et al. (2016), automation is the necessary step towards a widespread application and commercialization. Nevertheless, Alexovič et al. (2016) also name the limits of automation which are the refilling of the syringes, the transport to posterior analysis and cleaning steps.

2.3 Liquid-Liquid Microfluidic Flows

As already mentioned in Section 2.2, contacting two immiscible liquid flows on the microscale leads to rapid equilibration and is thus the basis for very efficient determination of LLE data. Regarding the implementation of a measurement technique, the microfluidic flow regime plays an important role for the extraction efficiency and the practicability. Therefore, this chapter will present the occurrence and application of different flow regimes while highlighting the respective flow characteristics and resulting advantages and disadvantages. In this work, the focus will be on 2-phase liquid-liquid flow regimes.

2.3.1 Flow Regimes

The properties and the flow regime of a two-phase flow depend on the channel geometry, the phase characteristics, the volume flow rates of both fluids and instabilities at the liquid-liquid interface (Günther and Jensen, 2006; Zhao and Middelberg, 2011). At the microscale, interfacial effects between the two phases or between wall and fluid are dominant. Especially the surface-wetting properties of the liquid phases with the wall have a major influence on the established flow regime (Günther and Jensen, 2006). In addition, the geometry of the contact point of the two fluids plays an important role. Typical flow regimes that are formed by two liquid fluids in a straight microchannel are parallel flow, plug flow and droplet flow. Mixed forms or chaotic flow regimes are also possible (Yao et al., 2021).

Since the established flow regimes depend on the microchannel surface material and geometry, the fluid properties and the volume flow rates, the flow regime can hardly

be predicted (Zhao and Middelberg, 2011; Yao et al., 2021). However, Yao et al. (2021) present in their review that a combination of the capillary number

$$\mathrm{Ca} = \frac{\eta u}{\sigma}, \tag{2.3}$$

which represents the relative importance of viscous to surface tension forces, and the Reynolds number

$$\mathrm{Re} = \frac{\rho d u}{\eta}, \tag{2.4}$$

which shows the relative importance of inertial to viscous forces, can be used for general correlations of the flow regime (Figure 2.2). The dimensionless capillary and Reynolds numbers depend on the dynamic viscosity η, the flow velocity u, the surface or interfacial tension σ, the density ρ and a characteristic length scale d. Thus, for fixed phase properties and microchannel geometry, the flow velocity remains the only variable. Plug flows (in Figure 2.2 called slug flows) occur when interfacial forces dominate at small $Ca_C Re_C^{0.5}$ and $Ca_D^{0.7} Re_D^{0.5}$ values and thus relatively low and similar volume flow rates (Yao et al., 2021; Kashid et al., 2005). Parallel flows occur when inertial or viscous forces of the dispersed phase dominate at high $Ca_D^{0.7} Re_D^{0.5}$ values, when the interfacial tension is overcome and both phases wet the channel (Yao et al., 2021). When strong inertial and viscous forces of the continuous phase dominate at high $Ca_C Re_C^{0.5}$ values, a droplet flow regime occurs where the diameter of the droplets is smaller than the channel width (Yao et al., 2021).

For microfluidic liquid-liquid extraction, parallel and plug flow regimes are of major importance since they offer high reproducibility and stability and can be established with a phase ratio between the two co-flowing liquid phases near one. A phase ratio near one accelerates the overall equilibration for systems with similar diffusion coefficients in the two liquid phases and guarantees a good optical accessibility to both phases which will be important for the measurement of liquid-liquid equilibria in this work. Therefore, the fundamentals and special features of this two flow regimes will be described in detail in the following subsections.

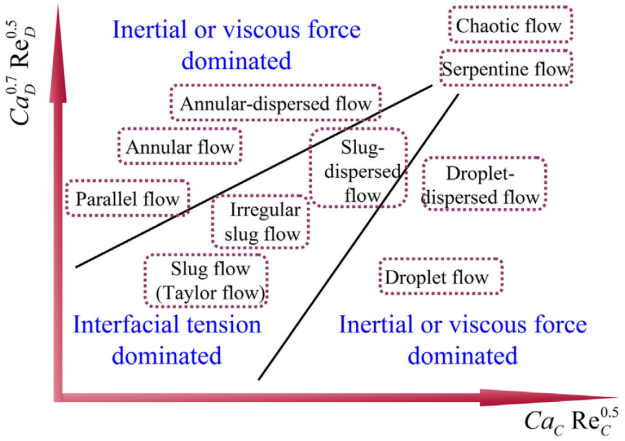

Figure 2.2: Schematic distribution map of the liquid-liquid flow pattern dependent on capillary and Reynolds number of continuous (C) and dispersed (D) phase (Yao et al., 2021).

Parallel Flow

In microfluidic devices, the influence of the gravity is negligible compared to the interfacial tension so that two liquid phases which are separated by gravity in conventional devices can flow next to each other on the microscale (Aota et al., 2009; Assmann et al., 2013). Due to the usually low Reynolds number in microfluidics, the flow regime is strongly laminar.

In a glass microchannel, the interface is curved towards the phase which preferably wets the hydrophilic glass surface (Aota et al., 2009). For a water-organic two-phase system, the interface is curved towards the aqueous phase. Xu and Xie (2017) mention in a review on microfluidic liquid-liquid extractors that there are two key components for the establishment of a stable laminar flow: The inlet structure and the interface stability. In most cases, a T- or Y-junction is used to establish a parallel liquid-liquid flow regime. The stability of the interface can be disturbed by Kelvin-Helmholtz (KH) instability and pressure imbalance, see Figure 2.3 (Xu and Xie, 2017). KH instability mainly arises due to velocity differences between the two co-flowing phases and causes the interface to move horizontally to the flow direction to form waves. With rising intensity, these waves can lead to an interface rupture where drops tear off. A pressure imbalance between the two co-flowing phases can also destroy a stable interface when the pressure difference across the interface overcomes the interfacial tension (Xu and Xie, 2017). Additionally, even small fluctuations in the volume flow rates can disturb

the surface.

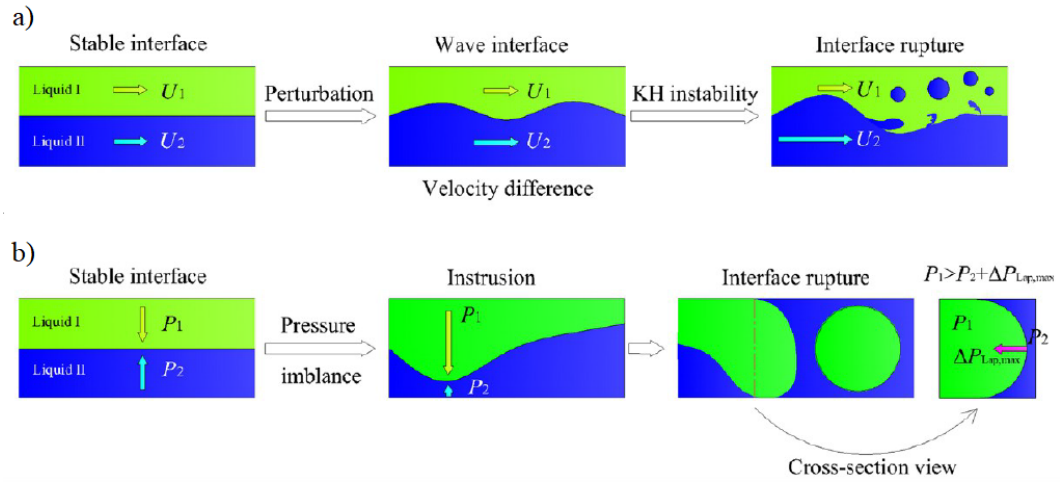

Figure 2.3: Destabilization of the interface in parallel microfluidic flows due to Kelvin-Helmholtz (KH) instability (a) and pressure imbalance (b). Adapted from Xu and Xie (2017).

A stabilization of the flow regime is possible by adding guiding structures to the channel surface or by selective surface modification (Aota et al., 2009; Xu and Xie, 2017; Hibara et al., 2016). Selective surface modification means that the surface is selectively patterned into hydrophobic and hydrophilic parts to stabilize the wall adhesion and thus position of the aqueous and organic phase, respectively. Using selective surface modification, a stable parallel flow can be maintained in a longer microchannel and even countercurrent parallel microflows are possible (Hibara et al., 2016).

Additionally, it has been theoretically and experimentally confirmed that fast velocities help to stabilize a parallel flow regime (Assmann et al., 2013). Here, the biggest drawback is that fast velocities limit the maximum residence time of the fluids in the microchannel and since the extraction is only diffusion-based in parallel microfluidic flows, the liquid-liquid equilibrium can eventually not be reached within the channel length (Assmann et al., 2013).

Separation of the side-by-side flowing liquids can easily be achieved by using a simple Y-splitter at the end of the microchannel. Since the position of the phase boundary can not perfectly be controlled and will be wavelike, the phases are usually split so that the product outlet stream is pure and the second outlet stream contains

small parts of the other phase. When both outlet streams are desired to be pure, the separation efficiency has to be increased by using different surface properties of the outlet channels, guiding structures or membranes (Assmann et al., 2013).

Plug Flow

Especially for the industrially relevant water-organic systems, the above named instabilities are highly relevant so that parallel flows are hard to establish in long microchannels. In a review on microfluidic liquid-liquid extractors, Xu and Xie (2017) found in the referenced work that all laminar flow microextractors without membranes are shorter than 7 cm. Since the mass transfer in parallel flows only takes place by diffusion and the mass transfer rates are low, the equilibrium is not always reached within the length of the microchannel. Consequently, the plug flow regime is the preferred flow regime when using water-organic systems.

Equilibration is much faster in plug flows than in parallel flows. The continuous phase which wets the channel walls forms a thin film between the plugs of the dispersed phase and the channel walls and increases the interfacial area by a factor of 3 to 4 compared to a parallel flow regime (Assmann et al., 2013). Larger surface-to-volume ratios and convective circulations within the plugs increase the mass transfer between the phases many times over, see Figure 2.4 (Kashid et al., 2005). Generally, the internal circulations are stronger and thus the mass transfer rates are higher at faster velocities so that this effect might even overcompensate lower residence times at higher velocities (Assmann et al., 2013). The enhanced mass transfer leads to a decreased solvent consumption. The great potential of microfluidic plug flow for liquid-liquid extraction has been shown: the extraction efficiency is enhanced compared to parallel microfluidic flow (Assmann et al., 2013). Additionally, plug flows display the advantages of easy control and excellent repeatability (Xu and Xie, 2017).

As stated above, plug flows occur when two immiscible liquid flows are contacted in a junction at relatively low and similar flow rates where interfacial forces dominate (Kashid et al., 2011). When a so-called T-junction is used, the channel piece with the dispersed phase intersects the main channel with the continuous phase perpendicularly. The tip of the dispersed phase enters the main channel and elongates due to shear forces and the pressure gradient till the neck of the dispersed phase thins and and breaks into a droplet (Teh et al., 2008). The formed droplets are thereby highly

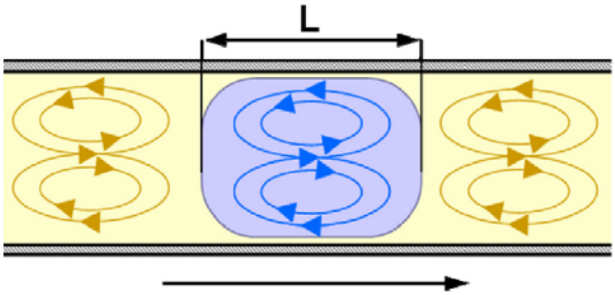

Figure 2.4: Convective cirulations within the single plugs of a plug flow. Adapted from Burlage et al. (2013).

monodisperse. The length of the plugs depends on the volume flow rates (Assmann et al., 2013).

Separating the two liquid phases of a plug flow is challenging since both phases flow alternately in the same channel. But using surface forces, which dominate at the microscale, separation is possible: For example, excellent separation can be achieved by using a wettability-based Y-splitter with one hydrophobic and one hydrophilic outlet channel or a membrane which is selectively wetted and passed by one of the phases (Assmann et al., 2013).

2.4 In-situ Concentration Measurements via Raman Spectroscopy

Raman spectroscopy relies on the Raman effect which occurs when light interacts with the molecular vibrations of the present molecules. The incoming light is scattered by the molecules for the most part elastically. But a small part of the light transfers a part of the energy to change the energy level of the molecules. The inelastically scattered light is emitted with a frequency that is changed exactly by this transferred energy of the molecular vibrations and which is therefore characteristic.

In practice, a sample is illuminated with a monochromatic laser light. The scattered Raman light is broken down into its individual wavelengths using a spectrometer, resulting in a typical Raman spectrum for each individual molecule. In this Raman spectrum, the intensity is plotted against the relative wavenumber which indicates the shift of frequency to the incoming laser light.

Since the intensity of the Raman signal is proportional to the number of molecules in the sample, Raman spectroscopy enables in-situ concentration measurement of all polyatomic components in gaseous, liquid or solid samples simultaneously. Raman spectroscopy is a very fast analytical method, needing only approximately one second per measurement (Chrimes et al., 2013). Furthermore, Raman spectroscopy is non-invasive and can provide high spatial resolution. Since it is capable of collecting spectra from very small volumes in the microliter range, it is very suitable for analysis in microchannels (Chrimes et al., 2013).

On the microscale, the use of confocal Raman microspectroscopy is extremely useful: the laser beam is focused at the point of interest within a transparent sample and can be moved to get concentration profiles along a line or even from a 2D or 3D profile (Everall, 2008).

For the measurement of phase equilibrium data, Raman spectroscopy has been successfully used to determine vapor-liquid equilibria in high-pressure view cells (Adami et al., 2013; Kaiser et al., 1992; Luther et al., 2013; Nakayama et al., 2007; Schuster et al., 2014; Stratmann and Schweiger, 2002). Thus, the accuracy of Raman spectroscopy can be sufficient for phase equilibrium measurements.

The combination of Raman spectroscopy and microfluidics is flexible, applicable in a lot of different situations and has a rapidly growing popularity across a wide range of application fields (Chrimes et al., 2013). Raman spectroscopy and microfluidics have also proven to be very suitable for highly efficient phase equilibrium measurements for both vapor-liquid equilibria and liquid-liquid equilibria (Luther et al., 2014, 2015; Nelson et al., 2018).

The main challenge using in-situ analytics is the fact that a plug flow is a non-continuous, segmented flow meaning that mechanisms for phase-selective data acquisition are needed. This is particularly difficult since the phase distribution and consequently the droplet length are not predictable for unknown LLE systems. Furthermore, a Raman signal from a single plug crossing a fixed measurement volume is often too weak for a precise quantitative analysis. Luther et al. (2014) accumulate the Raman signals from numerous droplets using a photo-electric gate. Here, averaging spectra of multiple plugs is required, and it is not possible to investigate one singular plug.

Since Raman signals of different liquid components are strongly overlapping, accurate methods for spectra evaluation are required when small concentrations need to be

quantified precisely. Especially, the water signal analysis is quite challenging for low water concentrations in organic phases since the Raman signal of water is very weak and changes its shape significantly due to disappearing hydrogen bonds (Giraudet et al., 2017).

2.5 Contribution of this Thesis

This chapter has shown that there is a need for new and efficient measurement methods for the determination of liquid-liquid equilibria since conventional methods need too much time and material especially for the screening of new systems. Since the use of microfluidics for liquid-liquid extraction and for the determination of distribution coefficient has been proven, it is obvious that microfluidics can also be used for the efficient measurement of full LLE data. The determination of full LLE data thereby requires a measurement technique that allows for the simultaneous quantification of all components. Ideally, the concentration determination should take place in-situ in the microchannel to avoid sampling and associated loss of time and accuracy due to volatile components. All these requirements for analysis technology are met by Raman spectroscopy. Therefore, in this thesis, microfluidics is combined with in-situ Raman spectroscopy for the time- and material-efficient determination of LLE data. The small dimensions of the microfluidic systems lead to rapid equilibration and small sample consumption (Section 2.2.2). Raman spectroscopy allows for rapid in-situ quantification of all components (Section 2.4).

Determination of LLE Using Microfluidics and Raman Microspectroscopy
First, the proof of concept of the determination of liquid-liquid equilibrium data using Raman spectroscopy is presented in Chapter 3. An H-cell microchannel is used in which a steady-state parallel flow regime is established which allows for the determination of Raman spectra at fixed measurement positions. The ternary system cyclohexane - methanol - toluene is measured and compared to literature data for validation.

Automated LLE Measurements from Calibration to Data Analysis
Since many applications have shown that highest efficiency and user independence can be reached by automation, an automated setup and workflow from calibration to data analysis for the determination of liquid-liquid equilibrium data using Raman microspectroscopy and a microfluidic platform are presented in Chapter 4. Pure

components are premixed online using a micromixer resulting in a closed system with the additional advantage of avoiding potential losses of volatile components. In the automated setup, one experiment generates several data points for calibration or LLE data measurements. The two ternary systems cyclohexane – toluene – methanol and *n*-heptane – acetonitrile – ethanol are measured and compared to literature data for validation.

LLE using Raman and Single Droplet Tracking in Microfluidic Plug Flow Since most of the industrially relevant water-organic LLE systems tend to form microfluidic plug flows, a second measurement setup has been built up for the determination of LLE in microfluidic plug flows which is presented in Chapter 5. The used capillary can be moved against the flow direction to hold one plug in the laser focus during the Raman measurement. To transfer the high efficiency of the first measurement setup, full automation is established for the premixing of the components, the calculation of the droplet lengths and speeds and the Raman measurements of both phases. The ternary system acetone - toluene - water is measured and compared to literature data for validation.

With the accessibility to both parallel and plug flows, this thesis presents a new and efficient measurement principle for a wide range of liquid-liquid systems.

Chapter 3

Determination of LLE Using Microfluidics and Raman Microspectroscopy

In this thesis, microfluidics is combined with in-situ Raman microspectroscopy for the time and material efficient determination of LLE data. In the first step presented in this chapter, a stationary and strongly laminar parallel flow regime is selected to enable fixed measurements positions and thus a simple and temporally not limited measurement via Raman spectroscopy. A spiral microchannel is used for this purpose with which diffusion coefficients have already been successfully determined (Peters et al., 2017, 2020). The channel length of 1 m makes it possible to reach the equilibrium state even if the mass transfer between the two co-flowing phases only takes place by diffusion (Section 2.3.1). For the proof of concept, the ternary LLE of the system cyclohexane – toluene – methanol is investigated.

Contribution report: Writing the draft, pricipal author, planning and conducting the experiments, data evaluation.

3.1 Experimental Setup and Materials

In the experimental setup, Raman microspectroscopy is used for concentration measurements in a microfluidic chip. The used microfluidic chip is a reusable custom-made glass chip (Micronit, Netherlands) consisting of an upper and a lower glass plate (D263 glass) of 1000 µm and 700 µm thickness, respectively. An H-cell microchannel is wet-etched to the lower glass plate. The H-cell has the form of a spiral of length $L = 1$ m, width $W = 400$ µm and height $H = 40$ µm (Figure 3.1a). Four observation points $s1$ to $s4$ are defined at different distances from the channel inlet. At each observation point, Raman spectra are obtained along the measurement line perpendicular to the flow (Figure 3.1c).

After each experiment, the microchannel is cleaned and reused. The smooth surface of the glass material allows to measure different systems one after the other in the same chip without impurities from old measurements have to be expected (Peters et al., 2017).

The H-cell is connected to a push-pull syringe pump (PHD ULTRA, Harvard Apparatus, US), which supplies the inlets of the H-cell by either two 2.5 mL syringes or one 2.5 mL syringe and one 1 mL syringe (H-TLT, ILS Innovative Labor Systeme GmbH, Germany). Typically, half the volume of the inlet syringes is filled, leading to low sample consumption of 1.75 to 2.5 mL per experiment. PTFE tubing with an inner diameter of 300 µm, connection parts from PEEK and syringe filters with a pore diameter of 0.45 µm (MULTOCLEAR-PTFE, CS-Chromatographie Service GmbH, Germany) were used.

The composition of the fluids in the microchannel is determined by an inverse confocal Raman microscope (inVia, Renishaw, UK). In particular, the beam from a frequency-doubled Nd:YAG-laser of 100 mW at 532 nm is focused by a water-immersion objective (LUMPLFLN 60XW, NA=1, Olympus, Japan) (Figure 3.1b). The resulting confocal volume is 2 µm x 2 µm x 10 µm (LxWxH). The back-scattered Raman light is processed in a multichannel analyzer consisting of a spectrometer with a grating of 1800 grooves/mm and a cooled CCD camera.

The temperature control of the microfluidic chip consists of a water-flushed aluminum plate on top of the microfluidic chip. The water in the aluminum plate is delivered by a thermostat (CC-K15 Pilot One, Peter Huber Kältemaschinenbau AG, Germany). The temperature of the aluminum plate is controlled via an external

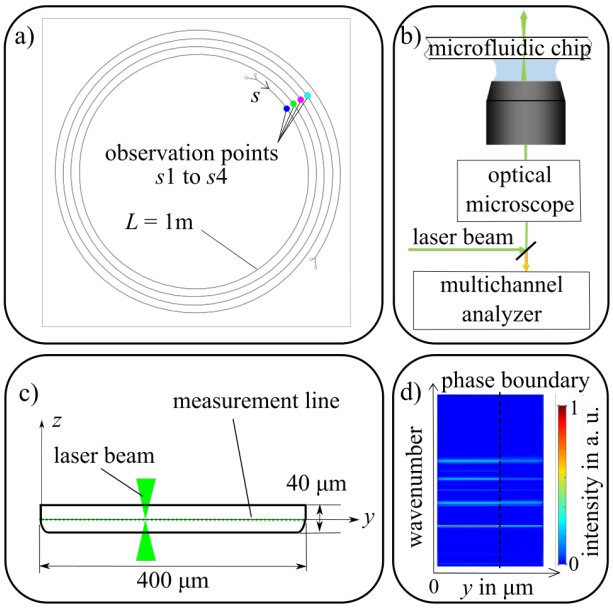

Figure 3.1: Experimental setup: (a) Microfluidic chip with microchannel and observation points $s1$ to $s4$. (b) Sketch of optical setup. (c) Channel cross-section with measurement line and laser beam. (d) Raman spectra over channel width y with visible change of intensities at phase boundary.

Pt 100 temperature sensor, which is connected to control the thermostat. Additionally, the temperature on the bottom side of the microfluidic chip is measured via a thermocouple. The temperature precision achieved in the microfluidic chip is ±0.5 K.

For the validation of the measurement setup, the LLE of the ternary system cyclohexane – toluene – methanol is investigated. The measured equilibrium concentrations are compared to literature data from Nagata (1984). All chemicals are used as received (Table 3.1).

Table 3.1: Used chemicals with supplier, specification and purity.

	supplier	**description**	**purity in %**
cyclohexane	VWR	Spectronorm	≥ 99.7 %
toluene	VWR	Spectronorm	≥ 99.8 %
methanol	VWR	Spectronorm	≥ 99.9 %

3.2 Data Analysis

All Raman spectra are evaluated quantitatively using the Indirect Hard Modeling (IHM) approach (Alsmeyer et al., 2004). IHM allows for the evaluation of mixture spectra with strongly overlapping spectral bands of the different components. Besides, non-linear effects, such as shifts of Raman bands, can be taken into account. Thus, IHM is particularly suited to analyze liquid phase spectra as has been demonstrated for a large variety of mixtures (Peters et al., 2017; Alsmeyer et al., 2004; Kriesten et al., 2008a; Blesinger et al., 2014; Beumers et al., 2016; Glass et al., 2017).

In IHM, the pure component spectra are modeled by a sum of pseudo-Voigt functions. A background signal is generated by the glass of the microchannel which is therefor modeled as additional component. All pure component models are combined to a mixture model. This model takes the non-linear effects in the mixture into account by enabling shifts in the parameters of the pure component models. In order to evaluate a mixture spectrum of unknown composition, this mixture model is fitted to the mixture spectrum by a weighted sum of the pure component models (Figure 3.2). As a result, areas of the pure components A_i in the Raman spectra are obtained. A detailed description of the IHM approach can be found in Alsmeyer et al. (2004).

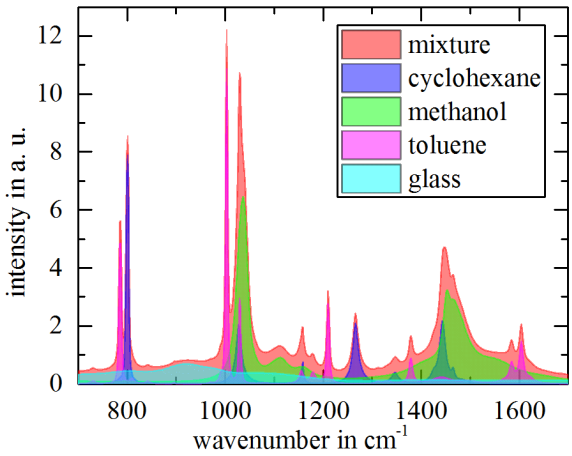

Figure 3.2: Fit of the mixture model to a mixture Raman spectrum using the IHM method.

From these areas A_i, the mole fractions x_i can be determined according to the following calibration model:

$$\frac{A_i}{A_j} = k_{ij}\frac{x_i}{x_j} + b_{ij}, \qquad \text{for } i = 1, ..., n-1 \tag{3.1}$$

$$\sum_{i=1}^{n} x_i = 1. \tag{3.2}$$

Here, x_i denotes the mole fraction of component i, and k_{ij} and b_{ij} are calibration constants. The reference component j was chosen to be j = cyclohexane for the calibration model of the cyclohexane-rich phase and j = methanol for the calibration model of the methanol-rich phase. Error propagation calculations considering the errors of the calibration constants k_{ij} and b_{ij} and the standard deviations of the area ratios A_i/A_j, resulting from the arithmetic averaging over the bulk phases, were performed to determine the relative uncertainties $u_r(x_i)$ and the uncertainties of the partition coefficient of toluene x'(toluene)/x''(toluene) between the cyclohexane-rich phase ($'$) and the methanol-rich phase ($''$).

3.3 Experimental Procedure

The initial compositions of the fluids are prepared by weight. The fluids are filled into the inlet syringes.

In the LLE experiments, channel inlet 1 is fed with a binary mixture of toluene and cyclohexane, where the composition is changed for different experiments. Channel inlet 2 is always fed with pure methanol. The volume flow rates are adjusted to ensure a Reynolds number $Re < 1$ in each phase and thus parallel laminar flow and steady state conditions (Häusler et al., 2012). Raman spectra are obtained every 2.5 µm along the measurement lines at observation points $s1$ to $s4$ with an exposure time of 1 second. The temperature was controlled to ensure a temperature of 298.15±0.5 K.

In order to evaluate the unknown concentrations in the LLE experiments, the Raman spectra have to be calibrated. For this purpose, the two channel inlets are fed with the same homogeneous solution of known composition. Multiple Raman spectra of this solution are obtained at observation point $s4$.

According to the expected concentration ranges for the equilibrium phases, separate calibration models are established for the cyclohexane-rich area and for the methanol-rich area as described before (Section 3.2). The calibration model of the cyclohexane-

rich area is based on 6 samples. The calibration model of the methanol-rich area takes 5 sample compositions into account. The respective concentration range can be well covered with this number of calibration samples in each case.

In order to determine the minimum retention time of the fluids in the microchannel to reach equilibrium, the mean concentrations of the bulk phases were measured at different retention times (Figure 3.3). The retention time was varied via the overall volume flow rate. The evaluation of the concentration profiles from $s1$ to $s4$ was monitored. A retention time smaller than three minutes has been found sufficient to reach the equilibrium state at which the net mass transfer between the two phases disappears.

In the LLE experiments, the syringe pump was adjusted to a volume flow rate of 2 µL/min for the 2.5 mL syringes and a volume flow rate of 0.8 µL/min for the 1 mL syringes, resulting in Reynolds numbers between 0.15 and 0.45 in the respective phases. Inlet 1 was fed with a binary mixture of toluene and cyclohexane by a 2.5 mL syringe. Simultaneously, inlet 2 was fed with pure methanol by either a 1 mL syringe or a 2.5 mL syringe. With the resulting volume flow ratios of 1:1 and 2.5:1, up to two tie lines per experiment can be measured by changing the syringe size of inlet 2 from a 1 mL syringe to a 2.5 mL syringe (Figure 3.4).

To determine equilibrium compositions, the measured concentrations are arithmetically averaged over the bulk phases at the last observation point downstream $s4$ (Figure 3.5). The ranges $y < 20$ µm and $y > 380$ µm are not taken into account in the evaluation, because of strong fluctuations in the Raman spectra due to the round channel side walls. Thus, for the analysis, the cyclohexane-rich bulk phase is defined to start at $y = 20$ µm and to end when the difference between two measurement points y becomes larger than $\Delta x = 0.02$. The methanol-rich bulk phase starts when the difference between two measurement points y becomes smaller than $\Delta x = 0.02$ and ends at $y = 380$ µm. The region next to the phase boundary is not taken into account for the determination of the equilibrium compositions.

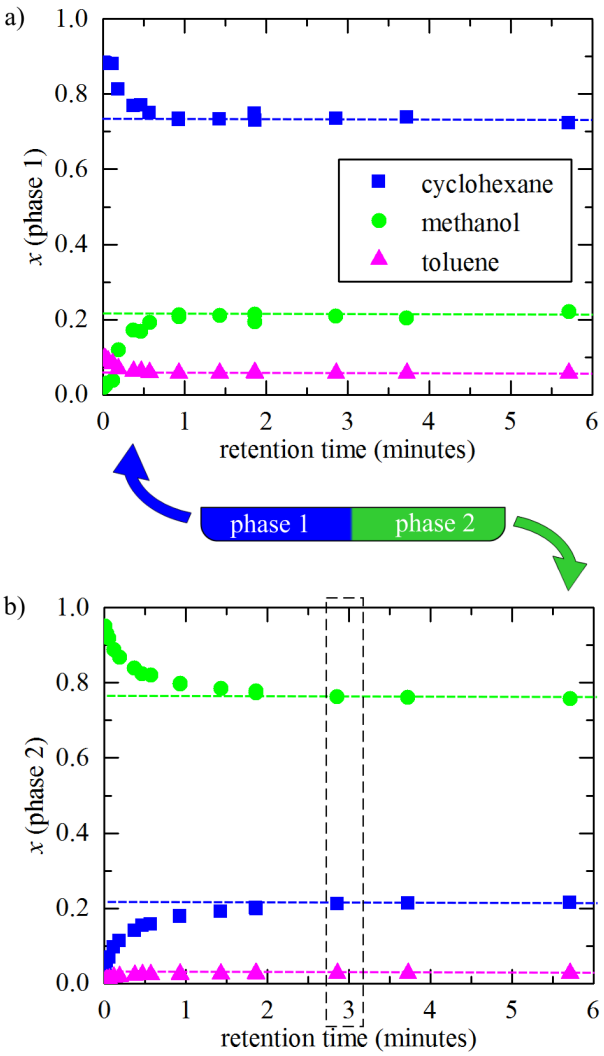

Figure 3.3: Concentrations averaged over bulk phases as a function of retention time: (a) cyclohexane-rich phase 1. (b) methanol-rich phase 2.

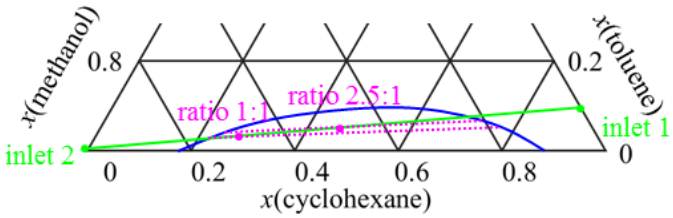

Figure 3.4: Schematic representation of mixing in LLE experiments: mixing of initial concentrations (green dots) at inlet 1 (cyclohexane + toluene) and inlet 2 (methanol) results in different global concentrations (red dots) for mixing ratios 1:1 and 2.5:1; blue line: binodale curve, red doted lines: expected tie-lines

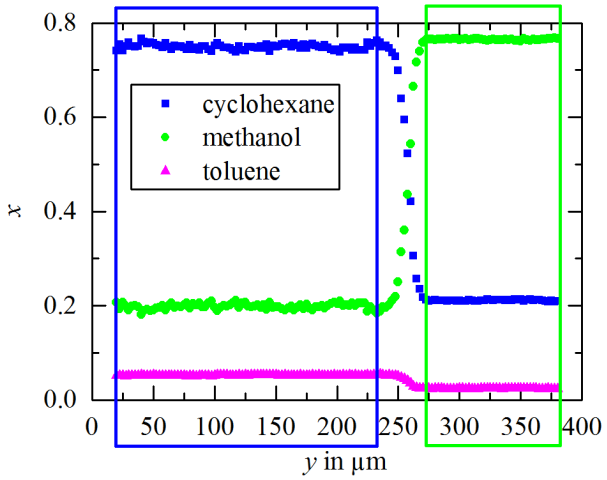

Figure 3.5: Spatially-resolved concentration profiles in liquid-liquid equilibrium at observation point $s4$; symbols denote single measurements from one experiment; blue box: cyclohexane-rich bulk phase; green box: methanol-rich bulk phase.

3.4 Results and Discussion

Concentration profiles of high spatial resolution are measured across the channel width at observation points $s1$ to $s4$ for all components. Figure 3.6 shows concentration curves of cyclohexane at observation points $s1$ to $s4$ for a typical experiment. At observation points $s1$ to $s3$, we still observe concentration gradients in the bulk phases and shifting of the interface. At observation point $s4$, equilibrium has been reached (see also Figure 3.3). Thus, the concentration profiles at $s1$ to $s3$ resolve the mass transfer as function of the residence time and provide additional information about the mass transfer until equilibrium is reached, e.g., the shift of the phase boundary and the equilibration time. Therefore, the setup could also offer the potential of measuring simultaneously mass transfer properties.

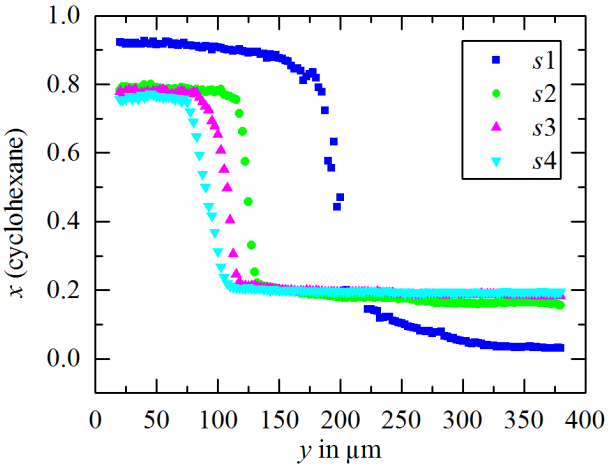

Figure 3.6: Mole fractions of cyclohexane at distances downstream $s1$ to $s4$; total volume flow 4 µl/min, volume flow ratio 1:1.

To measure the liquid-liquid equilibria, the measured equilibrium concentrations are averaged over the bulk phases at observation point $s4$ when the equilibrium is reached, as described in the experimental procedure. In this work, seven different equilibrium concentrations were investigated. The measured equilibrium concentrations and the related relative uncertainties are presented in Table 3.2. The provided relative uncertainties are calculated from error propagation calculations as described above. These relative uncertainties are regarded as conservative as they are up to 30 % larger than the standard deviations resulting from the arithmetic averaging of the mole fractions over the single measurements in the bulk phases as shown in Figure 3.5.

Table 3.2: Liquid-liquid equilibrium concentrations for the system cyclohexane ($x_1^{'}$,$x_1^{''}$) – toluene ($x_2^{'}$,$x_2^{''}$) – methanol ($x_3^{'}$,$x_3^{''}$) at $T = 298.15$ K and $p = 1.013$ bar.

$x_1^{'}$	$x_2^{'}$	$x_1^{''}$	$x_2^{''}$
0.8446	0.0189	0.1763	0.0072
0.8060	0.0289	0.1863	0.0116
0.7882	0.0377	0.1952	0.0157
0.7603	0.0416	0.2041	0.0184
0.7489	0.0522	0.2113	0.0241
0.6992	0.0689	0.2248	0.0337
0.6478	0.0820	0.2642	0.0462

Relative uncertainties u_r are $u_r(x_1^{'}) = 0.008$, $u_r(x_2^{'}) = 0.015$, $u_r(x_1^{''}) = 0.014$ and $u_r(x_2^{''}) = 0.018$.

Figure 3.7 shows the measured equilibrium concentrations in comparison to the literature data. All measured equilibrium concentrations and tie lines show excellent agreement with the data from Nagata (1984). The partition coefficient of toluene as function of the overall composition of toluene (Figure 3.8) is also in excellent agreement within the uncertainties considering that Nagata indicates an absolute uncertainty of $u(x) = 0.002$ for all mole fraction measurements (Nagata, 1984).

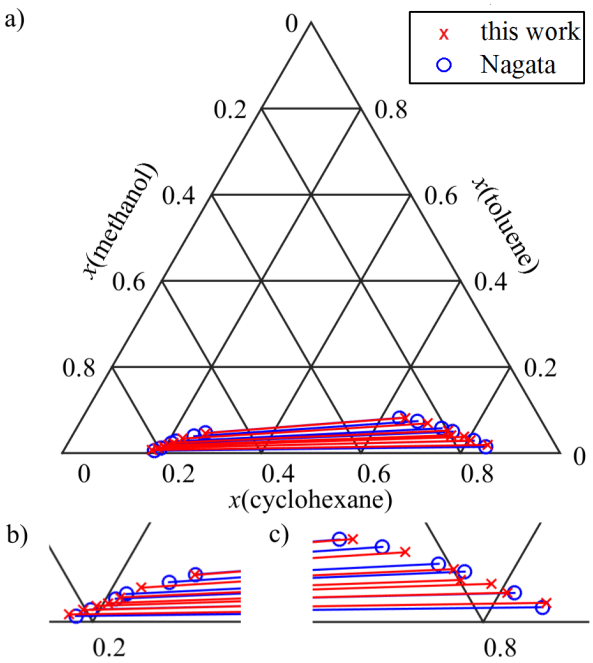

Figure 3.7: Tie-lines of the system cyclohexane – toluene – methanol at $T = 298.15$ K measured in this work and by Nagata (1984): (a) Complete phase diagram. (b) Zoom into methanol-rich phase. (c) Zoom into cyclohexane-rich phase.

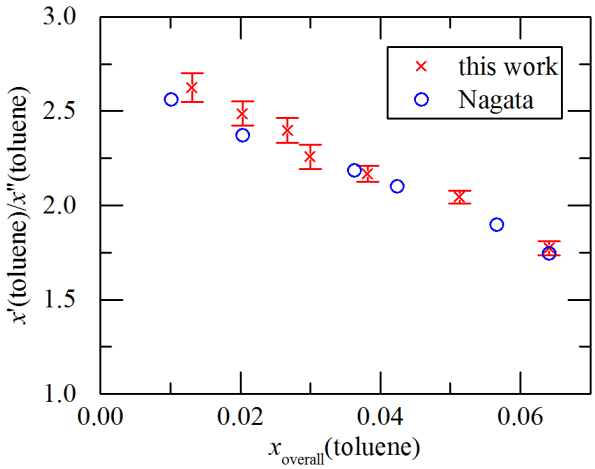

Figure 3.8: Partition coefficient of toluene between the cyclohexane-rich phase and the methanol-rich phase as function of the overall composition of toluene at $T = 298.15$ K measured in this work and by Nagata (1984).

3.5 Conclusions

We developed a promising measurement principle to obtain LLE data by combining microfluidics and Raman microspectroscopy. The measurement setup was successfully validated for the LLE of the ternary system cyclohexane – methanol – toluene at 298.15 K. The measured equilibrium concentrations are in excellent agreement with the literature data within the measurement uncertainties. Due to the small dimensions of the microfluidic setup, we see a rapid equilibration (< 3 minutes) and small sample consumption (about 2 ml per experiment). The combination with Raman microspectroscopy leads to an analysis time of about 3 minutes per observation point. The overall time for LLE determination is now mainly determined by the time for sample preparation, start-up and spectra evaluation. The improvement of these steps will be part of Chapter 4. Thus, the developed measurement principle has the potential to become an efficient tool for the determination of liquid-liquid equilibria.

Chapter 4

Automated LLE Measurements from Calibration to Data Analysis

In Chapter 3, we combined microfluidics and Raman microspectroscopy for the efficient determination of ternary LLE data. The main advantages of using microfluidics are the small dimensions resulting in small sample volumes as well as rapid equilibration. Still, there are two bottlenecks remaining: the preparation and start-up times of the experiments. The sample preparation is laborious and time-consuming compared to the autosampler setup (Dechambre et al., 2014a; Kuzmanović et al., 2003). In addition, about 30 minutes start-up time is needed for each experiment until steady-state flow is reached due to the start-up of the syringe pumps and to remove air bubbles from the system. As result, only one calibration point or one equilibrium point can be measured per experiment, leading to the fact that the times for preparation and start-up are 10 times higher than the times actually needed for equilibration and measurement (Chapter 3). Reducing these times for preparation and start-up is a central result of the development presented in this chapter.

Additionally, there is another bottleneck remaining: reliable concentration measurements by Raman spectroscopy require accurate calibration which is again a laborious and time-consuming step. There are a few examples for integrated calibration in

Reprinted (adapted) with permission from J. Thien, L. Reinpold, T. Brands, H.-J. Koß, and A. Bardow, "Automated Physical Property Measurements from Calibration to Data Analysis: Microfluidic Platform for Liquid-Liquid Equilibrium Using Raman Microspectroscopy.", *Journal of Chemical & Engineering Data*, vol. 65(2), pp. 319-327, 2020.

Contribution report: Writing the draft, pricipal author, conceptual design of the setup and the measurement procedure, planning and conducting the experiments, data evaluation.

the literature, e.g. using valveless microsystems (Blasco et al., 2007) and for Raman vapor-liquid equilibrium measurements (Liebergesell et al., 2017). These examples show that the integration of calibration in the experimental workflow saves time and effort.

For determining liquid-liquid equilibrium data using Raman microspectroscopy and a microfluidic platform with the highest efficiency, this chapter presents the automation of the setup introduced in Chapter 3 and an automated workflow from calibration to the actual data analysis. The chapter is structured as follows: First, we present the experimental details of the automated setup and workflow. Then, the experimental results are presented for the validation of the automated integrated calibration and for the LLE determination. For this purpose, we study the two ternary systems cyclohexane - toluene - methanol and *n*-heptane - acetonitrile - ethanol. Finally, for the proof of the novel concept, we compare the measured LLE data to literature.

4.1 Automated Setup and Workflow

The experimental setup for LLE measurements is sketched in Figure 4.1. Two fluids with a miscibility gap are contacted in a microchannel forming a parallel laminar flow at steady state conditions (Figure 4.1a). Feeding two immiscible phases to the two inlets helps to guarantee the desired flow regime of two phases in parallel. In our experiments, we did not encounter any other flow regimes (e.g., slug flow). The equilibration towards liquid-liquid equilibrium takes place by diffusion perpendicular to the flow direction. Concentration profiles are measured at several points along a measurement line perpendicular to the flow direction in-situ by Raman microspectroscopy (Figure 4.1b). More details of the setup are given below. The proof of principle of this experimental setup has already been presented in Chapter 3. In this chapter, the experimental setup is expanded by automated online sample preparation for highly efficient LLE measurements including their calibration.

In the expanded experimental setup, pure components are fed by inlet syringes and premixed in a micromixer (Figure 4.2). Thereby laborious, time-consuming and highly error-prone manual sample preparation is omitted. Manual sample preparation has always the risk of loss of volatile components during weighing (de Koning et al., 2009). Thus, the resulting closed system is a further advantage of the automated setup from calibration to actual data collection: the online mixing of the components

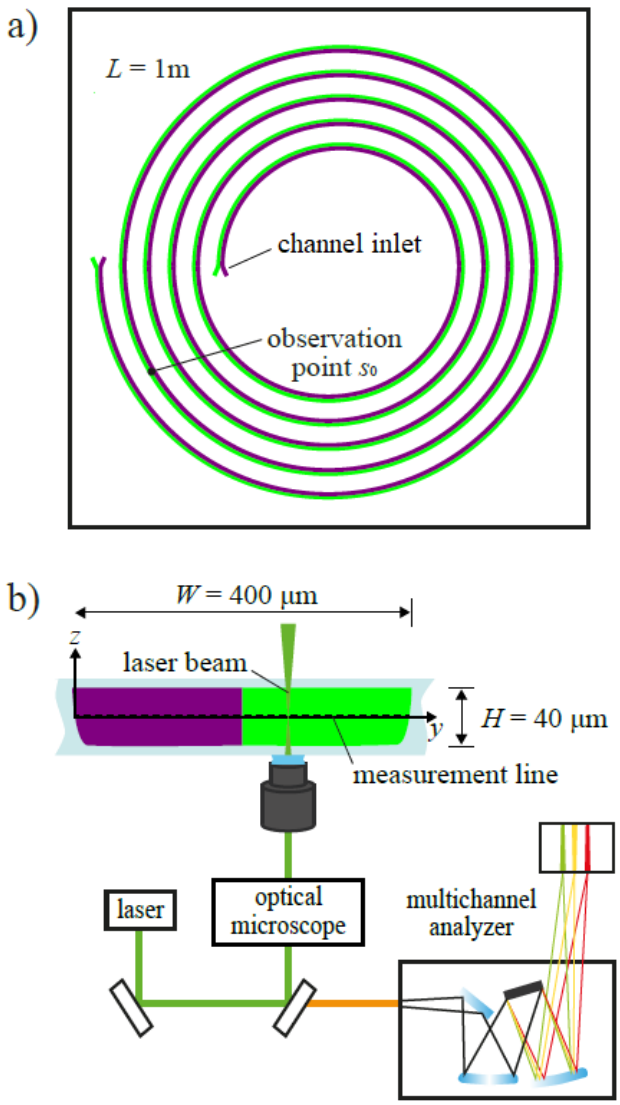

Figure 4.1: Experimental setup: (a) Top view of the microfluidic chip with microchannel and observation point s_o at a distance of 0.7 m from channel inlet. (b) Integration of microfluidic chip (cross-sectional area at observation point s_o) in optical setup consisting of laser, optical microscope, and multichannel analyzer.

and the in-situ concentration measurements avoid any risk of evaporation of volatile components. Additionally, the sample preparation is user-independent, which is an important advantage for all laboratories with varying staff.

Importantly, the volume flow rates can be adjusted via the inlet syringes such that the complete phase diagram is accessible. Thereby, either for calibration or LLE

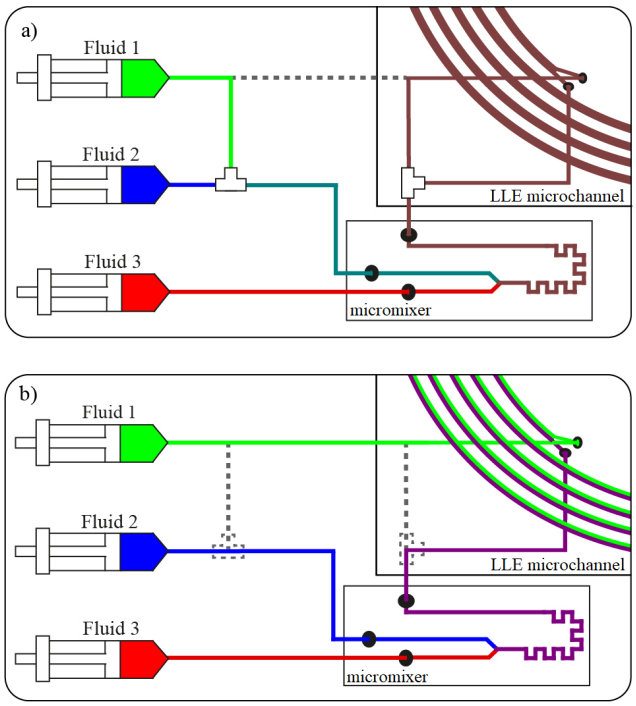

Figure 4.2: Mixing principle in experimental setup: (a) For calibration experiments, all components premixed in micromixer. (b) For LLE experiments, Fluid 2 and Fluid 3 premixed in micromixer and contacted with Fluid 1 in the microchannel.

data measurement, several data points can be generated in one experiment while needing only one time-consuming start-up period. For calibration experiments, all components are premixed in the micromixer leading to a constant concentration in the microchannel (Figure 4.2a). For LLE experiments, Fluid 2 and Fluid 3 are premixed in the micromixer and contacted with Fluid 1 in the microchannel (Figure 4.2b). Thereby, the components of a ternary mixture should be assigned so that the two premixed components 2 and 3 are completely miscible. Equilibration takes place due to the diffusional mixing between the two side-by-side flowing fluids until equilibrium is reached.

4.2 Experimental Details and Materials

The microlfuidic chip already used for the proof of concept in Chapter 3 is also suitable for the integration in an automated setup. It is a reusable custom-made glass chip

(Micronit, Netherlands) with an H-cell microchannel in form of a spiral of length $L = 1$ m, width $W = 400$ µm and height $H = 40$ µm (Figure 4.1). Volume flows are adjusted to ensure that liquid-liquid equilibrium is reached at the observation point s_o at a distance of 0.7 m from channel inlet, which is the last observation point accessible with the current setup. Using the last observation point provides the longest contact time for the fluids to reach phase equilibrium. Raman spectra are obtained along the measurement line (Figure 4.1b). The measurement line is located in the middle of the microchannel in the z-direction. In practice, the z-position is identified as the position with the best signal-to-background ratio from a Raman scan in z-direction (Figure 4.1b). It would be sufficient to measure at only one location in each phase. Nevertheless, measuring at several positions provides a cross-check that equilibrium has been reached and reduces measurement noise.

To provide automated online premixing of the pure components, the microfluidic setup is extended by a micromixer. This micromixer is a reusable commercially available glass chip (Teardrop Micromixer, Micronit, Netherlands) which guarantees homogeneous mixing at low Reynolds number flow. The push-pull syringe pump used in Chapter 3 is replaced by four programmable syringe pumps (Mid-Pressure Syringe Pump neMESYS, Cetoni GmbH, Germany) for dosing of the liquids: three syringe pumps dose the three pure components of the ternary system at the inlets, one syringe pump pulls the liquid flow at the microchannel outlet. Pulling the liquid flow out reduces the maximum pressure in the microchannel. Since only components with low viscosities were measured in this work, the experiments could also be done only using the inlet syringes. The syringe pumps, micromixer and microchannel are connected by PTFE tubing with an inner diameter of 300 µm and connection parts from PEEK. Syringe filters with a pore diameter of 0.45 µm (MULTOCLEAR PTFE, CS-Chromatographie Service GmbH, Germany) are used at the inlet syringes.

The optical setup (Figure 4.1b) is the same inverse confocal Raman microscope (inVia, Renishaw, UK) that has already been used in the proof of concept in Chapter 3. The beam of a frequency-doubled Nd:YAG-laser (100 mW, 532 nm) is focused by a water-immersion objective (LUMPLFLN 60 XW, NA = 1, Olympus, Japan). The backscattered Raman light is processed in a multichannel analyzer consisting of a spectrometer equipped with a grating with 1800 grooves/mm and a cooled CCD camera.

To further improve the temperature control already used in Chapter 3, the complete

setup including syringe pumps is surrounded by a temperature-controlled box. In addition, the water-flushed aluminum plate already presented in Chapter 3 is placed on top of the microchannel. The temperature of the water-flushed aluminum plate is controlled by a thermostat (CC-K15 Pilot One, Peter Huber Kältemaschinenbau AG, Germany) with external Pt 100 temperature sensor as described in detail in Chapter 3.1. The temperature of the setup is controlled to guarantee a temperature of $T = (298.15 \pm 0.5)$ K during all experiments.

To validate the automated experimental setup, we investigated the two ternary systems cyclohexane - toluene - methanol and *n*-heptane - acetonitrile - ethanol. For both systems, the liquid-liquid flow regime in the used microchannel is strongly laminar and reliable reference data sets are available (Nagata, 1984, 1987). Suppliers, specifications and purities in gas-chromatography area percentage from supplier data (GC, A %) of the used chemicals are listed in Table 4.1.

Table 4.1: Used chemicals with supplier, specification and purity in gas-chromatography area percentage from supplier data (GC, A%).

	supplier	**description**	**purity (GC, A%)**
cyclohexane	VWR	Spectronorm	99.7
toluene	VWR	Spectronorm	99.8
methanol	VWR	Spectronorm	99.9
n-heptane	Bernd Kraft GmbH	For analysis	99.0
acetonitrile	Merck KGaA	For spectroscopy	99.9
ethanol	Merck KGaA	For spectroscopy	99.9

4.3 Data Analysis

The Raman spectra were analyzed using the Indirect Hard Modeling (IHM) approach (Alsmeyer et al., 2004; Beumers et al., 2018). IHM is suitable to quantify systems with strongly overlapping spectral bands and nonlinear mixture effects as it is usually for liquid multicomponent mixtures. In the IHM approach, pure component spectra are modeled by a sum of pseudo-Voigt functions. The models of the pure components are fitted to a mixture spectrum, as it is described in detail in Chapter 3.2. The partial areas A_i of the pure components i in the mixture spectra are proportional to

the corresponding concentrations in the mixture, leading to the following calibration model for the determination of the mole fractions x_i:

$$\frac{A_i}{A_j} = k_{ij}\frac{x_i}{x_j} + b_{ij}, \qquad \text{for } i = 1, ..., n-1 \tag{4.1}$$

$$\sum_{i=1}^{n} x_i = 1. \tag{4.2}$$

In Raman spectra, the partial areas A_i are proportional to the number of molecules of component i. Consequently, k_{ij} is the proportionality factor between the area ratios and mole fraction ratios of two components i and j and the calibration line should start in the origin such that $b_{ij} = 0$. Nevertheless, in some cases, the calibration fit improves by considering small values of $b_{ij} \neq 0$ due to background signals or other elements in the Raman spectra.

Due to the use of the pure component spectra models, IHM requires only few calibration points for accurate results (Alsmeyer et al., 2004). In this work, one calibration model has been set up for each phase of the LLE due to the strongly different concentrations in the two liquid phases of the ternary systems. Herein, the reference component j in each calibration model has been chosen as the component with the highest concentration, hence, the main component of the respective phase. We report relative standard uncertainties $u_r(x_i)$ of the measured mole fractions x_i that are obtained from arithmetic averaging over the bulk phases along the measurement line at observation point s_o (Figure 4.1b).

4.4 Automated Experimental Procedure

An automated workflow has been established to enable the highly efficient and user-independent calibration and LLE determination. In the experimental setup, automation is realized by online sample preparation: the pure components are dosed by independent syringe pumps and premixed in the micromixer. Thus, the complete phase diagram is accessible by adjustment of the ratio of the volume flow rates $\dot{V}_i$ of the pure components i. The mole fractions x_i of the mixture can be calculated from the following equation:

$$x_i = \frac{\dot{n}_i}{\sum_{j=1}^{n} \dot{n}_j}, \qquad \text{for } i = 1, ..., n. \tag{4.3}$$

Since the syringe pumps contain pure components, the molar flow rates $\dot{n}_i$ can be calculated from the volume flow rates $\dot{V}_i$ and the molar volumes of the pure components v_i:

$$\dot{n}_i = \frac{\dot{V}_i}{v_i}, \qquad \text{for } i = 1, ..., n. \tag{4.4}$$

Adjusting the volume flows of the inlet pumps allows one to generate several data points for both calibration (Experiment 1) and LLE data measurement (Experiment 2) in one experiment (Figure 4.2).

4.4.1 Experiment 1: Automated Calibration

To evaluate the unknown mole fractions in the measured LLE from the Raman signal (Experiment 2), Raman spectra have to be calibrated first. In this work, calibration is directly integrated into the automated workflow. Calibration is automated by adjustment of the volume flow rates of the pure components $\dot{V}_i$. During calibration, all components are premixed in the micromixer to guarantee a homogeneous composition within the microchannel (Figure 4.2a). Calibration requires samples of known composition, expressed here by the mole fractions x_i. Consequently, to prepare a calibration sample with desired mole fractions x_i^*, the set values for the volume flow rates $\dot{V}_i$ are determined by

$$\dot{V}_i = \dot{V}_{\text{tot}} \frac{x_i^* \nu_i}{\sum_{j=1}^{n} x_j^* \nu_j}, \qquad \text{for } i = 1, ..., n. \tag{4.5}$$

Here, $\dot{V}_{\text{tot}}$ is the desired total volume flow rate. The actual volume flow rates $\dot{V}_i$ differ slightly since the accuracy of the settings of the syringe pumps is limited and allows only discrete settings. However, the actual values x_i can be calculated from the actual volume flow rates $\dot{V}_i$ and the molar volumes ν_i of the pure components in the syringe pumps according to equations (4.3) and (4.4).

Thus, we use the actual mole fractions x_i for calibration since the only requirement is to know the composition and its actual value is not as important as long as the

desired concentration range is covered. In practice, the difference between desired and actual mole fractions is usually small.

The total volume flow rate was set to $\dot{V}_{\text{tot}}$ =0.03 ml/min for all calibration experiments, which is the maximal volume flow rate to still ensure leak-free performance of the microfluidic setup. Since the individual volume flow rates $\dot{V}_i$ are specified, the total volume flow rate $\dot{V}_{\text{tot}}$ will slightly differ from the set value due to excess volume effects but this difference in flow rate is irrelevant for our measurements: both calibration and LLE measurements measure fluids that are fully mixed or in equilibrium such that the residence time does not impact the results.

At steady-state conditions, Raman spectra are obtained each 10 µm along the measurement line at observation point s_o (Figure 4.1b). Due to the round channel walls and the resulting strong fluctuations in the Raman spectra, the ranges $y < 20$ µm and $y > 380$ µm along the measurement line are not considered. The exposure time was set to 3 seconds per measurement for the system cyclohexane - toluene - methanol and to 5 seconds per measurement for the system *n*-heptane - acetonitrile - ethanol. In the present work, the exposure time was chosen based on preliminary experiments to obtain nearly the same good signal-to-noise ratio in the Raman spectra for both systems. Using the signal-to-noise criterion, the selection of exposure times could also be automatized in the future.

In this work, the automated sample preparation for the integrated calibration is validated by offline measurements using gas chromatography (GC). For this offline validation, the outlet of the microchannel was collected in a syringe. This syringe was installed at the outlet once steady state was reached. Subsequently, the content of the syringe was analyzed offline by GC (HP6890, Hewlett Packard, USA).

4.4.2 Experiment 2: LLE Measurement

In the LLE setup, the complete phase diagram is accessible during one experiment by adjusting the volume flow ratios. This feature had been exploited during calibration and is also used during LLE experiments: Fluid 2 and Fluid 3 are premixed to mixture M1 in the micromixer and contacted with Fluid 1 in the microchannel to reach a desired global mixture M2 (Figure 4.2b and Figure 4.3). The global mixture M2 is inside the miscibility gap of the system. In the same way as for calibration, the volume flow rates $\dot{V}_i$ required to get to the desired global mixture M2 are calculated from the

global mole fractions $x_{i,\mathrm{M2}}$ according to equation (4.5). In order to ensure a priori that the global mixture M2 falls into the miscibility gap, its shape needs to be known. For an unknown system, we estimate the miscibility gap by predictive thermodynamic models like COSMO-RS (Klamt, 2005). For the mixtures used for validation in this work, the miscibility gap was known.

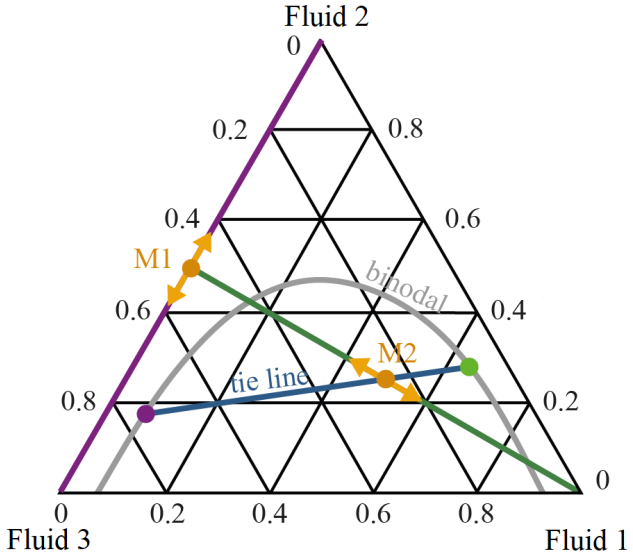

Figure 4.3: Mixing principle for LLE experiments: Fluid 2 and Fluid 3 are premixed to mixture M1 in a micromixer and contacted with Fluid 1 in the microchannel to obtain the global mixture M2 within the miscibility gap.

The minimal retention time to reach equilibrium is determined from repeated measurements using different retention times in an additional experiment (see Chapter 3.3). For the two investigated systems, a retention time at observation point s_o of approximately 3 minutes has proven to be sufficient to reach equilibrium at observation point s_o. This retention time corresponds to a total volume flow rate of $\dot{V}_{\mathrm{tot}} = 0.004$ ml/min which is one order of magnitude smaller than the total volume flow rate of the calibration experiments to ensure that equilibrium is reached.

Different equilibrium points were measured in one experiment by just varying the global composition $x_{i,M2}$. For the determination of the LLE data, the measured equilibrium mole fractions are arithmetically averaged over the equilibrated bulk phase along the measurement line at observation point s_o (Figure 4.4 and Figures A.1 to A.11 in Appendix A). Here again, the ranges $y < 20$ µm and $y > 380$ µm are not taken into account. The phase boundary was also not considered. The phase boundary was

defined as starting and ending when the difference between two measurement points y becomes larger than $\Delta x = 0.002$. As in the calibration experiments, the exposure time was set to 3 seconds per measurement for the system cyclohexane - toluene - methanol and to 5 seconds per measurement for the system n-heptane - acetonitrile - ethanol.

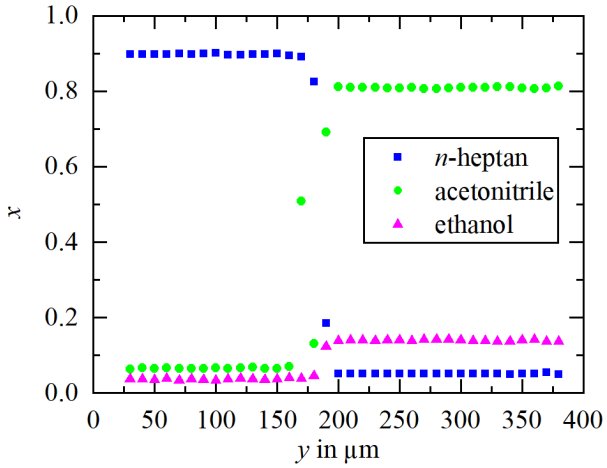

Figure 4.4: Spatially resolved mole fractions in liquid-liquid equilibrium along measurement line at observation point s_o for the system n-heptane - acetonitrile - ethanol (LLE 12).

4.5 Results and Discussion

4.5.1 Automated Calibration

As described above, for each system, all calibration points were measured in one experiment by adjusting the volume flow ratios. The desired mole fractions of all calibration experiments are presented in Tables B.1-B.4 in Appendix B. However, there is a time delay between the adjustment of the volume flow rates $\dot{V}_i$ at the channel inlet and establishing the set composition at observation point s_o, called the start-up period. The length of the start-up period depends on the length of the microchannels and connection parts. Here, the length of this start-up period was estimated from repeated measurements in the middle of the microchannel ($y = 200$ µm) at observation point s_o. After adjustment of new volume flow rates, the new composition was

assumed to be reached when the difference between the mean mole fractions averaged over 100 seconds becomes smaller than $\Delta x = 0.002$. The longest start-up time was about 500 seconds for composition 3 of the system cyclohexane – toluene – methanol (Figure 4.5). To be on the safe side, the start-up period was set to $t = 10$ min for the calibration measurements.

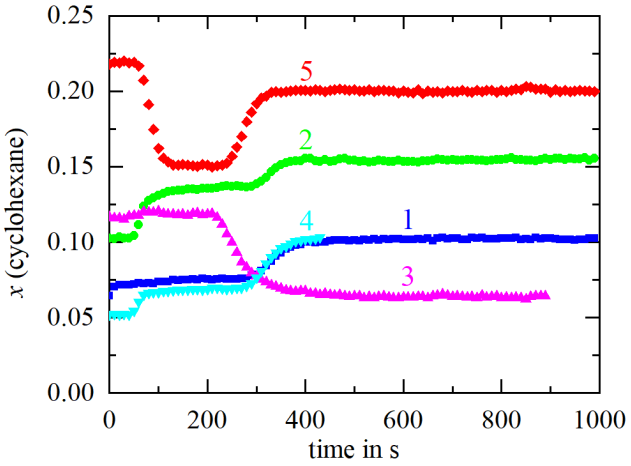

Figure 4.5: Typical composition profiles during start-up of calibration experiments 1-5 chosen to cover a composition range from 5 mol-% to 20 mol-% for cyclohexane. Here, the mole fraction is shown over time for cyclohexane in the system cyclohexane - toluene - methanol. The total volume flow rate is fixed at $\dot{V}_{\mathrm{tot}} = 0.003$ ml/min.

The automated calibration is validated offline by comparison between mole fractions measured by GC and the set concentrations in the calibration experiments (Figure 4.6 and Figures B.1-B.9 in Appendix B). The GC measurements were calibrated separately, leading to independent results. Very good agreement was found between the offline measurements and the set concentrations. Figure 4.6 and Figures B.1-B.9 also show the calibration curves of the concentration measurements by Raman microspectroscopy. The online measured concentrations correspond well to the set concentrations and the offline measured concentrations by GC. Only single experiments show small deviations of the online measurement to the GC measurements (Figure 4.6a and Figure 4.6b). We believe that this deviation is rather due to the offline measurements: the main problem of the offline measurement via GC is the sample collection and, associated therewith, the risk that the concentrations of the most volatile components decrease. The most volatile component of the system cyclohexane - methanol - toluene

is methanol. For the system *n*-heptane - ethanol - acetonitrile, ethanol and *n*-heptane are more volatile than acetonitrile. Overall, methanol is the most volatile component. As result, the offline validation was not possible for small methanol concentrations in the calibration of the cyclohexane-rich phase of the system cyclohexane - methanol - toluene. The offline measured mole fractions of methanol were systematically too low (not shown).

In total, the online and offline measured concentrations agree with the set concentrations within the error bars (Figure 4.6). Consequently, we regard the automated and integrated calibration as successfully validated. The automated and integrated calibration strongly reduced experimental time and effort since manual sample preparation is avoided and only one start-up period is required. With these changes, one calibration experiment sufficient to characterize a ternary mixture needs about two hours experimental time and less than 4 ml of chemicals in total.

4.5.2 Automated LLE Determination

Liquid-liquid equilibria measurements were conducted with the described automated setup for the systems cyclohexane - toluene - methanol (LLE 1-6) and *n*-heptane - acetonitrile - ethanol (LLE 7-12) (Nagata, 1984, 1987). For both systems, six different LLE compositions were successfully determined from a single experiment.

Table 4.2: Experimental liquid-liquid equilibrium mole fractions for the system cyclohexane ($x_1^{'}$,$x_1^{''}$) - toluene ($x_2^{'}$,$x_2^{''}$) - methanol ($x_3^{'}$,$x_3^{''}$) at $T = 298.15 \pm 0.5$ K and $p = 1.013$ bar.

	$x_1^{'}$	$x_2^{'}$	$x_1^{''}$	$x_2^{''}$
LLE 1	0.5971	0.0901	0.2703	0.0538
LLE 2	0.6626	0.0777	0.2552	0.0460
LLE 3	0.6964	0.0666	0.2389	0.0375
LLE 4	0.7224	0.0567	0.2219	0.0285
LLE 5	0.7723	0.0366	0.2039	0.0172
LLE 6	0.8134	0.0212	0.1868	0.0096

Mean relative standard uncertainties u_r are $u_r(x_1^{'}) = 0.0087$, $u_r(x_2^{'}) = 0.0180$, $u_r(x_3^{'}) = 0,0257$, $u_r(x_1^{''}) = 0.0226$, $u_r(x_2^{''}) = 0.0257$ and $u_r(x_3^{''}) = 0.0075$.

For the system cyclohexane - methanol - toluene, the measured mole fractions and

related mean relative uncertainties are presented in Table 4.2. The stated mean relative uncertainties $u_r(x_i)$ in Tables 4.2-4.3 are the mean values of the individual relative uncertainties of each component. Each LLE corresponds to one tie line with end points denoted by ($'$) and ($''$). We obtained average mean relative uncertainties of $\overline{u}_r(x)$=0.0177 for the studied mixture cyclohexane - toluene - methanol.

The system cyclohexane - methanol - toluene has already been measured in Chapter 3. The measurement uncertainties of both data sets are in the same order. Due to the presented automation, we reduced the experimental time in this work by a factor of three while retaining the same level of accuracy.

Table 4.3: Experimental liquid-liquid equilibrium mole fractions for the system n-heptane ($x_1^{'}$,$x_1^{''}$) - acetonitrile ($x_2^{'}$,$x_2^{''}$) - ethanol ($x_3^{'}$,$x_3^{''}$) at $T = 298.15 \pm 0.5$ K and $p = 1.013$ bar.

	$x_1^{'}$	$x_2^{'}$	$x_1^{''}$	$x_2^{''}$
LLE 7	0.6577	0.1219	0.1800	0.3726
LLE 8	0.7584	0.0971	0.1244	0.4754
LLE 9	0.7973	0.0856	0.1042	0.5136
LLE 10	0.8375	0.0772	0.0872	0.5959
LLE 11	0.8736	0.0707	0.0672	0.6984
LLE 12	0.8981	0.0653	0.0510	0.8096

Mean relative standard uncertainties u_r are $u_r(x_1^{'}) = 0.0067$, $u_r(x_2^{'}) = 0.0294$, $u_r(x_3^{'}) = 0.0333$, $u_r(x_1^{''}) = 0.0381$, $u_r(x_2^{''}) = 0.0085$ and $u_r(x_3^{''}) = 0.0093$.

For the system n-heptane - acetonitrile - ethanol, the measured mole fractions and related mean relative uncertainties are presented in Table 4.3. For the mixture n-heptane - acetonitrile - ethanol the average mean relative uncertainty is $\overline{u}_r(x)$=0.0254.

The present setup does not allow to determine the pressure since the system is closed. A known upper bound on pressure is given by the pressure limit of the employed syringes which is 23 bar. However, as the total volume flow rate of the LLE experiments is one order of magnitude smaller than the total volume flow rate of the calibration experiments and the observation point is at the end of the microchannel, the actual pressure is expected to be much lower. Since liquid-liquid equilibria are known to be nearly independent of pressure at low to moderate pressures (Raal and Mühlbauer, 1997), we assume that the measurements represent atmospheric conditions. In future work, we are planning to integrate pressure sensors in the setup.

The measured LLE concentrations were compared to literature data from Nagata (Figure 4.7 and Figure 4.8) (Nagata, 1984, 1987). Considering that Nagata reported an absolute uncertainty of $u(x) = 0.002$ for all mole fraction measurements, the measured concentrations from this work show good agreement with the literature data (Nagata, 1984, 1987). There are only small deviations in the slope of the tie lines of the system *n*-heptane - acetonitrile - ethanol (Figure 4.8).

For our measurements, one LLE experiment was sufficient to determine the complete phase diagram in only about three hours of experimental time and using less than 2 ml of chemicals in total.

The current setup has only been employed at $T = 298.15$ K till now. The component with the lowest temperature limit are the syringe pumps which are limited to $T = 318.15$ K. However, this temperature limit could be overcome by placing the pumps outside the heated box and heating the inlets separately. In general, it is a challenge to guarantee temperature control and optical access for the microscope. The actual temperature limits of the setup will be explored in future work. The pressure limit of the present setup is given by the syringe pumps with 23 bar. In practice, leakage-free operation of the microfluidic chip might also impact the highest possible pressures.

The current setup and analysis relies on the realization of the desired hydrodynamic regime where the two phases are flowing as two laminar layers. For the studied mixtures, we did not encounter any difficulties. However, hydrodynamic issues might occur if the two phases have strongly different properties (e.g., viscosities, densities) or the respective solubilities are such that one phase will be much smaller.

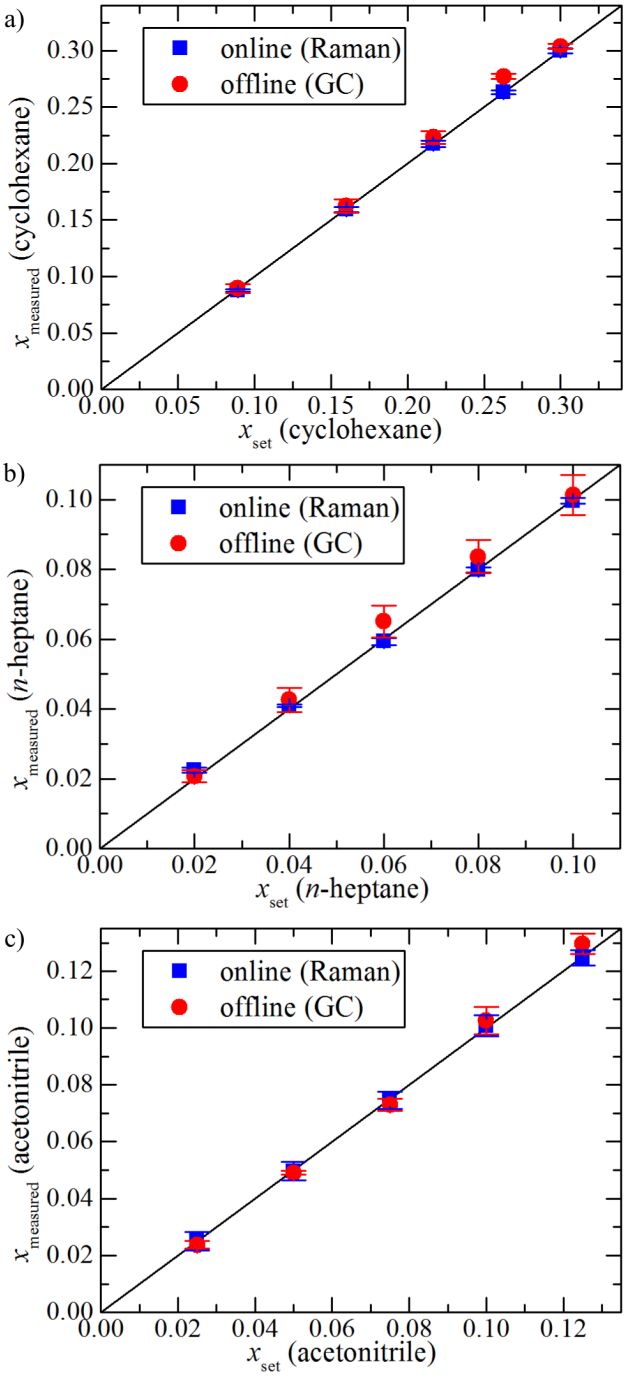

Figure 4.6: Comparison between measured and set concentrations in calibration experiments: (a) Cyclohexane in the methanol-rich area of the system cyclohexane - methanol - toluene. (b) *n*-heptane in the acetonitrile-rich area of the system *n*-heptane - ethanol - acetonitrile. (c) Acetonitrile in the *n*-heptane-rich area of the system *n*-heptane – acetonitrile - ethanol.

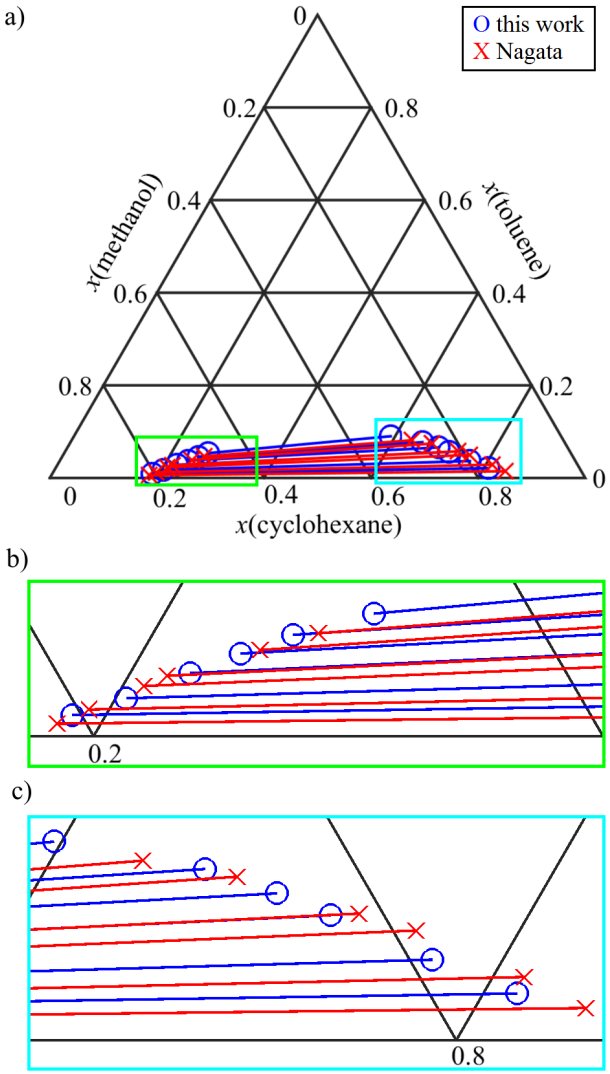

Figure 4.7: Tie-lines of the system cyclohexane - toluene - methanol at $T = 298.15$ K measured in this work and by Nagata (1984): (a) Complete phase diagram. (b) Zoom into methanol-rich phase. (c) Zoom into cyclohexane-rich phase.

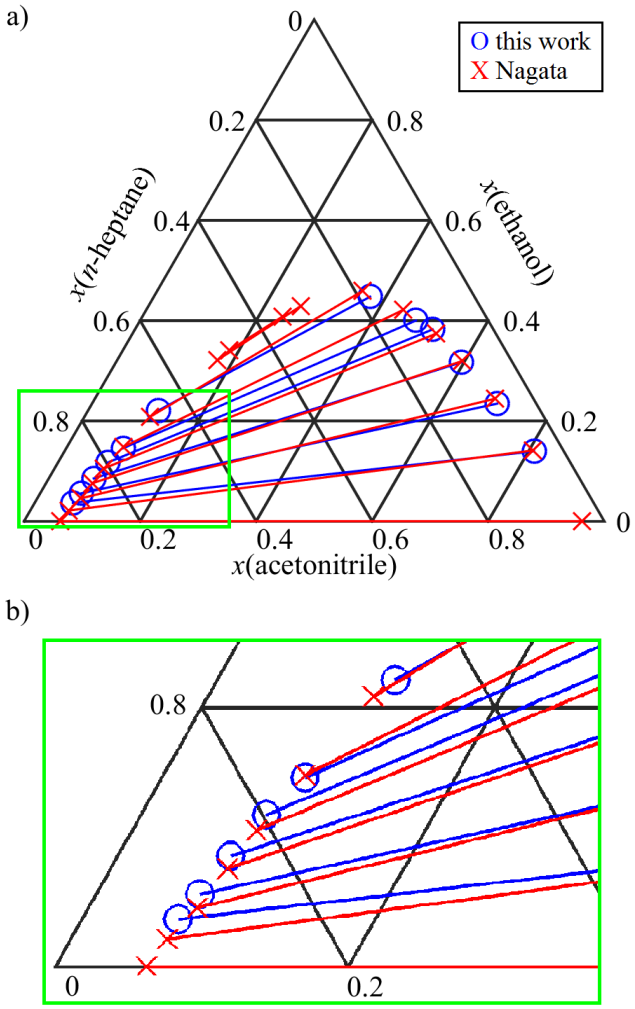

Figure 4.8: Tie-lines of the system *n*-heptane - acetonitrile - ethanol at $T = 298.15$ K measured in this work and by Nagata (1987): (a) Complete phase diagram. (b) Zoom into *n*-heptane-rich phase.

4.6 Conclusions

In this chapter, we demonstrated a new measurement setup and workflow for the automated LLE determination from calibration to data analysis using a combination of microfluidics and Raman microspectroscopy. This combination leads to rapid equilibration, small sample consumption and rapid in-situ concentration determination. In this work, the sample preparation was automated leading to further benefits. Automation was achieved by the integration of a micromixer, the use of flexible syringe pumps and an automated experimental workflow. The automated sample preparation removes the need for manual sample preparation. In addition, data points for both calibration and LLE can be measured in one experiment such that only one start-up period is needed. Consequently, we reduce both sample consumption and experimental effort.

Another benefit of the automated approach should also not be underestimated: The automated approach makes results depend less on the user.

With the automated setup presented in this work, a calibration experiment for a ternary mixture needed only 2 hours and less than 4 ml of chemicals in total. The measurement of six tie lines spanning the complete miscibility gap of a ternary system needed only 3 hours and less than 2 ml of chemicals in total.

In total, an enormous reduction of experimental time and effort could be achieved in comparison to standard analytical methods for LLE determination using the automated platform for LLE measurements.

Chapter 5

LLE using Raman and Single Droplet Tracking in Microfluidic Plug Flow

The microfluidic platform presented in Chapters 3 and 4 contacted two immiscible liquid flows at a small angle at the entry of an H-cell microchannel to form a laminar flow regime. Due to the steady-state flow, phase-specific Raman spectra could easily be acquired at fixed positions along the channel length. However, the laminar flow limits the mass transfer to diffusion only. As a result of the low diffusive mass transfer rates, the equilibrium cannot always be reached within the length of the microchannel, since stable laminar flows are hard to establish in long microchannels, especially for aqueous-organic systems as discussed in Chapter 2.3.1.

Microfluidic plug flows have already been successfully employed to determine distribution coefficients. The concentrations were determined either by using offline standard analytics after phase separation (Susanti et al., 2016; Alimuddin et al., 2008; Kralj et al., 2007; Poulsen et al., 2015) or using in-situ analytics like epifluorescence

M. Kasterke, J. Thien, C. Flake, T. Brands, L. Bahr, A. Bardow, and H.-J. Koß, "Automated Measurement of Liquid-liquid Equilibria using Raman Spectroscopy and Single Droplet Tracking in Microfluidic Plug Flow.", *Fluid Phase Equilibria*, vol. 567, pp. 113718, 2023.

Contribution report: Principal author together with Marvin Kasterke, writing the draft, conceptual design of the setup and the measurement procedure, data evaluation.

microscopy (Marine et al., 2009; Mary et al., 2008) and Raman spectroscopy (Luther et al., 2014; Nelson et al., 2018).

However, to the best of our knowledge, no full LLE measurements have been conducted in microfluidic plug flows until now. The main challenge for using in-situ analytics in combination with plug flows is that mechanisms are needed for phase-selective data acquisition in the moving plugs. This requirement is particularly difficult to satisfy since the phase distribution and, consequently, the plug lengths are not predictable for unknown LLE systems. Taking snapshots of individual moving plugs is possible when using epifluorescence spectroscopy, which allows for high signal intensities. However, only one single fluorescent component can be determined, allowing only determining its concentration and thus the distribution coefficient (Marine et al., 2009; Mary et al., 2008). In contrast, Raman spectroscopy can distinguish between a wide range of molecules, see Section 2.4. Nevertheless, a Raman signal from a single plug crossing a fixed measurement volume is often too weak for a precise quantitative analysis. For this reason, Klima and Braeuer (2019) accumulate the Raman signal from numerous plugs using a photo-electric guard. Their setup thus requires averaging spectra of multiple plugs and does not allow to investigate one single plug.

In addition to the challenge of recording phase-selective spectra, there is also the challenge of quantitatively evaluating these spectra. Since Raman signals of liquid components are strongly overlapping, accurate methods are required for spectra evaluation when small concentrations need to be quantified precisely. Especially, the water signal analysis is quite challenging for low water concentrations in organic phases since the Raman signal of water is very weak and it additionally changes its shape significantly due to disappearing hydrogen bonds (Giraudet et al., 2017).

In this chapter, a setup is presented for full LLE determination based on automated droplet detection and tracking in combination with phase-selective Raman spectroscopy measurements in single plugs of a microfluidic plug flow. A low-cost camera and a traversing unit enable the phase-selective data acquisition of single plugs. The camera detects plugs flowing inside a capillary. Through image processing, the velocities and sizes of the plugs are estimated from the recordings of the camera. Once a stable flow regime is reached, the traversing unit moves the capillary with the plug velocity opposite to the flow direction to keep a single equilibrated plug stationary in the focus of the optical measurement setup. The novel setup is demonstrated for the ternary system acetone - toluene - water and the results are compared

to literature.

5.1 Automated Experimental Setup and Workflow

The experimental setup consists of a syringe pump unit, a micromixer, a capillary which includes a droplet detection unit (DDU) and is installed on a traversing unit, a laser and a spectrometer (Figure 5.1).

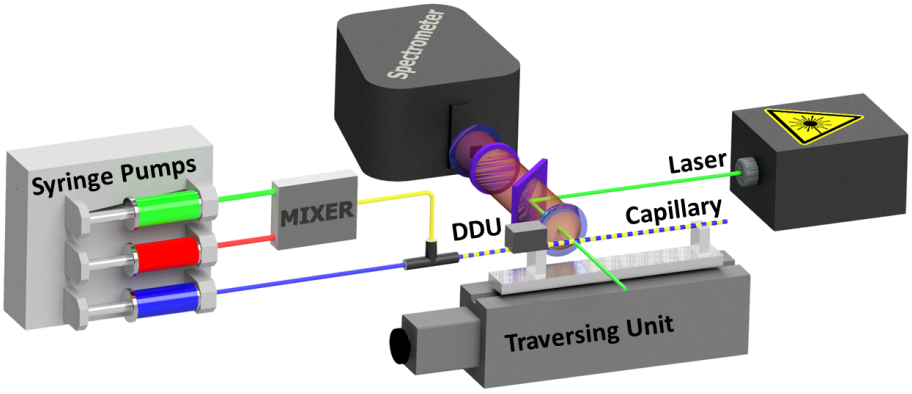

Figure 5.1: Experimental setup with syringe pumps, micromixer, traversing unit, droplet detection unit (DDU), capillary, laser, and spectrometer.

Pure components are dosed via three independent syringe pumps (Mid-Pressure Syringe Pump neMESYS, Cetoni GmbH, Germany). The global concentration can be varied by adjustment of the volume flow ratios so that the time-consuming and error-prone manual sample preparation is omitted, and the complete phase diagram is accessible in a single experiment, see Chapter 4. For the conducted LLE experiments, acetone and toluene are premixed in the micromixer (Swirl Micromixer, Micronit, The Netherlands) and contacted with water in a T-junction (PEEK Tee, CS-Chromatographie Service GmbH, Germany). The T-junction is used for droplet generation at the beginning of the capillary, to form a stable liquid-liquid plug flow (i Solvas and DeMello, 2011). To connect the syringe pumps to the micromixer and capillary, PTFE tubing with an inner diameter of 300 µm and connection parts from PEEK are used. The used capillary is made of fused silica and has an inner diameter of 530 µm and a length of 45 cm. The end of the capillary is open and the liquid flowing out is collected. A traversing unit (isel-automation, Germany) can move the capillary against the flow direction to hold the laser focus in the center of one plug.

The maximum distance that the traversing unit can pass has shown to be 15 cm. Thereby, the biggest challenge is to install the capillary straight enough to keep the focus in the center of the capillary.

Due to the wetting characteristics of the glass capillary, the aqueous phase is the continuous phase, and the organic phase is the dispersed phase in the established plug flow. The plugs of the organic phase are therefore surrounded by a very thin film of the aqueous phase which wets the wall completely. The mass transfer is enhanced due to inner circulations and the resulting homogenous concentrations inside the plugs that keep the concentration gradient high for diffusion across the phase boundary (Assmann et al., 2013).

A droplet detection unit is installed at a distance of 300 mm from the capillary entry (Figure 5.2). A camera (Logitech C270) is directed at the capillary and continuously provides pictures of the plug flow. Four white LEDs next to the camera illuminate the capillary (Figure 5.2a). The complete system is encapsulated so that the light of the LEDs does not impair the Raman measurements. The cameras images are read out and processed by National Instruments LabVIEW 2019 to determine the droplet speeds and lengths. Two brightness control lines are set in the camera image as ranges of interest (ROI) at a fixed distance s to each other in flow direction (Figure 5.2b). These brightness control lines are placed near the glass surface of the capillary since the phases can best be distinguished here due to the different wetting characteristics of the two phases with the glass wall and the resulting shadow between the plugs of the organic phase and the glass surface (Figure 5.2b). The intensity values of the pixels of the two ROI lines were read out continuously and the Labview Script thus detects the change in the light intensity when a Shadow of a phase boundary passes a ROI line. The velocity of the plug flow v is calculated from the time Δt that the plugs need to overcome the distance s. This time delay Δt is calculated from the delay between the edges of the data patterns of ROI 1 and ROI 2 (respectively rising or falling, s. Figure 5.2c).

For the acquisition of the Raman spectra, a confocal setup is used which records the Raman scattered light in backscattering (Figure 5.1). A laser beam of a 532 nm Nd:YAG laser (Genesis CX532-2000 SLM, COHERENT, 150mW) is focused through a lens (N-BK7 Plano-Convex Lens, f=30 mm, A Coated, Thorlabs) onto the sample in the measurement volume inside the capillary. Due to the focusing of the laser, an influence of the small film of the aqueous phase on the spectrum of the organic phase

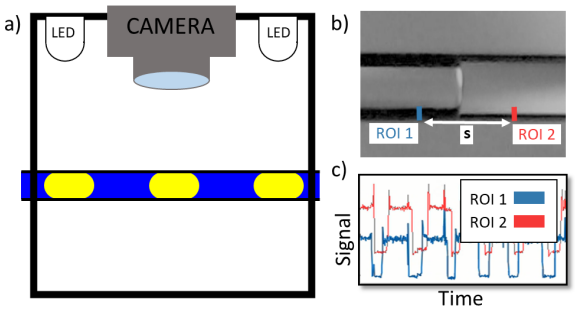

Figure 5.2: Droplet detection unit (DDU): a) Camera captures images of the illuminated capillary. b) Camera image with two defined ranges of interest (ROI) at a fixed distance s to each other. c) Signal over time at ROI 1 and ROI 2.

can be excluded. The backscattered Raman light is separated from the laser light by two dichroic filter (Raman Strahlenteiler RT 532 rdc, AHF Germany, dividing line a 532 nm, 45 °; Semrock 532 nm StopLine single-notch filter, 0 °) and focused on the slit of a spectrometer (IsoPlane SCT320, Princeton Instruments). The spectrally resolved Raman light is recorded by a CCD sensor of a camera (ProEM 1600^4, Princeton Instruments) and saved by the Princeton Instruments Lightfield 5.0 software.

The traversing unit, holding T-Junction and droplet detection unit, is encapsulated from the laboratory environment by a 54.5 x 35 x 30 cm^3 temperature-controlled polystyrene box. This box is omitted for clarity in Figure 5.1. A heat exchange system is installed inside the box to control and ensure temperature stability. A Haake Phoenix II P50C thermostat with an external Pt 100 sensor, combined with a heat exchanger (MagiCool, G2 Slim Radiator 16 FPI – 240 mm), regulates the temperature to $T = 298.15 \pm 0.2$ K. To ensure fast heat transfer and homogeneous temperature distribution, the heat exchanger is ventilated by two 120 mm fans (Arctic P12PWM PST).

A new mixture is analyzed by first recording calibration spectra from weighed-in samples which are injected into the capillary. In this work, for each calibration point, 100 spectra were recorded with an exposure time of 300 ms. The calibration samples must be located in the homogeneous region outside the miscibility gap of the LLE system. Here, for the proof of concept, the location of the miscibility gap is known from literature. For a completely unknown system, the location of the miscibility gap can be estimated by a predictive thermodynamic model like COSMO-RS (Klamt, 2005).

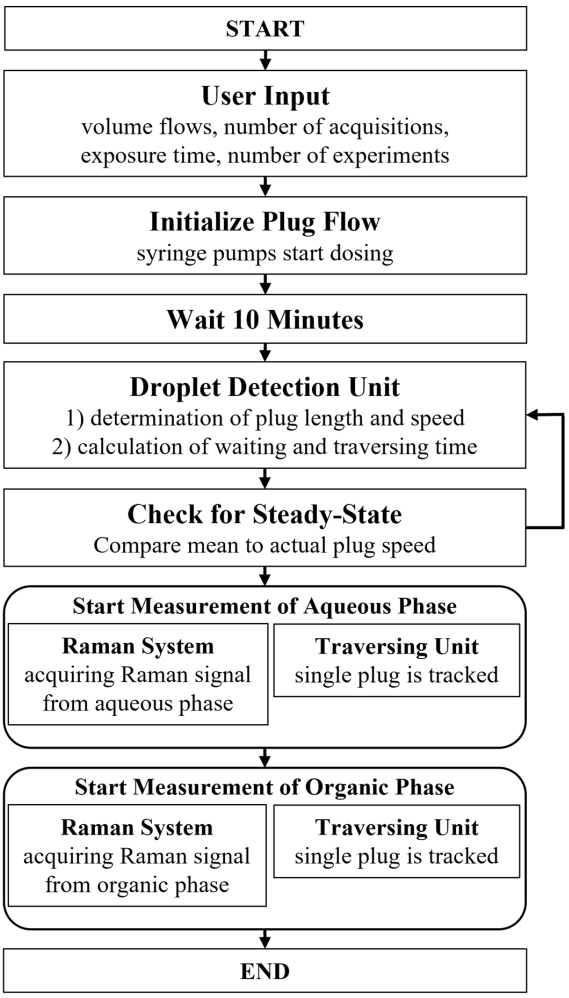

Figure 5.3: Scheme of the automated experimental procedure for liquid-liquid equilibrium measurements.

For the LLE experiments, several global concentrations were chosen inside the miscibility gap. Figure 5.3 shows the scheme of the automated workflow to measure one equilibrium point. To start an experiment, a graphical user interface of the program allows to set the experimental parameters (number of experiments and for each experiment volume flow rates of individual components and number and exposure time of Raman acquisitions). After the initialization of the syringe pumps, the system waits 10 minutes which, in preliminary tests, has proven to be a typical time between the adjustment of the volume flow rates at the syringe pumps and establishing the set composition and a stable plug flow in the capillary. This so-called start-up period depends on the length of the connection parts. After this start-up period, the labVIEW

script automatically determines the droplet lengths and speeds from the camera pictures of the droplet detection unit. For this, the system-specific threshold values for the distinction between the phases are automatically determined from evaluating the intensity values of the ROI-lines over multiple alternating droplets. This procedure is performed separately for each ROI-line because the illumination of the capillary is not homogeneous, and the ROI-lines are located at different positions. The system checks for steady state by calculating the deviation of the measured droplet velocities with the theoretical velocities from the volume balance of the dosing. If this deviation, averaged over the last 10 droplets, is within a range of 1.45 mm/s, steady state is assumed. After reaching the steady state, the system tracks the next passing plug, and the spectrometer starts acquiring spectra with the specified exposure time and number of spectra. Here, 25 spectra with an exposure time of 300 ms are recorded in each plug. At the end of the measurement, the traversing unit returns to the initial starting position and a plug of the other phase can be tracked. Afterwards, the volume flow rates are adjusted to the next global concentration and the automated procedure from Figure 5.3 is repeated.

To validate the setup, the LLE of the ternary system acetone - toluene - water is measured. The measured mole fractions are compared to literature data from Friebel et al. (2017) at $T = 295.15$ K . All chemicals are used as received. Suppliers, specifications, and purities of the used chemicals are listed in Table 5.1.

Table 5.1: Used chemicals with supplier, specification, and purity in gas-chromatography area percentage (GC, A %) from supplier data.

	CAS number	**supplier**	**description**	**purity (GC, A %)**
acetone	67-64-1	VWR	Spectronorm	99.9 %
toluene	108-88-3	VWR	Spectronorm	99.8 %
water	7732-18-5	VWR	Spectronorm	99.9 %

5.1.1 Data Analysis

The Raman spectra are evaluated quantitatively using the Indirect Hard Modeling (IHM) approach (Alsmeyer et al., 2004; Beumers et al., 2018) implemented in the PEAXACT 4 software (S-PACT GmbH, Germany). IHM has proven to be very suitable for quantifying liquid multicomponent mixtures with strongly overlapping

spectral bands (Peters et al., 2020). A detailed description of the method can be found in Chapter 3. The IHM method models pure component spectra by a sum of pseudo-Voigt functions. The resulting pure component models build up a linear mixture model which is fitted to a mixture spectrum, while nonlinear mixture effects as peak shifts are considered by the release of related peak parameters of the pseudo-voigt functions. The fit gives the weights w_i of each pure component i in the mixture spectrum. These weights w_i are, analogous to the partial areas A_i used in Chapters 3 and 4, proportional to the corresponding mole fractions of component i in the mixture so that a linear calibration model can be used for the calculation of the mole fractions x_i:

$$\frac{w_i}{w_j} = k_{ij}\frac{x_i}{x_j}, \qquad \text{for } i = 1, ..., n-1 \tag{5.1}$$

$$\sum_{i=1}^{n} x_i = 1. \tag{5.2}$$

The calibration constants k_{ij} are determined from the known calibration spectra. Here, we chose two different calibration sets according to the expected concentration ranges of the two phases. Water's specific spectral behavior requires these two calibration sets for high accuracy: The shape of liquid water´s Raman spectrum depends on the degree of hydrogen bonding and is thus not constant. With progressing dilution, the hydrogen bonds, whose vibrations make up a large part of the pure component Raman spectrum of water, disappear. Thus, the intensity of the water peak is not proportional to the concentration over the complete concentration range, as it is normally the case for other components. Additionally, the Raman spectrum of diluted water is completely different to the Raman spectrum of pure water (Figure 5.4). Therefore, the pure component spectrum of water can only be used to build the pure component model of water in the aqueous phase. In the organic phase, however, the water concentration is low, and the hydrogen bonds vanish so that a single peak builds the pure component model of water (Figure 5.5) (Kriesten et al., 2008b). The pure component models of acetone and toluene, which are built from the respective pure component spectra, can be used for both calibration sets (Figures C.1 and C.2 in Appendix C).

For the industrially relevant water-organic LLE systems, quantifying water as an analyte is especially challenging at the low concentrations in the organic phase. Compared to organic compounds, water shows a weak Raman cross-section, especially at

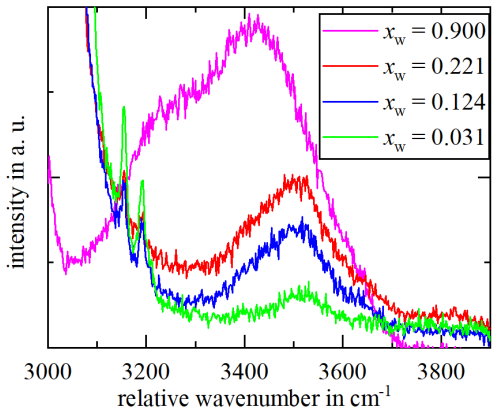

Figure 5.4: OH-stretching vibration band of the Raman spectrum of water changes shape and position with increasing dilution.

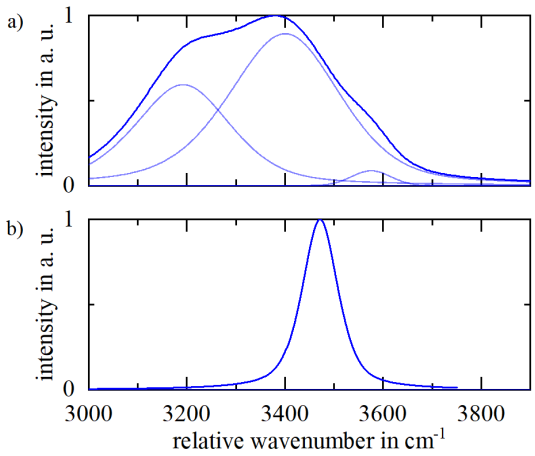

Figure 5.5: IHM pure component models of water: a) IHM model of water in aqueous phase consisting of three peaks. b) IHM model of water in organic phase consisting of one single peak.

lower wavenumbers. To increase the relative area of water in the mixture spectrum, the analysis of the organic phase only employs the part with relative wavenumbers > 2500 cm^{-1} for the spectral evaluation.

The calibration data is presented in Appendix D, including the weighed-in mole fractions and a comparison between measured and set mole fractions for all components in both water-rich and toluene-rich calibration area.

In the LLE experiments, absolute standard uncertainties are obtained from arith-

metic averaging over 25 spectra recorded with an exposure time of 300 ms for each spectrum during single plug tracking. These uncertainties thus represent the measurement variance. The set volume flow rates of the conducted LLE experiments are presented in Table E.1 in Appendix E.

5.2 Results and Discussion

With the introduced automated setup, nine different LLE compositions of the ternary system water - acetone - toluene were successfully determined. For each equilibrium composition, a single plug of either organic or aqueous phase has been tracked and measured successfully. Single droplet tracking provides the additional advantage of checking if the equilibrium is reached. Figure 5.6 and Figures E.1 to E.8 in Appendix E show the development of the mole fractions in one single plug of either aqueous or organic phase during the tracking time of about 10 seconds. All measured mole fractions in all single plugs were constant over time within the measurement uncertainty which finally indicates that the equilibrium has been reached. In this work, the acquisition time of 300 ms per spectrum is sufficient for a good signal-to-noise ratio. With the established workflow, acquisition times up to several seconds from one single plug are possible.

The measured equilibrium mole fractions are arithmetically averaged over all 25 measurements of single plugs. The calculated mean equilibrium mole fractions and the related mean absolute standard uncertainties for all components are presented in Table 5.2.

Figure 5.7 compared our data (given in Table 5.2) and data measured by Friebel et al. (2017) at 295.15 K in a triangular diagram. Friebel et al. (2017) found that there is no significant temperature influence on the LLE for a temperature range of 293.15 K to 303.15 K. Both, the measured equilibrium mole fractions which represent the binodale curve and the slope of the tie lines show excellent agreement within the uncertainties considering that Friebel et al. (2017) indicate a mean standard uncertainty of $\bar{u}(x_i) = 0.008$.

With the presented Raman setup, the measurement of the fully LLE (9 equilibrium concentrations) is possible within about 3 hours, resulting in a sample consumption of less than 3 ml in total.

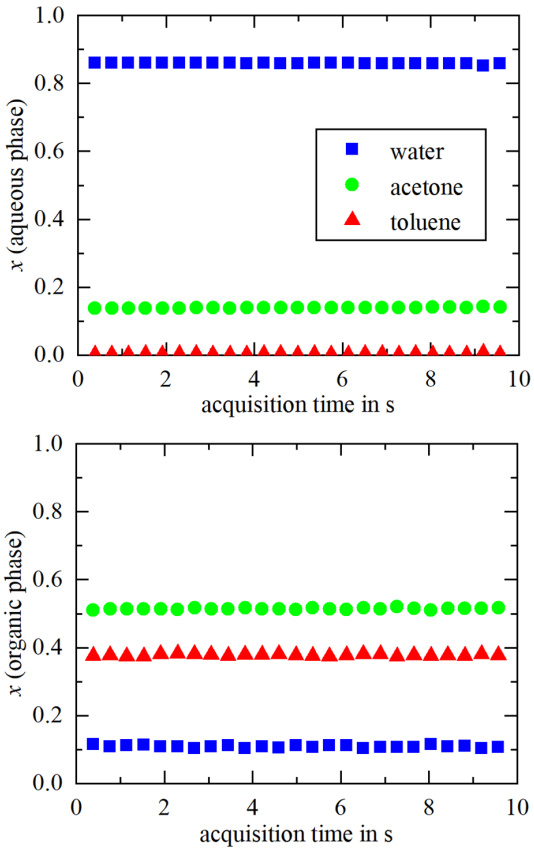

Figure 5.6: Mole fractions in single plugs of organic and aqueous phase over time after start of the first acquisition (LLE 15).

Table 5.2: Liquid-liquid equilibrium mole fractions for the system acetone ($x_1^{'}$,$x_1^{''}$) - toluene ($x_2^{'}$,$x_2^{''}$) - water ($x_3^{'}$,$x_3^{''}$) at $T = 298.15 \pm 0.2$ K and $p = 1.013$ bar.

	$x_1^{'}$	$x_2^{'}$	$x_1^{''}$	$x_2^{''}$
LLE 13	0.5841	0.2066	0.2207	0.0041
LLE 14	0.5498	0.3041	0.1743	0.0028
LLE 15	0.5143	0.3776	0.1391	0.0021
LLE 16	0.4256	0.5064	0.0999	0.0013
LLE 17	0.3588	0.6007	0.0926	0.0010
LLE 18	0.2583	0.7300	0.0661	0.0001
LLE 19	0.2047	0.7875	0.0488	0.0010
LLE 20	0.1510	0.8448	0.0422	0.0015
LLE 21	0.0282	0.9710	0.0108	0.0000

Mean absolute standard uncertainties u are $u(x_1^{'}) = 0.0024$, $u(x_2^{'}) = 0.0035$, $u(x_3^{'}) = 0,0042$, $u(x_1^{''}) = 0.0006$, $u(x_2^{''}) = 0.0006$ and $u(x_3^{''}) = 0.0009$.

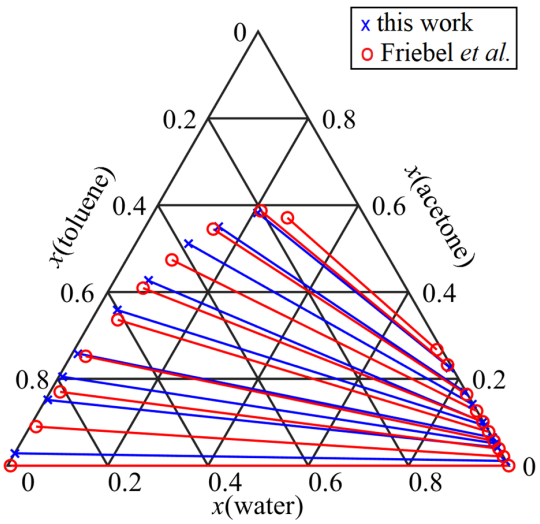

Figure 5.7: Tie-lines of the system acetone - toluene - water measured at $T = 298.15$ K with the presented Raman setup and by Friebel et al. (2017) at $T = 295.15$ K

5.3 Conclusions

This work presents a promising measurement principle for the determination of liquid-liquid equilibria of water-organic systems in microfluidic plug flow. The small capillary dimensions and the inner circulations in the plugs result in fast equilibration of the phases. Using Raman spectroscopy, the precise concentration determination is rapid and in-situ. The automated workflow enables a strong reduction of the experimental effort and omits the error-prone manual sample preparation. For each tie line, an experimental time of 20 minutes is sufficient. The measurement of the complete miscibility gap, here consisting of nine tie lines, needed only about 3 hours and less than 3 ml of chemicals in total.

Time-resolved single droplet tracking offers numerous further possibilities that will be part of future work. For example, the equilibration process or a reaction within a plug can be tracked and quantified. Using this setup to investigate microfluidic plug flows and the setup presented in Chapters 3 and 4 to investigate parallel microfluidic flows, it is now possible to study a wide range of systems with versatile phase properties.

Chapter 6

Summary and Outlook

6.1 Summary

In this work, a new measurement method has been presented which combines Raman spectroscopy, microfluidics and automation for the highly time- and material-efficient determination of experimental liquid-liquid equilibrium data. The presented approach is especially beneficial for the screening of new systems where conventional methods for the determination of LLE data reach their limits since they need large amounts of materials and have large experimental effort (see Section 2.2.1).

Chapter 2 presents the theoretical background and the state of the art of LLE measurements which is needed to understand the importance and application of the new approach presented in this work. In literature, examples for the improvement of the conventional methods can be found which use either automation in combination with standard chromatographic analytics or microfluidics. When using microfluidics, the liquid-liquid flow regime plays an important role for the effectiveness and applicability. Therefore, more insight is given on the different liquid-liquid flow regimes on the microscale. Most of the presented state-of-the-art microfluidic approaches are limited to the determination of distribution coefficients and thus do not provide full LLE data. Here, Raman spectroscopy is very promising to fill the gap since it can be applied in situ and can provide the concentrations of all components simultaneously.

The proof of concept of the feasibility of LLE measurements using Raman spectroscopy in a microfluidic chip is presented in Chapter 3. In the presented setup, a commercially available inverse confocal Raman microscope is used for concentration measurements in a parallel liquid-liquid microfluidic flow regime. The temperature

can be adjusted by a water-flushed aluminum plate on top of the microchannel. An H-cell microchannel is used which has the form of a spiral and thus provides access to multiple observation points which correspond to different retention times of the fluids in the microchannel. Due to the steady-state flow regime, phase-specific Raman spectra can thereby easy be acquired at fixed positions. Spectra are evaluated using the indirect hard modeling approach. For the validation, the LLE of the ternary systems cylohexane - toluene - methanol has been investigated.

In the LLE experiments, pure methanol is contacted with a weighed-in mixture of toluene and cyclohexane with a volume flow ratio of 1:1 and 2.5:1, so that up to two tie-lines can be measured in one experiment by varying the global concentration by the volume flow ratio. Thereby, the volume flow ratio is given by the used syringe pump which provides the same feed velocity for both syringes and which were operated with 1 ml or 2.5 ml syringes. At each observation point, a concentration profile along the channels cross-section perpendicular to the flow direction is measured. In a preliminary test, the mean concentrations of the bulk phases at different retention times were determined and a minimum retention time of 3 minutes has been found to be sufficient to reach the liquid-liquid equilibrium state. To determine the LLE compositions, the measured concentrations are arithmetically averaged over the equilibrated bulk phases at the last observation point. All seven measured equilibrium concentrations show excellent agreement with data from literature. Consequently, the measurement setup has been successfully validated. Using the presented setup, only up to 2 ml sample consumption per experiment and about 3 minutes analysis time per observation point are needed. Thus, the overall time for LLE determination is now mainly dependent on the sample preparation and start-up time.

The reduction of the sample preparation and start-up times is essential to get the highest efficiency concerning time and material consumption since the start-up time is 10 times higher than the time needed for equilibration and measurement. Additionally, the preparation time and quality is mainly user-dependent, which is why manual sample preparation should be completely avoided.

Therefore, the setup presented in Chapter 3 has been improved and automated which in turn is presented in Chapter 4. Additionally, also the calibration, which is another laborious, time-consuming and user-dependent factor, has been integrated in the automated workflow.

Setup and workflow are automated by the integration of a micromixer and the use

of independent syringe pumps which allow for integrated premixing of pure components to any global concentration wanted for either calibration or LLE experiments. By adjustment of the volume flow rates of the pure component-dosing individual syringe pumps, the whole phase diagram is accessible. For the calibration experiments, the global concentration is situated outside the miscibility gap and all pure components are premixed in the micromixer to ensure a homogenous single-phase mixture of known concentration in the microchannel. Afterwards, the connection parts are switched to premix two components for LLE experiments in the micromixer and contact this mixture with the third component in the microchannel. Thereby, the global concentration is situated inside the miscibility gap. Due to diffusional mass transfer across the phase boundary, the concentrations of the two co-flowing immiscible liquid phases are equilibrated until the LLE state is reached.

The temperature control has also been optimized now using a temperature-controlled box which surrounds the complete setup including the syringe pumps in addition to the temperature-controlled plate on top of the microchannel which has been presented in Chapter 3.

Thus, several data points for calibration or the determination of liquid-liquid equilibria can be generated in only one experiment by adjustment of the volume flow rates of the individual syringe pumps. This procedure avoids the highly laborious and error-prone manual sample preparation and makes the results user-independent. Additionally, only one time-consuming start-up period is needed for a complete data set.

The automated setup has been validated successfully with regard to both automated calibration and LLE determination studying the two ternary systems cyclohexane - toluene - methanol and *n*-heptane - acetonitrile - ethanol. The integrated calibration has been validated offline by gas chromatography measurements. With the presented automated setup, only 2 h and less than 4 mL of chemicals for a ternary calibration experiment and only 3 h and less than 2 mL of chemicals for a ternary LLE experiment are needed.

The measurement principle presented in Chapters 3 and 4 is based on a parallel microfluidic liquid-liquid flow regime which limits the mass transfer to diffusion only. This limits the applicability, since for many industrially relevant water-organic biphasic systems, stable laminar flows are hard to establish, especially in long microchannels. These systems tend to form microfluidic plug flows which have the additional

advantage that the mass transfer is enhanced due to convective circulations inside the moving plugs. However, plug flows are alternating so that fixed measurement positions in the microchannel can be problematic since phase-selective spectra acquisition is needed. Using Raman spectroscopy, this is especially challenging, since a single spectrum from a moving plug passing a fixed measurement volume is often to weak for accurate data evaluation. Regarding the quantification of small amounts of water in the organic phase, there is an additional challenge since water is a weak Raman scatterer and the spectrum of water changes its shape depending on the degree of hydrogen bonding.

To overcome these challenges and to be able to measure the LLE of industrially relevant water-organic systems using the highly efficient combination of microfluidics, Raman spectroscopy and automation, a new setup has been set up which is presented in Chapter 5. The setup is based on automated droplet detection and tracking in combination with phase-selective Raman measurements in single plugs of either aqueous or organic phase.

The automated online mixing for the LLE experiments which has been presented in Chapter 4 has also been implemented in the droplet LLE setup presented in Chapter 5. In the droplet LLE setup, two pure compounds are premixed in a micromixer and are contacted with the third component in a T-junction to form a stable liquid-liquid plug flow regime in a round capillary. The capillary is placed on a traversing unit which can move the capillary against the flow direction to hold the laser focus in the center of one plug of either aqueous or organic phase for phase-specific data acquisition. For this, the position, length and the speed of the individual plugs must be known. Therefore, a droplet detection unit has been installed at the beginning of the capillary which provides continuous pictures from the passing droplets from which the droplet positions, lengths and speeds are calculated.

Starting from entering all relevant information in the software (volume flow rates, number of acquisitions, exposure time and number of experiments), the workflow for the LLE measurements is fully automated. After a initialization time of 10 minutes following the start of the syringe pumps, the pictures of the droplet detection unit are continuously evaluated to determine the plug lengths and speeds and to calculate the wait and traversing time. Once a steady-state flow regime is detected from the comparison between the mean to the actual plug speed, the Raman measurement automatically starts. First, one plug of the aqueous phase and then one plug of the

organic phase was held in the laser focus by the movement of the traversing unit while Raman spectra were acquired continuously. The whole procedure is repeated for the next tie line starting from the adaption of the volume flow rates to the new global concentration.

Concerning the evaluation of the Raman spectra, the quantification of water as an analyte of low concentration in the organic phase is especially challenging since water is a weak Raman scatterer compared to organic compounds and the spectrum additionally changes its shape with increasing dilution. In this work, a good evaluation has been achieved by using a reduced spectral range and an adaptet IHM model of water in the organic phase.

With the presented droplet LLE setup, the LLE of the ternary system acetone - toluene - water has been measured successfully and the results are in good agreement with data from literature. In total, the complete LLE has been measured within 3 hours experimental time needing less than 3 ml of chemicals in total.

With the two presented setups, it is now possible to measure LLE data in a very efficient manner using either a parallel or plug microfluidic flow regime, depending on the phase characteristics of the specific system. Consequently, a wide range of systems with versatile phase properties can now be studied.

6.2 Perspective for Future Work

Both presented setups can be used for the efficient generation of LLE data. Although the setups are already very efficient, there is still potential for further improvements concerning the efficiency and application range.

Until now, the temperature control has only been validated for temperatures close to room temperature. However, to generate precise LLE data across a broader temperature range, it is necessary to validate and optimize the temperature control in future research. For this purpose, ternary LLE systems known from literature at several temperatures should be measured as a first step to test the limits of the current temperature control systems of both presented setups (see Chapters 4 and 5). If the resulting valid temperature range does not yet meet the requirements, further improvements must be made.

In addition, the measurement principle should be made accessible to a wide range

of users. Therefore, simple, cheap and secure equipment is desirable. While commercially available capillaries, as discussed in Chapter 5, offer an affordable option, the acquisition of customized glass chips used in Chapters 3 and 4 can be expensive. Here, 3D printing is a promising alternative for the production of cheap and system-adapted microchannels.

In this work, two different Raman setups were used. In Chapters 3 and 4, a commercially available inverse Raman microscope has been used, which is relatively easy and secure to use, but expensive to purchase. For the Raman measurements in the capillary (Chapter 5), laser light is guided using multiple mirrors and lenses and focused in the capillary while the scattered Raman light is collected and guided into a spectrometer. Since the setup can be assembled as desired, it is cheaper and can be built up using standard Raman lab equipment. But the installation and operation needs much more expert knowledge concerning the adjustment and maintenance. Since the optical setup is open and laser light is guided through the room, experiments can only be conducted in an optics laboratory with staff instructed in laser safety. Therefore, the use of fiber optics would be a great step forward to establish the measurement methodology. Using fiber optics, the experiments would be much more robust and would need much less expert knowledge, since the laser light and the scattered Raman light are guided through a flexible optical fiber.

Both presented setups have already been automated, but there are still some manual steps remaining, mostly concerning the start-up of a new experiment and the evaluation of the Raman spectra. It would therefore be desirable to further improve the presented setups and spectral evaluation to come to an holistic fully automated test sequence, beginning from the choice of the flow regime (parallel or plug flow) over calculation of the optimal volume flow rates and execution of all necessary calibration and LLE experiments to the spectral evaluation. Thereby, the previously mentioned predictive methods such as COSMO-RS (Klamt, 2005) could help to predict mixture behaviors which can be used for the choice of the flow regime and for the identification of one-phasic concentrations ranges for calibration. The integration of Optimal Experimental Design methods can help to identify the best LLE experiments (Dechambre et al., 2014b). On the spectral evaluation side, methods for automatic IHM model generation can help to come to the desired fully automated testing sequence (Woehl et al., 2021).

Finally, the two presented setups offer the opportunity to measure further ther-

mophysical property data. Due to the possibility to track a temporal progression, it would be possible to quantify the equilibration process itself or to monitor a reacting system online.

Overall, a promising new measurement principle has been presented in this work, which has shown good performance for the determination of LLE data and which can be adapted to many new fields of application.

Appendix A

Concentration Profiles Along Measurement Line for the Automated LLE Experiments

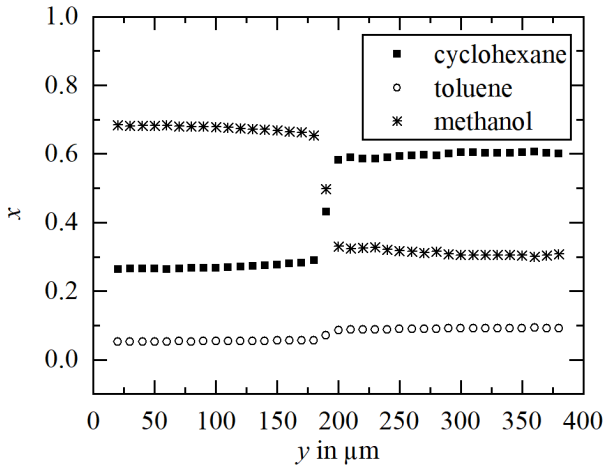

Figure A.1: Spatially resolved mole fractions in liquid-liquid equilibrium along measurement line at observation point s_o for the system cyclohexane - toluene - methanol (LLE 1).

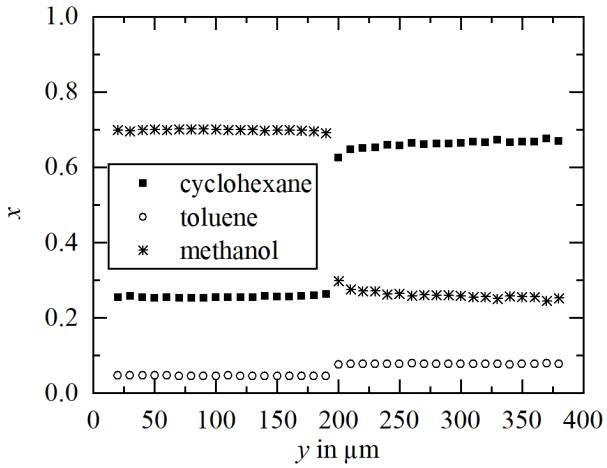

Figure A.2: Spatially resolved mole fractions in liquid-liquid equilibrium along measurement line at observation point s_o for the system cyclohexane - toluene - methanol (LLE 2).

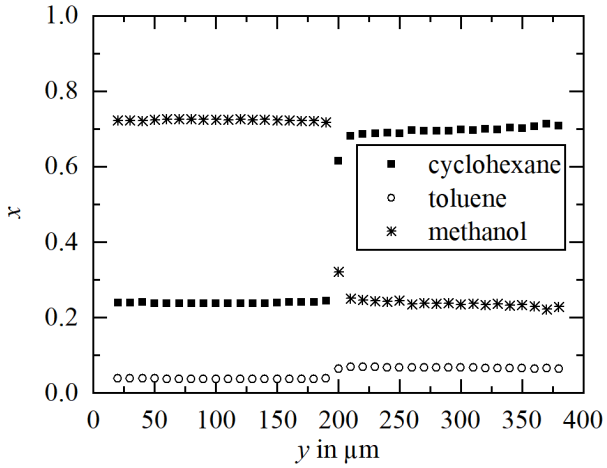

Figure A.3: Spatially resolved mole fractions in liquid-liquid equilibrium along measurement line at observation point s_o for the system cyclohexane - toluene - methanol (LLE 3).

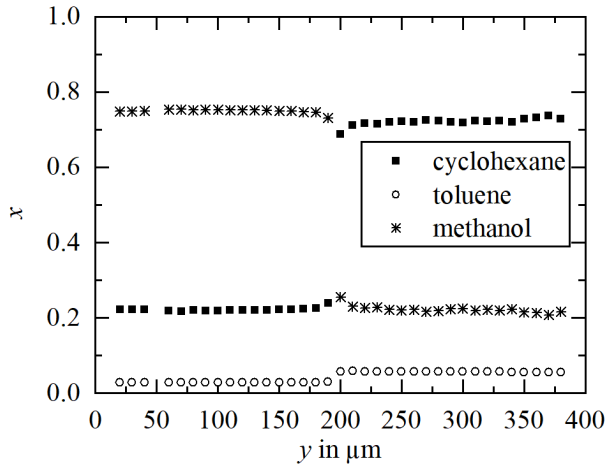

Figure A.4: Spatially resolved mole fractions in liquid-liquid equilibrium along measurement line at observation point s_o for the system cyclohexane - toluene - methanol (LLE 4).

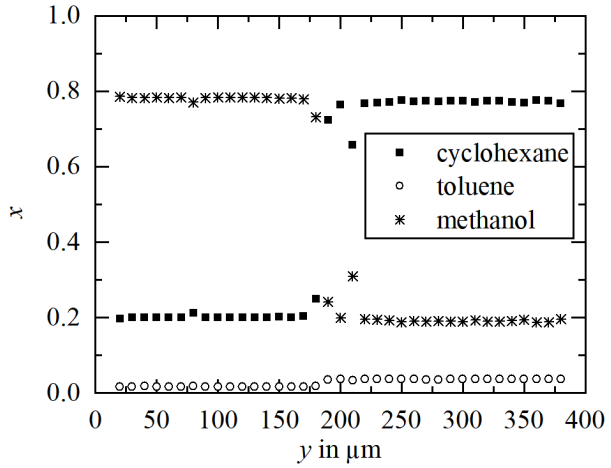

Figure A.5: Spatially resolved mole fractions in liquid-liquid equilibrium along measurement line at observation point s_o for the system cyclohexane - toluene - methanol (LLE 5).

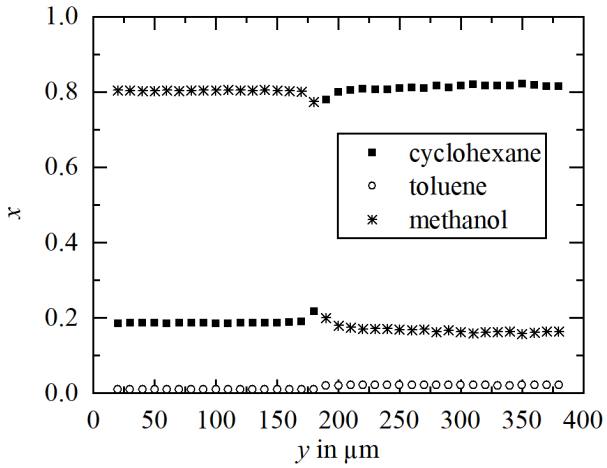

Figure A.6: Spatially resolved mole fractions in liquid-liquid equilibrium along measurement line at observation point s_o for the system cyclohexane - toluene - methanol (LLE 6).

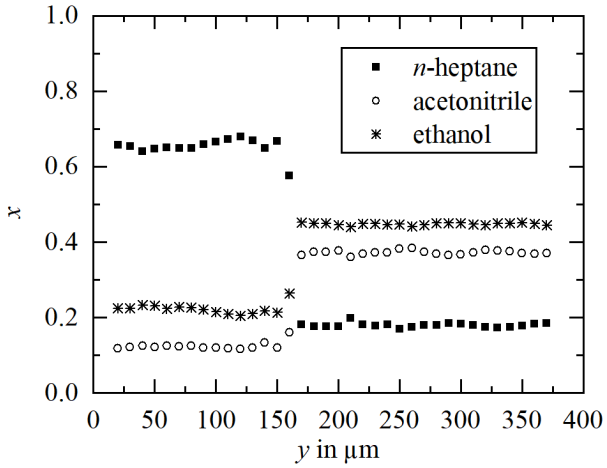

Figure A.7: Spatially resolved mole fractions in liquid-liquid equilibrium along measurement line at observation point s_o for the system n-heptane - acetonitrile - ethanol (LLE 7).

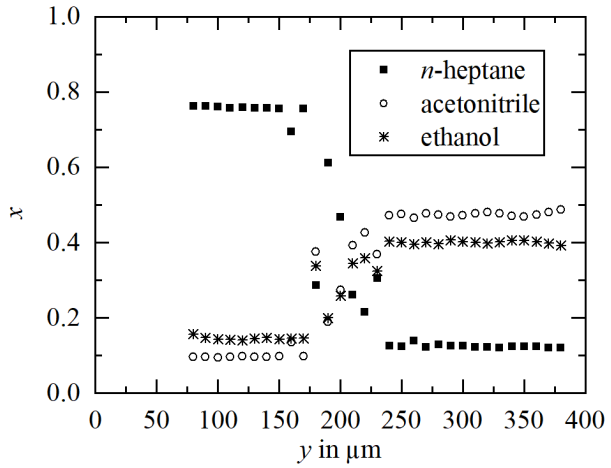

Figure A.8: Spatially resolved mole fractions in liquid-liquid equilibrium along measurement line at observation point s_o for the system n-heptane - acetonitrile - ethanol (LLE 8).

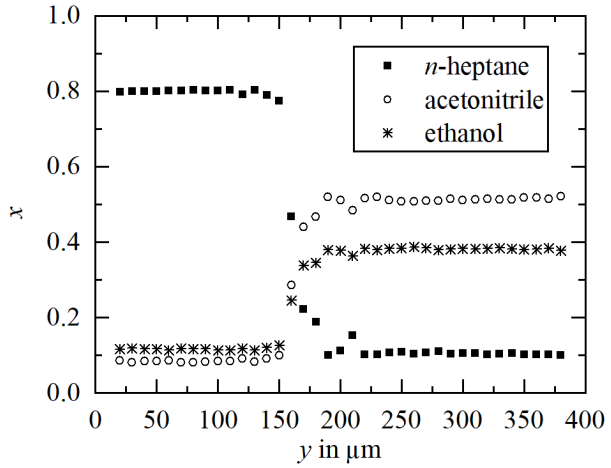

Figure A.9: Spatially resolved mole fractions in liquid-liquid equilibrium along measurement line at observation point s_o for the system n-heptane - acetonitrile - ethanol (LLE 9).

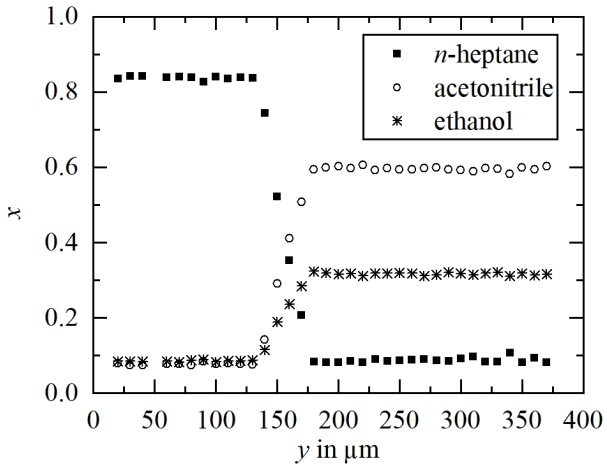

Figure A.10: Spatially resolved mole fractions in liquid-liquid equilibrium along measurement line at observation point s_o for the system n-heptane - acetonitrile - ethanol (LLE 10).

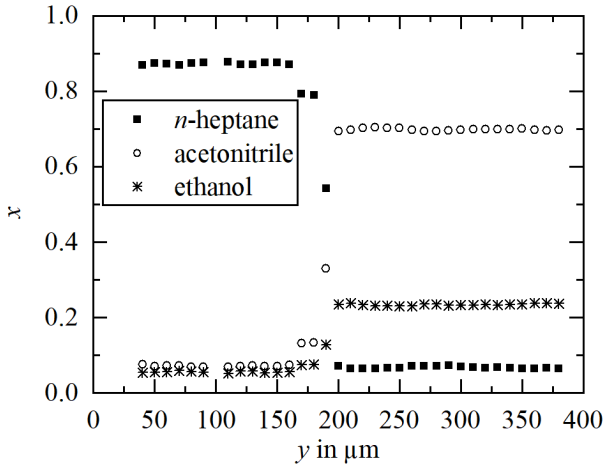

Figure A.11: Spatially resolved mole fractions in liquid-liquid equilibrium along measurement line at observation point s_o for the system n-heptane - acetonitrile - ethanol (LLE 11).

Appendix B

Set Concentrations and Results for Automated Calibration Experiments

Table B.1: Set concentrations in calibration experiments of the *n*-heptane-rich area of the system *n*-heptane (x_1) - acetonitrile (x_2) - ethanol (x_3)

	x_1	x_2
C1	0.8864	0.025
C2	0.7917	0.05
C3	0.7115	0.075
C4	0.6429	0.01
C5	0.5833	0.125

Table B.2: Set concentrations in calibration experiments of the acetonitrile-rich area of the system *n*-heptane (x_1) - acetonitrile (x_2) - ethanol (x_3)

	x_1	x_2
C6	0.02	0.8167
C7	0.04	0.6857
C8	0.06	0.5875
C9	0.08	0.5111
C10	0.1	0.45

Table B.3: Set concentrations in calibration experiments in the methanol-rich area of the system cyclohexane (x_1) - toluene (x_2) - methanol (x_3)

	x_1	x_2
C11	0.0891	0.02
C12	0.16	0.04
C13	0.2169	0.06
C14	0.2629	0.08
C15	0.3	0.1

Table B.4: Set concentrations in calibration experiments in the cyclohexane-rich area of the system cyclohexane (x_1) - toluene (x_2) - methanol (x_3)

	x_1	x_2
C16	0.7083	0.15
C17	0.6923	0.1
C18	0.7107	0.12

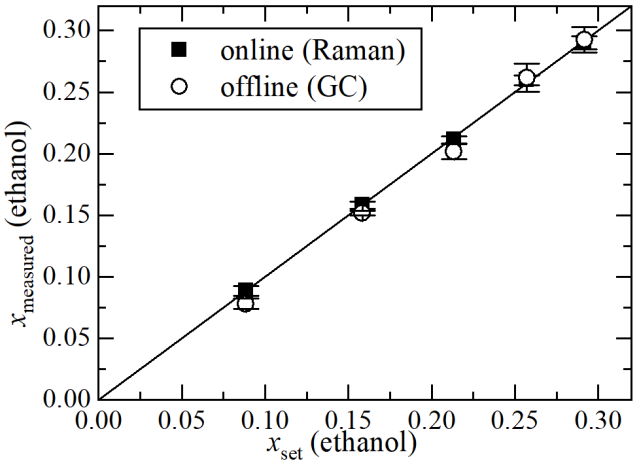

Figure B.1: Comparison between measured and set concentrations in calibration experiments: ethanol in the *n*-heptane-rich area of the system *n*-heptane - acetonitrile - ethanol (C1-C5)

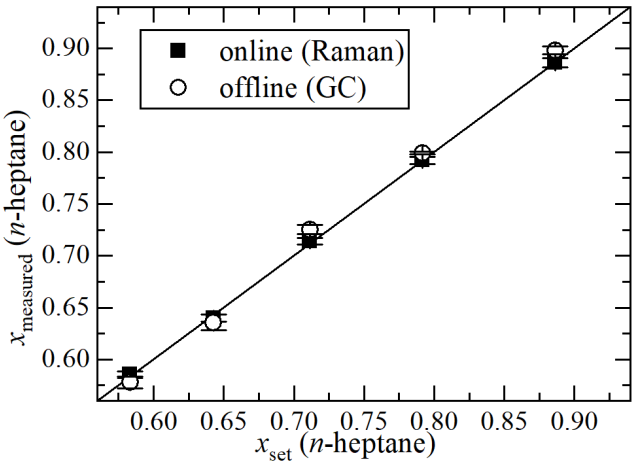

Figure B.2: Comparison between measured and set concentrations in calibration experiments: *n*-heptane in the *n*-heptane-rich area of the system *n*-heptane - acetonitrile - ethanol (C1-C5)

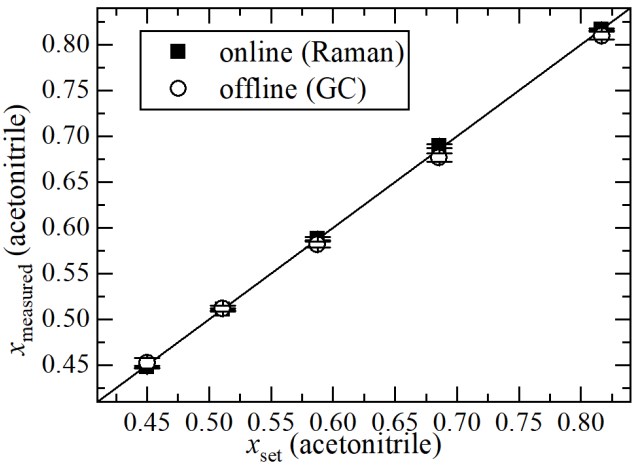

Figure B.3: Comparison between measured and set concentrations in calibration experiments: acetonitrile in the acetonitrile-rich area of the system *n*-heptane - acetonitrile - ethanol (C6-C10)

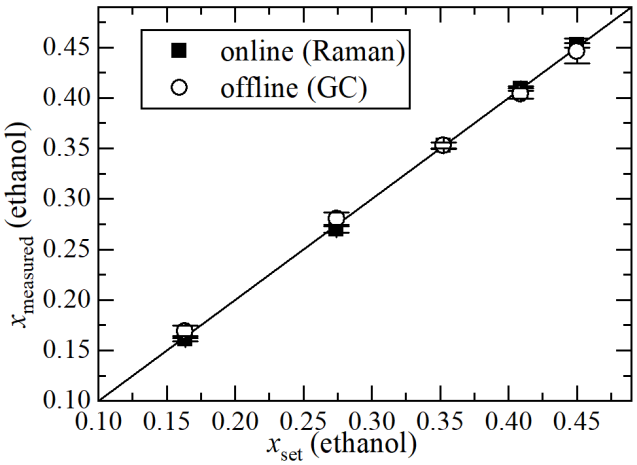

Figure B.4: Comparison between measured and set concentrations in calibration experiments: ethanol in the acetonitrile-rich area of the system *n*-heptane - acetonitrile - ethanol (C6-C10)

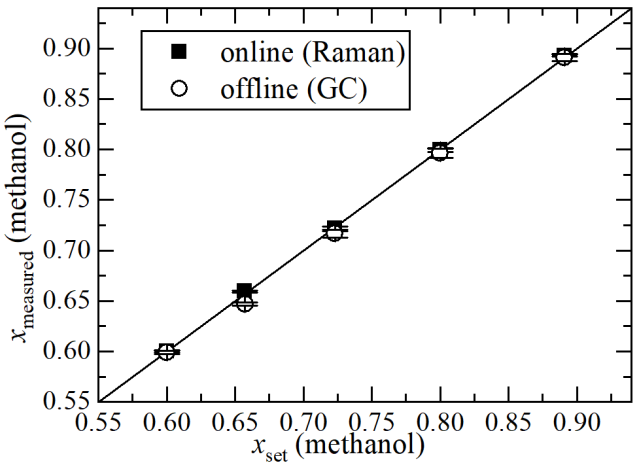

Figure B.5: Comparison between measured and set concentrations in calibration experiments: methanol in the methanol-rich area of the system cyclohexane - toluene - methanol (C11-C15).

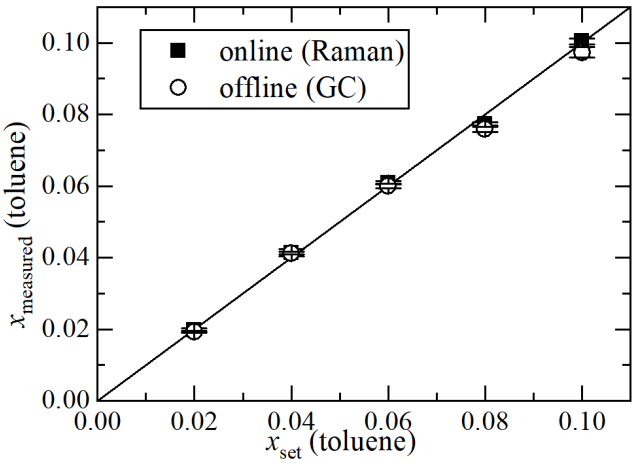

Figure B.6: Comparison between measured and set concentrations in calibration experiments: toluene in the methanol-rich area of the system cyclohexane - toluene - methanol (C11-C15).

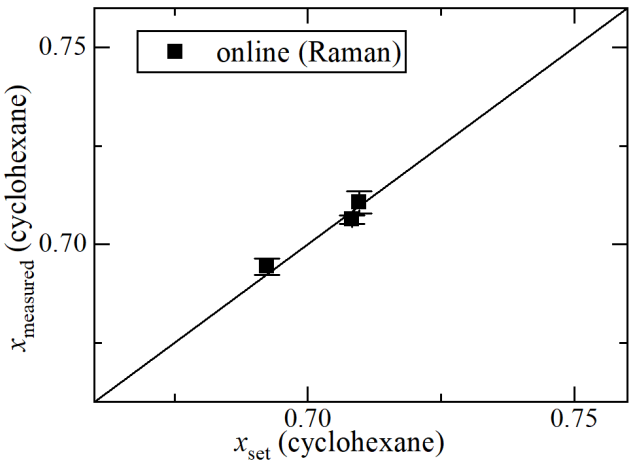

Figure B.7: Comparison between measured and set concentrations in calibration experiments: cyclohexane in the cyclohexane-rich area of the system cyclohexane - toluene - methanol (C16-C18).

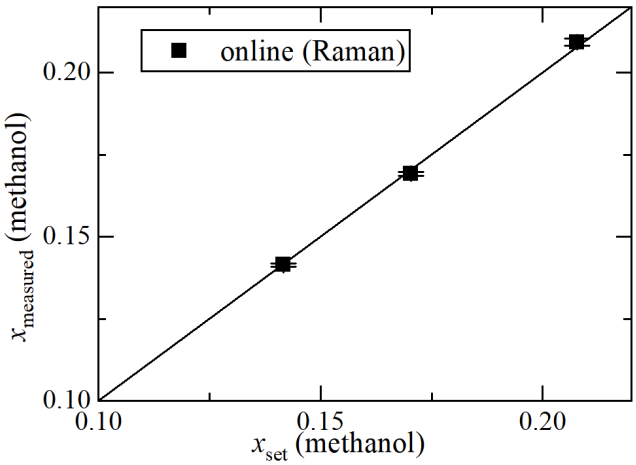

Figure B.8: Comparison between measured and set concentrations in calibration experiments: methanol in the cyclohexane-rich area of the system cyclohexane - toluene - methanol (C16-C18).

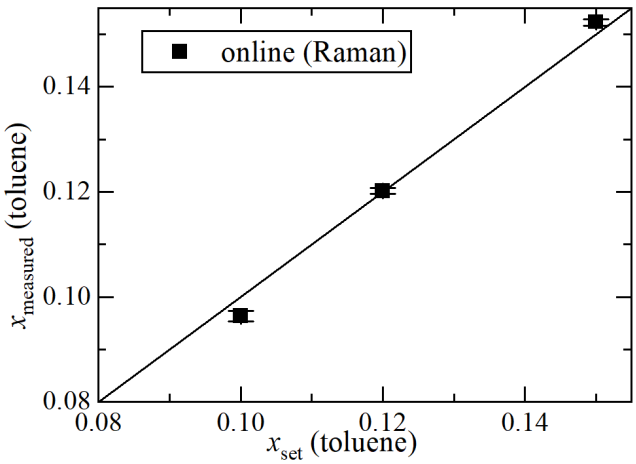

Figure B.9: Comparison between measured and set concentrations in calibration experiments: toluene in the cyclohexane-rich area of the system cyclohexane - toluene - methanol (C16-C18).

Appendix C

IHM Pure Component Models of Acetone and Toluene

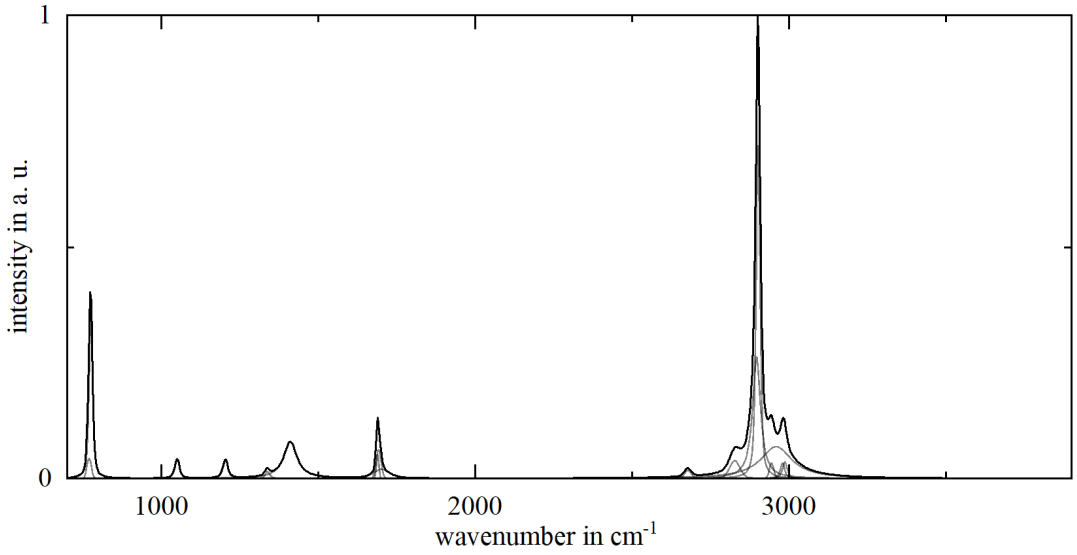

Figure C.1: IHM pure component model of acetone.

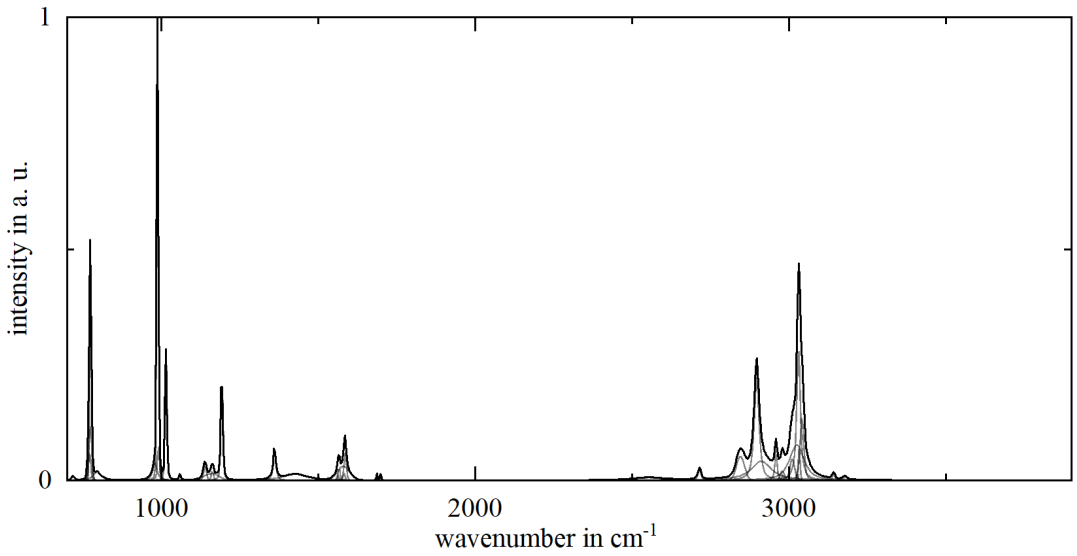

Figure C.2: IHM pure component model of toluene.

Appendix D

Calibration Data for Droplet LLE Experiments

Table D.1: Set mole fractions in calibration experiments of the water-rich area of the system acetone (x_1) - toluene (x_2) - water (x_3)

	x_1	x_2
C19	0.0918	0.0000
C20	0.2816	0.0101
C21	0.3801	0.0099
C22	0.4305	0.0198
C23	0.4821	0.0199

Table D.2: Set mole fractions in calibration experiments of the toluene-rich area of the system acetone (x_1) - toluene (x_2) - water (x_3)

	x_1	x_2
C24	0.1999	0.7956
C25	0.2996	0.6912
C26	0.4011	0.5719
C27	0.5012	0.4501
C28	0.5488	0.3494
C29	0.6003	0.2504
C30	0.6208	0.1805
C31	0.6394	0.1101

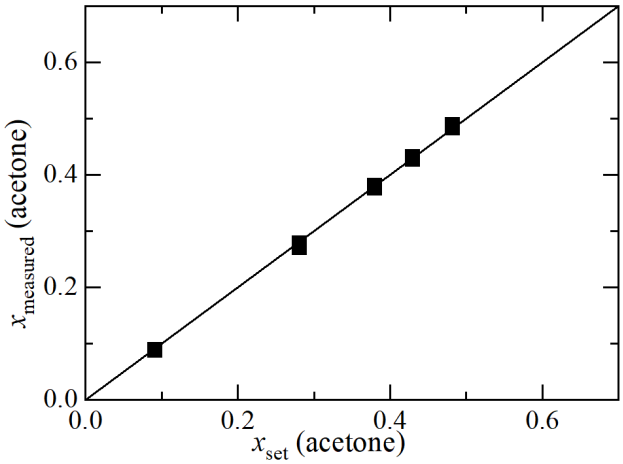

Figure D.1: Comparison between measured and set mole fractions in calibration experiments: acetone in the water-rich area of the system acetone - toluene - water (C19-C23).

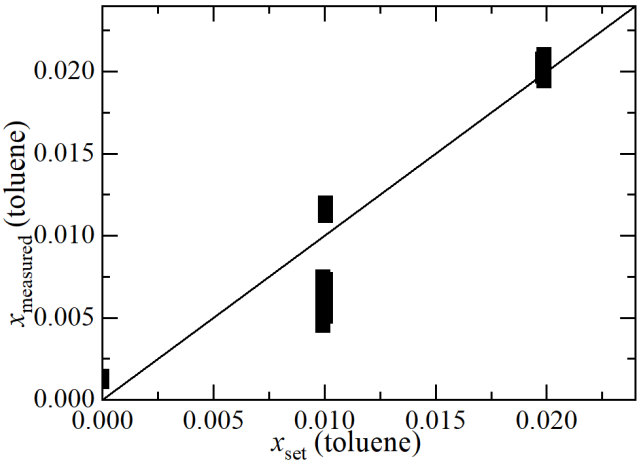

Figure D.2: Comparison between measured and set mole fractions in calibration experiments: toluene in the water-rich area of the system acetone - toluene - water (C19-C23). (Note the small absolute mole fractions in comparision to D.1 and D.3.)

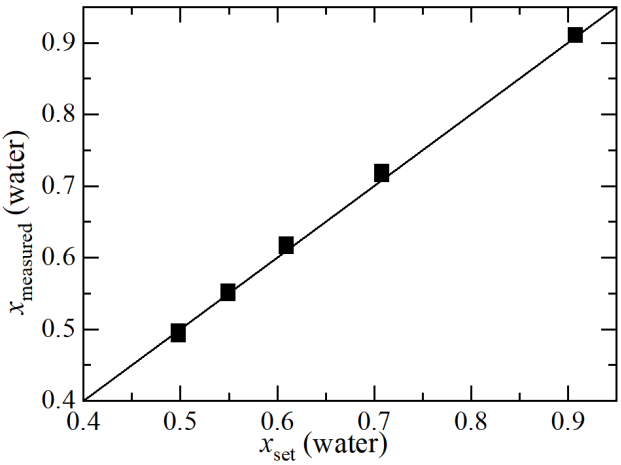

Figure D.3: Comparison between measured and set mole fractions in calibration experiments: water in the water-rich area of the system acetone - toluene - water (C19-C23).

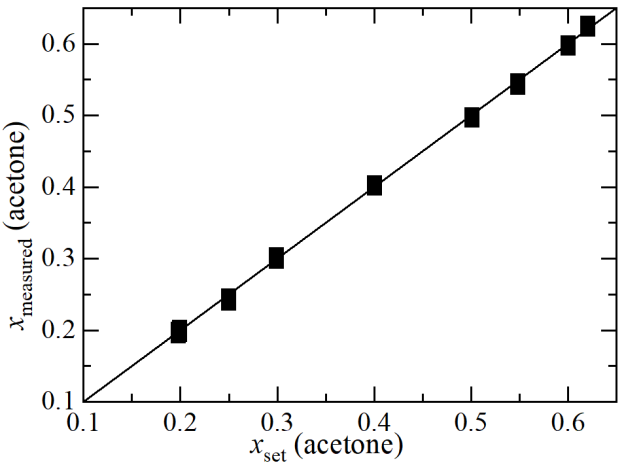

Figure D.4: Comparison between measured and set mole fractions in calibration experiments: acetone in the toluene-rich area of the system acetone - toluene - water (C24-C31).

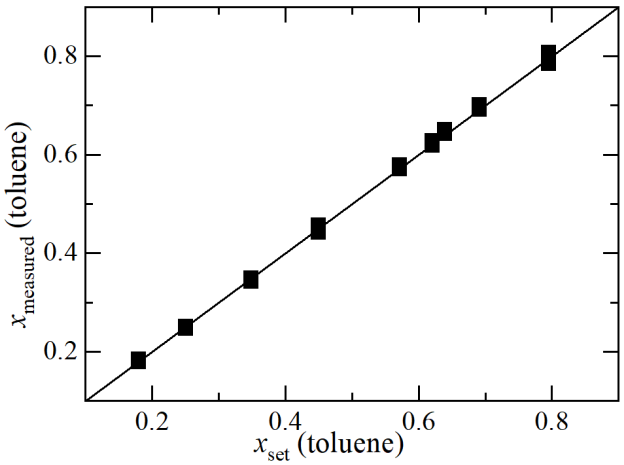

Figure D.5: Comparison between measured and set mole fractions in calibration experiments: toluene in the toluene-rich area of the system acetone - toluene - water (C24-C31).

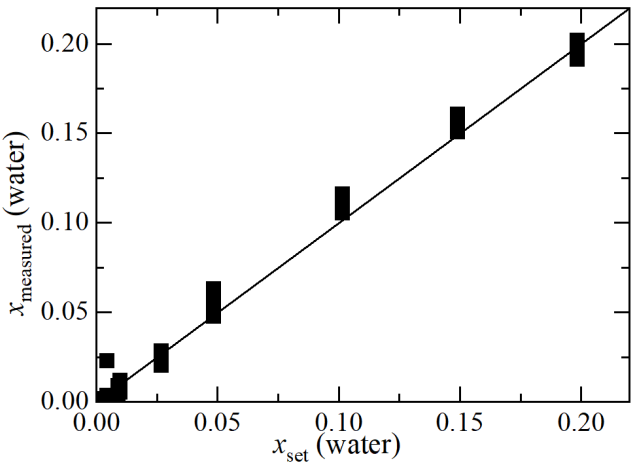

Figure D.6: Comparison between measured and set mole fractions in calibration experiments: water in the toluene-rich area of the system acetone - toluene - water (C24-C31).

Appendix E

Volume Flow Rates and Concentration Lines of Droplet LLE Experiments

Table E.1: Set volume flow rates $\dot{V}_i$ in the LLE experiments of the system acetone ($\dot{V}_1$) - toluene ($\dot{V}_2$) - water ($\dot{V}_3$).

	$\dot{V}_1$ in μL/min	$\dot{V}_2$ in μL/min	$\dot{V}_3$ in μL/min
LLE 13	8.7477	2.7156	3.5366
LLE 14	7.5946	3.6675	3.7379
LLE 15	6.7588	3.9166	4.3246
LLE 16	5.4825	4.964	4.5535
LLE 17	4.4161	5.3313	5.2526
LLE 18	2.9888	6.4948	5.5164
LLE 19	2.407	6.3696	6.2235
LLE 20	1.6158	7.0223	6.362
LLE 21	0.9685	6.2856	7.7459

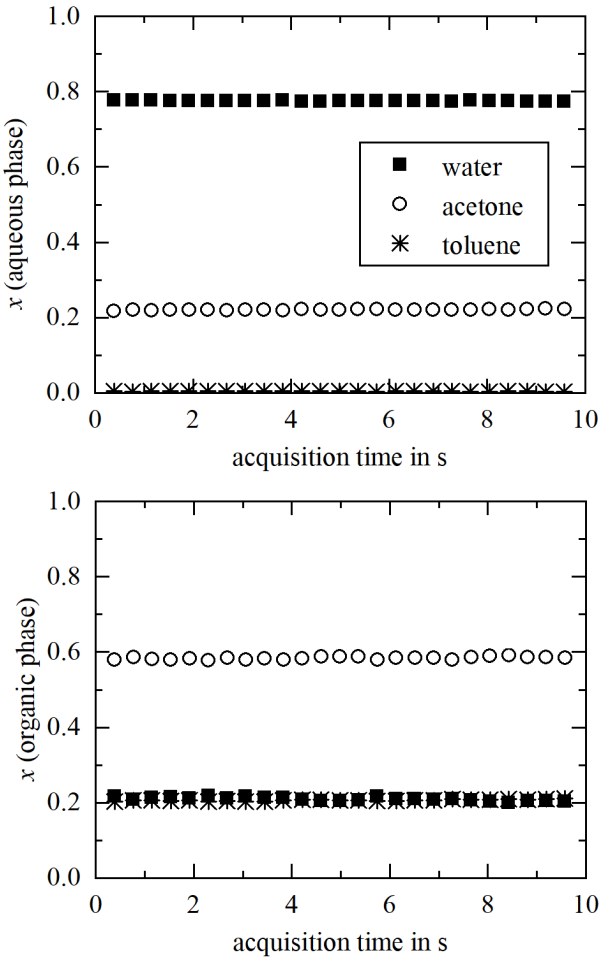

Figure E.1: Mole fractions in a single fragment of organic and aqueous phase over time (LLE 13).

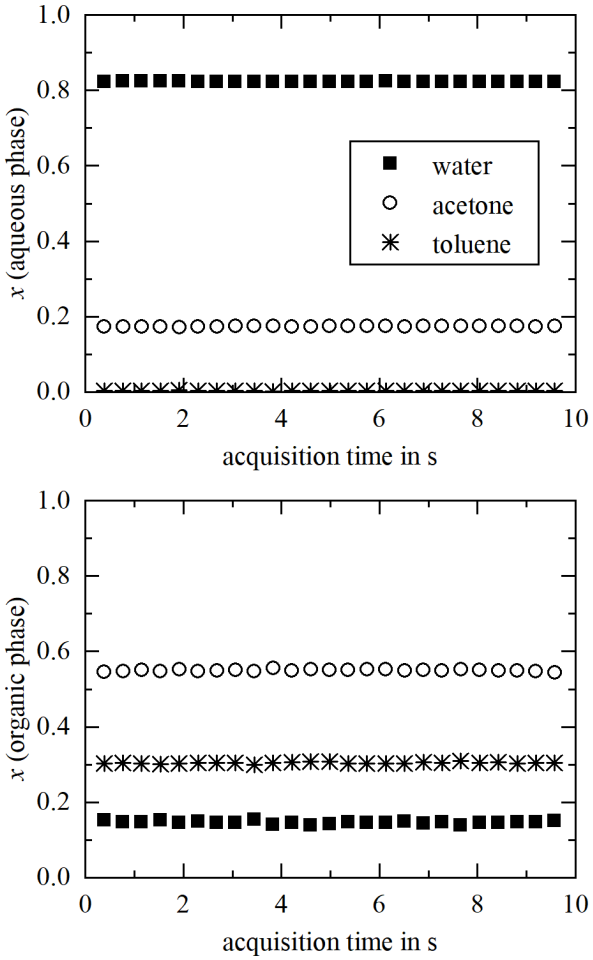

Figure E.2: Mole fractions in a single fragment of organic and aqueous phase over time (LLE 14).

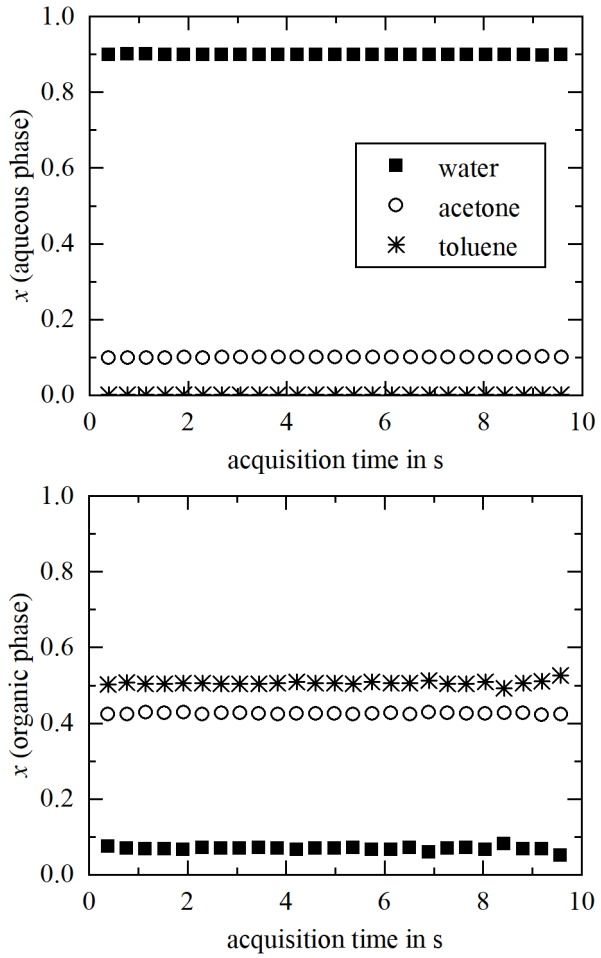

Figure E.3: Mole fractions in a single fragment of organic and aqueous phase over time (LLE 16).

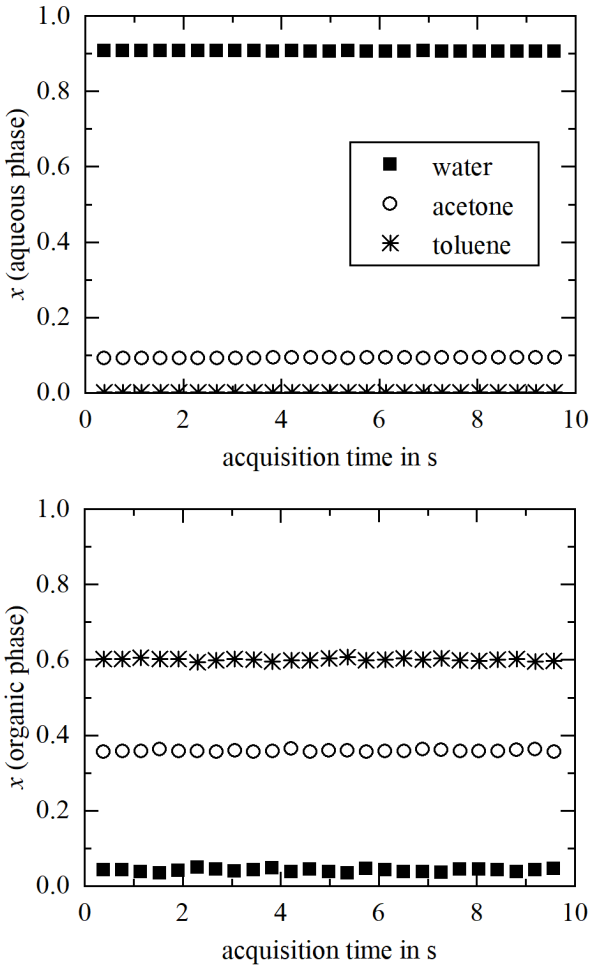

Figure E.4: Mole fractions in a single fragment of organic and aqueous phase over time (LLE 17).

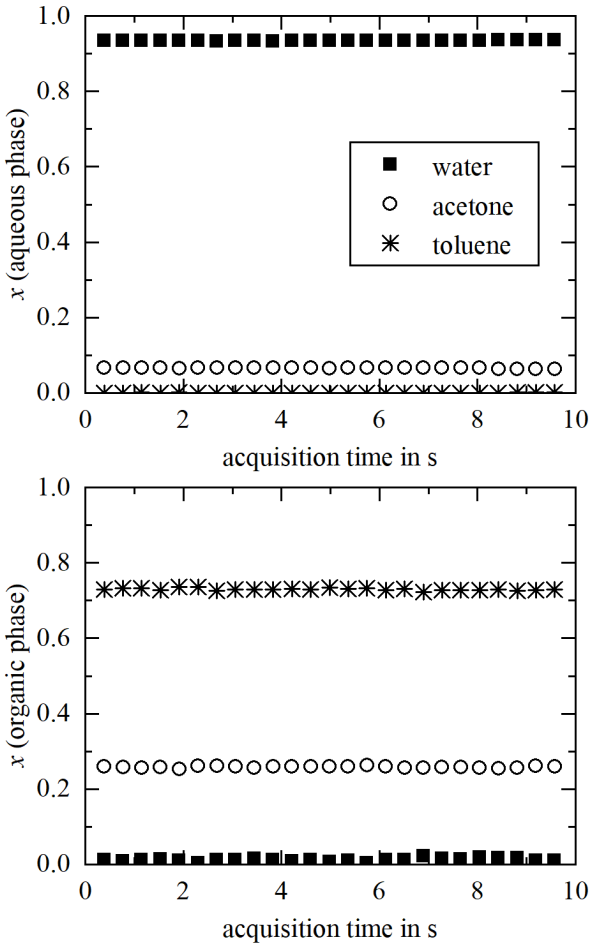

Figure E.5: Mole fractions in a single fragment of organic and aqueous phase over time (LLE 18).

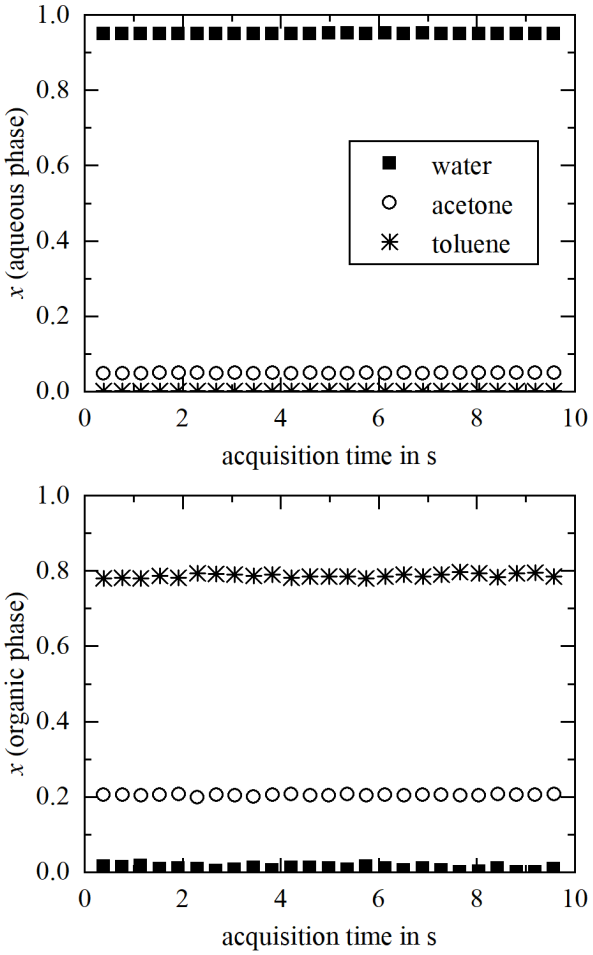

Figure E.6: Mole fractions in a single fragment of organic and aqueous phase over time (LLE 19).

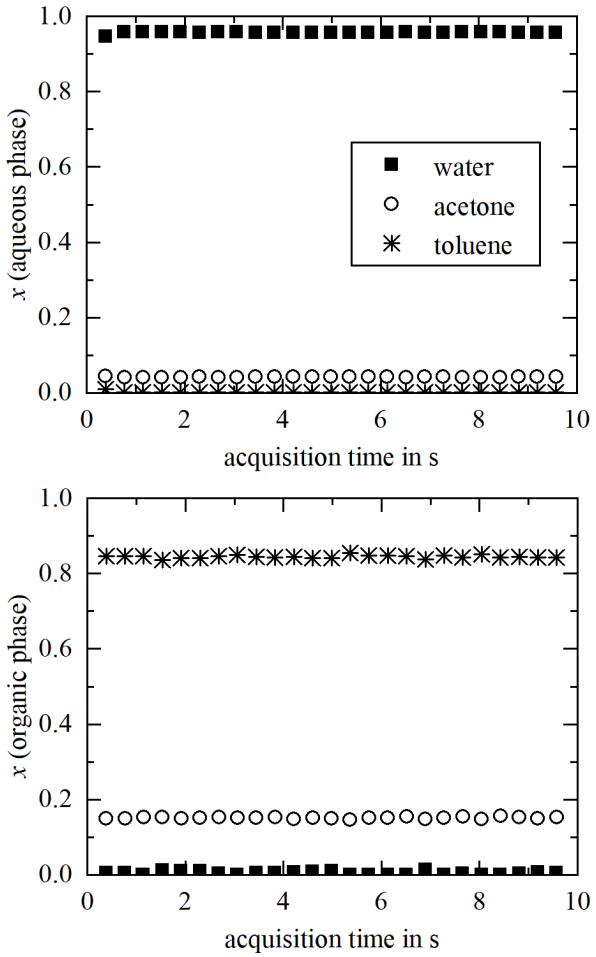

Figure E.7: Mole fractions in a single fragment of organic and aqueous phase over time (LLE 20).

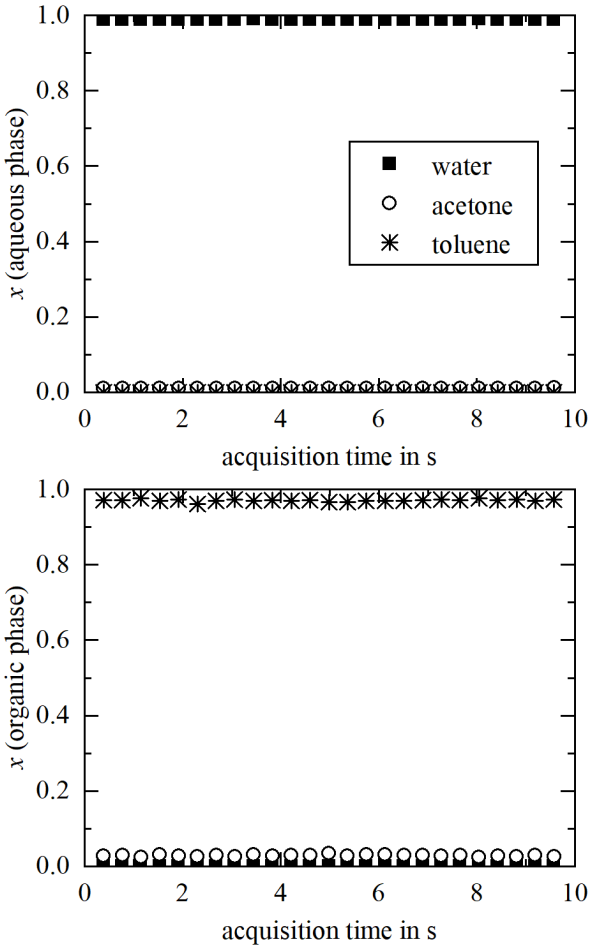

Figure E.8: Mole fractions in a single fragment of organic and aqueous phase over time (LLE 21).

Appendix F

Student Theses Completed within this Work

Berg, J., Gert, G. (2018). Experimentelle Bestimmung von Flüssig-flüssig-Gleichgewichtsdaten für das Kraftstoffgemisch OME, *n*-Heptan und Wasser. Project thesis, RWTH Aachen University.

Eminoglu, Y. (2018). Untersuchungen an mikrofluidischen Propfenströmungen zur Vermessung von Flüssig-flüssig-Gleichgewichten mittels Raman-Mikrospektroskopie. Bachelor thesis, RWTH Aachen University.

Henn, N. (2018). Bestimmung des Einflusses von Natriumchlorid auf das Flüssig-flüssig-Gleichgewicht des Systems Ethanol-Butanol-Wasser mittels Mikrofluidik und Raman-Mikrospektroskopie. Bachelor thesis, RWTH Aachen University.

Kasterke, M. (2018). Simultane Bestimmung von Diffusionskoeffizienten und Verteilungskoeffizienten von Aceton im System Toluol-Wasser mittels Mikrofluidik und Raman-Mikrospektroskopie. Bachelor thesis, RWTH Aachen University.

Kasterke, M. (2020). Konzeption, Aufbau und Inbetriebnahme eines Versuchsaufbaus zur effizienten Messung von Flüssig-flüssig-Gleichgewichten in mikrofluidischen Propfenströmungen mittels Raman-Spektroskopie. Master thesis, RWTH Aachen University.

Münch, G., Laker, J., and Henn, N. (2017). Optimierung eines Versuchsaufbaus zur Messung von Flüssig-flüssig-Gleichgewichten mittels Mikrofluidik und Raman-Mikrospektroskopie durch die Integration eines Mikromischers. Project

thesis, RWTH Aachen University.

Steimann, T. (2018). Quantifizierung von Diffusions- und Verteilungskoeffizienten von Toluol im Stoffsystem Cyclohexan-Toluol-Methanol mittels Mikrofluidik und konfokaler Raman-Mikrospektroskopie. Bachelor thesis, RWTH Aachen University.

Stüwe, L. (2017). Inbetriebnahme und Validierung eines Versuchsaufbaus zur Messung von Flüssig-flüssig-Gleichgewichten mittels 1D-Raman-Spektroskopie. Bachelor thesis, RWTH Aachen University.

Bibliography

Abolhasani, M., Coley, C. W., and Jensen, K. F. (2015). Multiphase Oscillatory Flow Strategy for in Situ Measurement and Screening of Partition Coefficients. *Anal. Chem.*, 87(21):11130–11136.

Adami, R., Schuster, J., Liparoti, S., Reverchon, E., Leipertz, A., and Braeuer, A. (2013). A Raman spectroscopic method for the determination of high pressure vapour liquid equilibria. *Fluid Phase Equilibr.*, 360:265–273.

Alexovič, M., Horstkotte, B., Solich, P., and Sabo, J. (2016). Automation of static and dynamic non-dispersive liquid phase microextraction. Part 1: Approaches based on extractant drop-, plug-, film-and microflow-formation. *Anal. Chim. Acta*, 906:22–40.

Alimuddin, M., Grant, D., Bulloch, D., Lee, N., Peacock, M., and Dahl, R. (2008). Determination of log D via Automated Microfluidic Liquid-Liquid Extraction. *J. Med. Chem.*, 51(16):5140–5142.

Alsmeyer, F., Koß, H.-J., and Marquardt, W. (2004). Indirect Spectral Hard Modeling for the Analysis of Reactive and Interacting Mixtures. *Appl. Spectrosc.*, 58(8):975–985.

Anastas, P. T. and Zimmerman, J. B. (2016). Safer by Design. *Green Chem.*, 18:4324.

Aota, A., Mawatari, K., and Kitamori, T. (2009). Parallel multiphase microflows: fundamental physics, stabilization methods and applications. *Lab Chip*, 9(17):2470–2476.

Assmann, N., Ladosz, A., and Rudolf von Rohr, P. (2013). Continuous Micro Liquid-Liquid Extraction. *Chem. Eng. Technol.*, 36(6):921–936.

Battat, S., Weitz, D. A., and Whitesides, G. M. (2022). An outlook on microfluidics: the promise and the challenge. *Lab Chip*, 22:530–536.

Beumers, P., Brands, T., Koss, H.-J., and Bardow, A. (2016). Model-free calibration of Raman measurements of reactive systems: Application to monoethanolamine/water/CO2. *Fluid Phase Equilibr.*, 424:52–57.

Beumers, P., Engel, D., Brands, T., Koß, H.-J., and Bardow, A. (2018). Robust analysis of spectra with strong background signals by First-Derivative Indirect Hard Modeling (FD-IHM). *Chemometr. Intell. Lab.*, 172:1–9.

Blasco, A. J., Crevillén, A. G., de la Fuente, P., González, M. C., and Escarpa, A. (2007). Electrochemical valveless flow microsystems for ultra fast and accurate analysis of total isoflavones with integrated calibration. *Analyst*, 132(4):323–329.

Blesinger, C., Beumers, P., Buttler, F., Pauls, C., and Bardow, A. (2014). Temperature-Dependent Diffusion Coefficients from 1D Raman Spectroscopy. *J. Solution Chem.*, 43(1):144–157.

Burlage, K., Gerhardy, C., Praefke, H., Liauw, M., and Schomburg, W. (2013). Slug length monitoring in liquid–liquid Taylor-flow integrated in a novel PVDF microchannel. *Chem. Eng. J.*, 227:111–115.

Carlsson, K. and Karlberg, B. (2000). Determination of octanol–water partition coefficients using a micro-volume liquid-liquid flow extraction system. *Anal. Chim. Acta*, 423(1):137–144.

CAS REGISTRY (2023). CAS REGISTRY and CAS Registry Number FAQs (accessed 2023 Sep 14). https://www.cas.org/support/documentation/chemical-substances/faqsy.

Case, F. H., Chaka, A., Moore, J. D., Mountain, R. D., Ross, R. B., Shen, V. K., and Stahlberg, E. A. (2011). The sixth industrial fluid properties simulation challenge. *Fluid Phase Equilibr.*, 310(1-2):1–3.

Chrimes, A. F., Khoshmanesh, K., Stoddart, P. R., Mitchell, A., and Kalantar-zadeh, K. (2013). Microfluidics and Raman microscopy: current applications and future challenges. *Chem. Soc. Rev.*, 42:5880–5906.

Ciceri, D., Perera, J. M., and Stevens, G. W. (2014). The use of microfluidic devices in solvent extraction. *J. Chem. Technol. Biotechnol.*, 89(6):771–786.

DDBST GmbH (2023). List of Systems for Liquid-Liquid Equilibria (Miscibility Gaps) (accessed 2023 Sep 14). http://ddbonline.ddbst.com/DDBSearch/onlinedd boverview.exe?submit=DDBSystems&databank=LLE.

de Koning, S., Janssen, H.-G., and Udo, A. T. B. (2009). Modern methods of sample preparation for GC analysis. *Chromatographia*, 69(1):33–78.

Dechambre, D., Pauls, C., Greiner, L., Leonhard, K., and Bardow, A. (2014a). Towards automated characterisation of liquid–liquid equilibria. *Fluid Phase Equilibr.*, 362:328–334.

Dechambre, D., Thien, J., and Bardow, A. (2017). When 2nd generation biofuel meets water–The water solubility and phase stability issue. *Fuel*, 209:615–623.

Dechambre, D., Wolff, L., Pauls, C., and Bardow, A. (2014b). Optimal Experimental Design for the Characterization of Liquid–Liquid Equilibria. *Ind. Eng. Chem. Res.*, 53(50):19620–19627.

Everall, N. J. (2008). Confocal raman microscopy: Performance, pitfalls, and best practice. In *Pittcon - Invited Lecture at the Symposium "50 Years of SAS: Looking to the Future with Vibrational Spectroscopy"*, New Orleans, Louisiana.

Fabry, D. C., Sugiono, E., and Rueping, M. (2016). Online monitoring and analysis for autonomous continuous flow self-optimizing reactor systems. *React. Chem. Eng.*, 1:129–133.

Frank, T. C., Dahuron, L., Holden, B. S., Prince, W. D., Seibert, A. F., and Wilson, L. C. (2008). *Perry's Chemical Engineers' Handbook*. McGraw-Hill Education.

Friebel, A., Fröscher, A., Münnemann, K., von Harbou, E., and Hasse, H. (2017). In situ measurement of liquid–liquid equilibria by medium field nuclear magnetic resonance. *Fluid Phase Equilibr.*, 438:44–52.

Giraudet, C., Papavasileiou, K. D., Rausch, M. H., Chen, J., Kalantar, A., van der Laan, G. P., Economou, I. G., and Fröba, A. P. (2017). Characterization of Water Solubility in n-Octacosane Using Raman Spectroscopy. *J. Phys. Chem. B*, 121(47):10665–10673.

Glass, M., Aigner, M., Viell, J., Jupke, A., and Mitsos, A. (2017). Liquid-liquid equilibrium of 2-methyltetrahydrofuran/water over wide temperature range: Measurements and rigorous regression. *Fluid Phase Equilibr.*, 433:212–225.

Günther, A. and Jensen, K. F. (2006). Multiphase microfluidics: from flow characteristics to chemical and materials synthesis. *Lab Chip*, 6(12):1487–1503.

Grob, R. L. and Barry, E. F. (2004). *Modern Practice of Gas Chromatography*. John Wiley & Sons.

Heger, S., Bluhm, K., Du, M., Lehmann, G., Anders, N., Dechambre, D., Bardow, A., Schäffer, A., and Hollert, H. (2018). Aquatic toxicity of biofuel candidates on Daphnia magna. *Ecotox. Environ. Safe.*, 164:125–130.

Hibara, A., Fukuyama, M., Chung, M., Priest, C., and Proskurnin, M. A. (2016). Interfacial Phenomena and Fluid Control in Micro/Nanofluidics. *Anal. Sci.*, 32(1):11–21.

Houben, C. and Lapkin, A. A. (2015). Automatic discovery and optimization of chemical processes. *Curr. Opin. Chem. Eng.*, 9:1–7.

Hübner, M. and Minceva, M. (2022). Microfluidics approach for determination of the equilibrium phase composition in multicomponent biphasic liquid systems. *Chem. Eng. Res. Des.*, 184:592–602.

Häusler, E., Domagalski, P., Ottens, M., and Bardow, A. (2012). Microfluidic diffusion measurements: The optimal H-cell. *Chem. Eng. Sci.*, 72:45–50.

i Solvas, X. C. and DeMello, A. (2011). Droplet microfluidics: recent developments and future applications. *Chem. Commun.*, 47(7):1936–1942.

Jovanovic, J., Rebrov, E. V., Nijhuis, T., Kreutzer, M., Hessel, V., and Schouten, J. C. (2011). Liquid–Liquid Flow in a Capillary Microreactor: Hydrodynamic Flow Patterns and Extraction Performance. *Ind. Eng. Chem. Res.*, 51(2):1015–1026.

Kaiser, T., Voßmerbäumer, C., and Schweiger, G. (1992). A New Approach to the Determination of Fluid Phase Equilibria: Concentration Measurements by Raman Spectroscopy. *Ber. Bunsenges. Phys. Chem.*, 96(8):976–980.

Kashid, M. N., Gerlach, I., Goetz, S., Franzke, J., Acker, J. F., Platte, F., Agar, D. W., and Turek, S. (2005). Internal Circulation within the Liquid Slugs of a Liquid–Liquid Slug-Flow Capillary Microreactor. *Ind. Eng. Chem. Res.*, 44(14):5003–5010.

Kashid, M. N., Renken, A., and Kiwi-Minsker, L. (2011). Gas–liquid and liquid–liquid mass transfer in microstructured reactors. *Chem. Eng. Sci.*, 66(17):3876–3897.

Kim, H.-B., Ueno, K., Chiba, M., Kogi, O., and Kitamura, N. (2000). Spatially-Resolved Fluorescence Spectroscopic Study on Liquid/Liquid Extraction Processes in Polymer Microchannels. *Anal. Sci.*, 16(8):871–876.

Kitt, J. P. and Harris, J. M. (2015). Confocal Raman Microscopy for in Situ Measurement of Octanol–Water Partitioning within the Pores of Individual C18-Functionalized Chromatographic Particles. *Anal. Chem.*, 87(10):5340–5347.

Klamt, A. (2005). *COSMO-RS: from quantum chemistry to fluid phase thermodynamics and drug design*. Elsevier.

Klima, T. C. and Braeuer, A. S. (2019). Vapor-liquid-equilibria of fuel-nitrogen systems at engine-like conditions measured with Raman spectroscopy in micro capillaries. *Fuel*, 238:312–319.

Kontogeorgis, G. M., Dohrn, R., Economou, I. G., de Hemptinne, J.-C., ten Kate, A., Kuitunen, S., Mooijer, M., Zilnik, L. F., and Vesovic, V. (2021). Industrial Requirements for Thermodynamic and Transport Properties: 2020. *Ind. Eng. Chem. Res.*, 60(13):4987–5013.

Kralj, J. G., Sahoo, H. R., and Jensen, K. F. (2007). Integrated continuous microfluidic liquid–liquid extraction. *Lab Chip*, 7:256–263.

Kriesten, E., Alsmeyer, F., Bardow, A., and Marquardt, W. (2008a). Fully automated indirect hard modeling of mixture spectra. *Chemometr. Intell. Lab.*, 91(2):181–193.

Kriesten, E., Mayer, D., Alsmeyer, F., Minnich, C. B., Greiner, L., and Marquardt, W. (2008b). Identification of unknown pure component spectra by indirect hard modeling. *Chemometr. Intell. Lab.*, 93:108–119.

Kuzmanović, B., van Delden, M. L., Kuipers, N. J. M., and de Haan, A. B. (2003). Fully Automated Workstation for Liquid-Liquid Equilibrium Measurements. *J. Chem. Eng. Data*, 48(5):1237–1244.

Liebergesell, B., Flake, C., Brands, T., Koß, H.-J., and Bardow, A. (2017). A milliliter-scale setup for the efficient characterization of isothermal vapor-liquid equilibria using Raman spectroscopy. *Fluid Phase Equilibr.*, 446:36–45.

Liu, Y. and Jiang, X. (2017). Why microfluidics? Merits and trends in chemical synthesis. *Lab Chip*, 17:3960–3978.

Luther, S. K., Schuster, J. J., Leipertz, A., and Braeuer, A. (2013). Non-invasive quantification of phase equilibria of ternary mixtures composed of carbon dioxide, organic solvent and water. *J. Supercrit. Fluids*, 84:146–154.

Luther, S. K., Stehle, S., Weihs, K., Will, S., and Braeuer, A. (2015). Determination of Vapor-Liquid Equilibrium Data in Microfluidic Segmented Flows at Elevated Pressures using Raman Spectroscopy. *Anal. Chem.*, 87:8165–8172.

Luther, S. K., Will, S., and Braeuer, A. (2014). Phase-specific Raman spectroscopy for fast segmented microfluidic flows. *Lab Chip*, 14(16):2910–2913.

Marine, N. A., Klein, S. A., and Posner, J. D. (2009). Partition Coefficient Measurements in Picoliter Drops Using a Segmented Flow Microfluidic Device. *Analytical Chemistry*, 81(4):1471–1476.

Mary, P., Studer, V., and Tabeling, P. (2008). Microfluidic Droplet-Based Liquid–Liquid Extraction. *Anal. Chem.*, 80:2680–2687.

Nagata, I. (1984). Liquid-liquid equilibria for four ternary systems containing methanol and cyclohexane. *Fluid Phase Equilibr.*, 18:83–92.

Nagata, I. (1987). Liquid-liquid equilibria for ternary acetonitrile-ethanol-saturated hydrocarbon and acetonitrile-l-propanol-saturated hydrocarbon mixtures. *Thermochim. Acta*, 119:357–368.

Nakayama, H., Murai, M., Tono-oka, M., Masuda, K., and Ishii, K. (2007). Enhancement of Structural Fluctuation in the Region Connecting Two Kinds of Critical Points in Temperature–Pressure–Composition Three-Dimensional Phase Diagram: Raman Studies of Benzene/CO2 Binary Systems up to Supercritical Region. *J. Phys. Chem. A*, 111(8):1410–1418.

Nelson, G. L., Asmussen, S. E., Lines, A. M., Casella, A. J., Bottenus, D. R., Clark, S. B., and Bryan, S. A. (2018). Micro-Raman Technology to Interrogate Two-Phase Extraction on a Microfluidic Device. *Anal. Chem.*, 90(14):8345–8353.

Peters, C., Thien, J., Wolff, L., Koß, H.-J., and Bardow, A. (2020). Quaternary Diffusion Coefficients in Liquids from Microfluidics and Raman Microspectroscopy: Cyclohexane + Toluene + Acetone + Methanol. *J. Chem. Eng. Data*, 65(3):1273–1288.

Peters, C., Wolff, L., Haase, S., Thien, J., Brands, T., Koß, H.-J., and Bardow, A. (2017). Multicomponent diffusion coefficients from microfluidics using Raman microspectroscopy. *Lab Chip*, 17:2768–2776.

Poulsen, C. E., Wootton, R. C. R., Wolff, A., deMello, A. J., and Elvira, K. S. (2015). A Microfluidic Platform for the Rapid Determination of Distribution Coefficients by Gravity-Assisted Droplet-Based Liquid–Liquid Extraction. *Anal. Chem.*, 87(12):6265–6270.

Prabhu, G. R. D. and Urban, P. L. (2017). The dawn of unmanned analytical laboratories. *TrAC Trends Anal. Chem.*, 88:41 – 52.

Raal, J. D. and Mühlbauer, A. L. (1997). *Phase Equilibria: Measurement and Computation*. Taylor & Francis.

Schuster, J. J., Will, S., Leipertz, A., and Braeuer, A. (2014). Deconvolution of Raman spectra for the quantification of ternary high-pressure phase equilibria composed of carbon dioxide, water and organic solvent. *J. Raman Spectrosc.*, 45(3):246–252.

Stephan, K., Saab, J., Mokbel, I., Goutaudier, C., and Ferrigno, R. (2014). Continuous-flow microfluidic method for octanol-water partition coefficient measurement. *Fluid Phase Equilibr.*, 380:116–120.

Stratmann, A. and Schweiger, G. (2002). Fluid Phase Equilibria of Ethanol and Carbon Dioxide Mixtures with Concentration Measurements by Raman Spectroscopy. *Appl. Spectrosc.*, 56(6):783–788.

Susanti, S., Winkelman, J. G. M., Schuur, B., Heeres, H. J., and Yue, J. (2016). Lactic Acid Extraction and Mass Transfer Characteristics in Slug Flow Capillary Microreactors. *Ind. Eng. Chem. Res.*, 55:4691–4702.

Tang, S., Zhang, H., and Lee, H. K. (2016). Advances in Sample Extraction. *Anal. Chem.*, 88(1):228–249.

Teh, S.-Y., Lin, R., Hung, L.-H., and Lee, A. P. (2008). Droplet microfluidics. *Lab Chip*, 8:198–220.

Wang, K. and Luo, G. (2017). Microflow extraction: A review of recent development. *Chem. Eng. Sci.*, 169:18–33.

Weir, R. D. and de Loos, T. W. (2005). *Measurement of the Thermodynamic Properties of Multiple Phases*. Gulf Professional Publishing.

Wellsandt, T., Stanisch, B., and Strube, J. (2015). Development of Micro Separation Technology Modules. Part 1: Liquid-Liquid Extraction. *Chem. Ing. Tech.*, 87(9):1198–1206.

Whitesides, G. M. (2006). The origins and the future of microfluidics. *Nature*, 442:368–373.

Woehl, J., Meltzow, F., and Koß, H.-J. (2021). Method for Automatic Generation of Indirect Hard Models using crossvalidation (MAGIC) for the spectral analysis of mixture spectra. *Chemometr. Intell. Lab.*, 217:104419.

Xu, C. and Xie, T. (2017). Review of Microfluidic Liquid–Liquid Extractors. *Ind. Eng. Chem. Res.*, 56(27):7593–7622.

Yao, C., Zhao, Y., Ma, H., Liu, Y., Zhao, Q., and Chen, G. (2021). Two-phase flow and mass transfer in microchannels: A review from local mechanism to global models. *Chem. Eng. Sci.*, 229:116017.

Zhao, C.-X. and Middelberg, A. P. J. (2011). Two-phase microfluidic flows. *Chem. Eng. Sci.*, 66(7):1394 – 1411.

Aachener Beiträge zur Technischen Thermodynamik

ABTT 1
Philip Voll
Automated Optimization-Based Synthesis of Distributed Energy Supply Systems
1. Auflage 2014
ISBN 978-3-86130-474-6

ABTT 2
Johannes Jung
Comparative Life Cycle Assessment of Industrial Multi-Product Processes
1. Auflage 2014
ISBN 978-3-86130-471-5

ABTT 3
Franz Lanzerath
Modellgestützte Entwicklung von Adsorptionswärmepumpen
1. Auflage 2014
ISBN 978-3-86130-472-2

ABTT 4
Thorsten Brands
Einfluss der Gemischzusammensetzung auf die Verbrennung im Diesel- und GCAI-Motor
1. Auflage 2014
ISBN 978-3-95886-006-3

ABTT 5
Dominique Dechambre
Efficient Measurement of Liquid-Liquid Equilibria using Automation and Optimal Experimental Design
1. Auflage 2016
ISBN 978-395886-077-3

ABTT 6
Niklas von der Aßen
From Life-Cycle Assesement towards life-Cycle Design of Carbon Dioxide Capture and Utilization
1. Auflage 2016
ISBN 978-3-95886-080-3

ABTT 7
Matthias Lampe
Integrated Process and Organic Rankine Cycle Working Fluid Design in the Continuous-Molecular Targeting Framework
1. Auflage 2016
ISBN 978-3-95886-086-5

ABTT 8
Thomas Hülser
Optische Untersuchung der Zündvorgänge und deren Auswirkung auf die Verbrennung in PKW-Motoren
1. Auflage 2016
ISBN 978-3-95886-090-2

Aachener Beiträge zur Technischen Thermodynamik

ABTT 16
Bastian Liebergesell
A Milliliter-Scale Setup for the Efficient Characterization of Multicomponent Vapor-Liquid Equilibria Using Raman Spectroscopy
1. Auflage 2018
ISBN 978-3-95886-247-0

ABTT 17
Stefan Wilhelm Graf
A Design Approach for Adsorption Energy Systems Integrating Dynamic Modeling with Small-Scale Experiments
1. Auflage 2018
ISBN 978-3-95886-258-6

ABTT 18
Sebastian Kaminski
Quantum-Mechanics-Based Prediction of SAFT Parameters for Non-Associating and Associating Molecules Containing Carbon, Hydrogen, Oxygen and Nitrogen
1. Auflage 2019
ISBN 978-3-95886-270-8

ABTT 19
Maike Renate Hennen
Decision Support for the Synthesis of Energy Systems by Analysis of the Near-Optimal Solution Space
1. Auflage 2019
ISBN 978-3-95886-277-7

ABTT 20
Peyman Yamin
COSMO-RS-Based Methods for Improved Modelling of Complex Chemical Systems
1. Auflage 2019
ISBN 978-3-95886-288-3

ABTT 21
Meltem Erdogan
Assessement of Adsorbents for Drying by Experiments and Dynamic Simulations
1. Auflage 2019
ISBN 978-3-95886-303-3

ABTT 22
Christian Schulz
SRS/LIF-Messungen zur Charakterisierung rußarmer dieselähnlicher Flammen von alternativen Kraftstoffen und n-Heptan
1. Auflage 2019
ISBN 978-3-91886-310-1

ABTT 23
Peter Beumers
Physically-Based Models for the Analysis of Raman Spectra
1. Auflage 2019
ISBN 978-3-95886-319-4

Aachener Beiträge zur Technischen Thermodynamik

ABTT 24
Arne Kätelhön
Technology Choice Model for Consequential Life Cycle Assessment
1. Auflage 2019
ISBN 978-3-95886-324-8

ABTT 25
Christine Peters
Measurement of Multicomponent Diffusion in Liquids Using Raman Microspectroscopy and Microfluidics
1. Auflage 2020
ISBN 978-3-95886-337-8

ABTT 26
Dinah Elena Hollermann
Reliable and Robust Optimal Design of Sustainable Energy Systems
1. Auflage 2020
ISBN 978-3-95886-346-0

ABTT 27
Thomas Raffius
Laserspektroskopische Analyse von selbstzündenden motorischen Einspritzstrahlen alternativer Biokraftstoffe
1. Auflage 2020
ISBN 978-3-95886-358-3

ABTT 28
Johannes Schilling
Integrated Thermo-Economic Design of Processes and Molecules Using PC-SAFT
1. Auflage 2020
ISBN 978-3-95886-368-2

ABTT 29
Nils Julius Baumgärtner
Optimization of Low-Carbon Energy Systems from Industrial to National Scale
1. Auflage 2020
ISBN 978-3-95886-385-9

ABTT 30
Ludger Wolff
From Model-based Experimental Design and Analysis of Diffusion and Liquid-Liquid Equilibria to Process Applications
1. Auflage 2020
ISBN 978-3-95886-402-3

ABTT 31
Andrej Gibelhaus
A Model-based Framework for Optimal Systems Integration of Adsorption Chillers
1. Auflage 2021
ISBN 978-3-95886-406-1

ABTT 32
Jan Seiler
Debottlenecking the Evaporator in Water-Based Adsorption Chillers
1. Auflage 2021
ISBN 978-3-95886-407-8

Aachener Beiträge zur Technischen Thermodynamik

ABTT 33
Leif Kröger
Prediction of Reaction Rate Constants for the Synthesis of Microgels
1. Auflage 2021
ISBN 978-395886-425-2

ABTT 34
Sarah von Pfingsten
Uncertainty Analysis in Matrix-Based Life Cycle Assessment
1. Auflage 2022
ISBN 978-3-95886-431-3

ABTT 35
Ludger Leenders
Optimization Methods for Integrating Energy and Production Systems
1. Auflage 20022
ISBN 978-3-95886-445-0

ABTT 36
Leonard Müller
Harmonized Life Cycle Assessment of Technologies for Carbon Capture and Utilization
1. Auflage 2022
ISBN 978-3-95886-434-4

ABTT 37
Fritz Röben
Decarbonization of Copper Production by Optimal Demand Response
and Power-to-Hydrogen
1. Auflage 2022
ISBN 978-3-95886-458-0

ABTT 38
Johanna Kleinekorte
Predictive Life Cycle Assessment for Chemical Processes using Machine Learing
1. Auflage 2022
ISBN 978-3-95886-461-0

ABTT 39
Raoul Meys
Designing Pathways for Net-Zero Greenhouse Gas Emission Plastics
with Life Cycle Optimization
1. Auflage 2022
ISBN 978-3-95886-463-4

ABTT 40
Lukas Krep
Novel Acceleration Methods and Improved Transition State Finding Approaches for the
Automatic Exploration of Reaction Networks
1. Auflage 2023
ISBN 978-3-95886-480-1

ABTT 41
Andreas Kämper
Data-driven Modeling and Optimization of Multi-Energy Systems
1. Auflage 2023
ISBN 978-3-95886-488-7

Aachener Beiträge zur Technischen Thermodynamik

ABTT 42
Chriatiane Reinert
Optimization and Life-Cycle Assessment of Low-Carbon Energy systems from Industrial to International Scale
1. Auflage 2023
ISBN 978-3-95886-498-6

ABTT 43
Sarah Deutz
Life-Cycle Assessment of Low-Carbon Technologies from Screening to Integrated Energy system Design
1. Auflage 2023
ISBN 978-3-95886-499-6

ABTT 44
Hesam Ostovari
From Life Cycle Assessment to Optimal Supply Chains of CO2 Mineralization
1. Auflage 2023
ISBN 978-3-95886-509-9

ABTT 45
Justus Wöhl
Extension of Indirect Hard Modeling for the User-Independent and Automated Spectral Analysis of Reactive and Interacting Mixtures
1. Auflage 2023
ISBN 978-3-95886-511-2

ABTT 46
Carsten Flake
Automated Measurement Modeling and Interpretation of Diffusion Coefficients in Aqueous Multicomponent Mixtures
1. Auflage 2024
ISBN 978-95886-516-7

ABTT 47
Raphael Dewor
Laseroptische Untersuchungen von Verbrennungsprozessen bio-hybrider Kraftstoffe
1. Auflage 2024
ISBN 978-3-95886-522-8

ABTT 48
Christian Zibunas
Life Cycle Optimization towards Environmentally and Economically Sustainable Chemicals and Plastics
1. Auflage 2024
ISBN 978-3-95886-525-9

ABTT 49
Christoph Gertig
Computer-Aided Design of Molecules and Reactive Chemical Processes based on Quantum Chemistry
1. Auflage 2024
ISBN 978-95886-528-0

Aachener Beiträge zur Technischen Thermodynamik

ABTT 50
Marvin Bachmann
From Life Cycle Assessment to Absolute Environment Sustainability of Plastics from Alternative Carbon Feedstocks
1. Auflage 2024
ISBN 978-3-95886-530-3

ABTT 51
Mirko Engelpracht
Experimental Demonstration and Model-Based Optimization of Adsorption Heat Transformation for Waste Heat Upgrading
1. Auflage 2024
ISBN 978-3-95886-533-4

ABTT 52
David Müller
In-Line Monitoring and Control of Bioprocesses Using Raman Spectroscopy and Indirect Hard Modeling
1. Auflage 2024
ISBN 978-3-95886-537-2

ABTT 53
Matthias Henninger
Optimal Design of Small-Scale Experiments for Model-Based Scale-Up of Adsorption Chillers
1. Auflage 2024
ISBN 978-95886-539-6

ABTT 54
Julia Thien
A Microfluidic Platform for the Efficient Determination of Liquid-Liquid Equilibria Using Raman Microspectroscopy
1. Auflage 2025
ISBN 978-3-95886-542-6